UAB
Universitat Autònoma de Barcelona

Stabilizing Ferroelectricity in Ultrathin $BaTiO_3$ Films with Molecular Electrodes

Nona Mirzamohammadi

ADVERTIMENT. L'accés als continguts d'aquesta tesi queda condicionat a l'acceptació de les condicions d'ús establertes per la següent llicència Creative Commons:  https://creativecommons.org/licenses/?lang=ca

ADVERTENCIA. El acceso a los contenidos de esta tesis queda condicionado a la aceptación de las condiciones de uso establecidas por la siguiente licencia Creative Commons:  https://creativecommons.org/licenses/?lang=es

WARNING. The access to the contents of this doctoral thesis it is limited to the acceptance of the use conditions set by the following Creative Commons license:  https://creativecommons.org/licenses/?lang=en

Doctoral Thesis

Stabilizing Ferroelectricity in Ultrathin $BaTiO_3$ Films with Molecular Electrodes

submitted by

Nona Mirzamohammadi

for the degree of

Doctor of Philosophy in Materials Science

at the Autonomous University of Barcelona

Advisors:

Prof. Dr. Gustau Catalán Bernabé

Dr. David Pesquera

Dr. Kumara Cordero-Edwards

Tutor:

Prof. Dr. Javier Rodríguez- Viejo

2026





The research work done during the course of this thesis, has been carried out at Institut Català de Nanociència i Nanotecnologia (ICN2) during the period: Nov 2021 and Feb 2026, funded by Spanish Ministry of Science and Innovation under the grant PID2019-109931GB-I00 (SURFER) (doi: *10.13039/501100011033*), *and* PID2023-148673NB-I00 (GRIPHO2) (doi: *10.13039/50110001103*). All research at ICN2 is supported by a Severo Ochoa Grant CEX2021-001214-S.

Bellaterra, 20 de Febrero de 2026

El Prof. Gustau Catalán, científico titular y líder del grupo **Oxide Nanophysics**; el Dr. David Pesquera y la Dra. Kumara Cordero-Edwards, del **Institut Català de Nanociència i Nanotecnologia (ICN2)**; y el Dr. Javier Rodríguez Viejo, Catedrático del Departamento de Física de la **Universitat Autònoma de Barcelona (UAB)**, en calidad de tutor de tesis,

CERTIFICAN

Que Nona Mirzamohammadi ha realizado bajo su dirección y tutoría el trabajo titulado "**Stabilizing ferroelectricity in ultrathin $BaTiO_3$ films with Molecular Electrodes**". Dicho trabajo ha sido desarrollado dentro del programa de doctorado en Ciencia de Materiales y constituye su memoria de tesis doctoral para optar al grado de Doctora por la Universitat Autònoma de Barcelona.

Prof. Gustau CATALÁN
Group leader, Oxide Nanophysics group
ICN2 - ICREA

Dr. David PESQUERA
Senior postdoctoral researcher
ICN2

Dr. Kumara CORDERO-EDWARDS
Senior Postdoctoral Researcher
ICN2

Prof. Javier RODRIGUEZ VIEJO
Full Professor
UAB

Tribunal

Presidente:	***Assoc. Prof. Charlotte Cochard*** *charlotte.cochard@univ-rennes.fr*	***Institut des Sciences Chimiques de Rennes,*** *Rennes, France.*
Vocal:	***Assoc. Prof. Eric. Langenberg*** *eric.langenberg@ub.edu*	***Universitat de Barcelona (UB),*** *Barcelona, Spain.*
Secretario:	***Dr. Mariona Coll*** *mcoll@icmab.es*	***Institut de Ciència de Materials de Barcelona (ICMAB-CSIC),*** *Barcelona, Spain.*
Suplente:	***Prof. Luis E. Hueso*** *l.hueso@nanogune.eu*	***CIC nanoGUNE****,* *San Sebastián, Spain.*
Suplente:	***Prof. Eva Pellicer*** *Eva.Pellicer@uab.cat*	***Universitat Autònoma de Barcelona (UAB),*** *Barcelona, Spain.*
Suplente:	***Asst. Prof. Blai Casals Montserrat*** *bcasals@ub.edu*	***Universitat de Barcelona (UB),*** *Barcelona, Spain.*

Acknowledgments

I have waited for this part for a long time, and fun fact? Now I don't even know where to begin. But we shall get the job done. (Emotions? Please leave me alone for a while.)

Kumara Cordero Edwards! You have been much more than a supervisor to me. You have been my friend, my therapist, my non-existent sister, my shoulder to cry on, and MY AFM SUPERPOWER. Now that I look back, I am still in shock at how it is even possible that when you simply stepped foot in the AFM lab, the machine could sense your presence and suddenly everything would start working properly (the machine would be like: *HOSTIA, aquí viene la jefa!*). You taught me everything, but the most important thing of all? *Be patient with AFM.* Your voice is in my head now: *Details matter much more than you can imagine.* You have always treated AFM like a treasure, and it still amazes me how you can be this meticulous and passionate at the same time. That is something I truly wish for myself. And a word for Eric, who always brings a smile to my face: you are lucky as hell to have her as your mom :).

David, I will never forget my first day as a PhD student, meeting you in your office for the first time. You guided me — or let's say all of us — step by step. You bore all of my stupid questions. I was like a blind person in the lab, and you took my hand and walked me through everything. You are an extraordinary person. Your standards are so high that they have, from time to time, definitely crossed into frightening territory :). But if I were to wrap it up: I am pretty sure that if, when I am dying, someone randomly asks me to name three of the best scientists I've ever met, your name would be on that list :).

Gustau, I always remember a quote from Saptam: *I was an orphan and Gustau took me in.* At the time, I couldn't fully relate to the depth of its meaning, but now, looking back after more

than four years, I can say that no better words could describe it. I was hired by Neus, but when she had to leave, you treated me as one of your own. Thank you for accepting me into your group, for saving my PhD, for drawing a roadmap when I lost hope. Thank you for all the scientific discussions that didn't start with results, but rather with: *How are you doing?* Thank you for giving me the confidence to present at a conference for the first time. I will miss all the jokes you made about, well we all know about what, and sneaking looks at my face to see if I was bothered. Truth is, I never was, not even the slightest :). And lastly, thank you for being a **LEGEND** boss.

Gabriele, although you were not my official supervisor, you pretty much did the job while you were at ICN2, and even after you left. You were my "growth" dictionary. There wasn't a single problem or dilemma I faced that didn't find a solution with you. It was you who gave life to sputtering; without you, there would be no ultrathin films of mine. Thank you for always being so supportive. I might never have said this to you directly, but you are a brilliant scientist, and I feel honored to have learned from you, even if it was for a short time.

Roque, I'll keep it short. ICN2 would not function without you. You are the gem, capable of everything!! The number of times I've said and heard *"let's go to Roque"* over these four years is countless. Thank you for teaching me not only the serious stuff, but also the tiniest "stupid" things I didn't know. Like: *Roque, how do I even turn on the Keithley machine?!* But most importantly, thank you for the smile on your face that never fades, and for your unbelievable patience.

Santi, it was an honor learning from you. I will never forget the time you patiently explained all the necessary basics of reciprocal space on the whiteboard in our office. That old-school teaching lesson was truly precious to me.

Jessica, you are another gem, just like Roque. You have done hundreds of meticulous XRD measurements for each one of us, forming the fundamental basis of all our PhDs. Beautiful inside and out — thank you for always being there.

Umair, **Saptam**, **Wen Xin**, beyond everything else this PhD brought me, your friendships are among the most valuable souvenirs. Even if we don't see each other for a long time, our memories will always bring a smile to my face. I will never forget that my first birthday abroad, away from my family and friends, was spent at a synchrotron with you guys. And no champagne has ever tasted sweeter than the one we opened that night :). **Umair**, you were my PhD brother. We almost started together and almost finished together. I have to say: you are brilliant. You helped me far more than I could ever help you, and I will never forget that.

Arnau, **Tapas**, **Xinxin**, **Yingzhou**, **Gustavo**, **Shubham**, I truly enjoyed all the time we spent together, in our offices, group meetings, and lunch breaks :). I wish all of you a Nobel Prize someday in your future (well… maybe not all at the same time).

Felip, although I didn't have the chance to work with you directly during my PhD, I deeply admire your knowledge, and I truly enjoyed your company in both scientific and non-scientific discussions.

Neus, thank you for hiring me. Without you, I wouldn't be writing these acknowledgments right now. Who knows? maybe someday in the future I'll get the opportunity to work with you :). And **Irena**, thank you for the brilliant idea of "molecular electrodes" that shaped my thesis, and for all the time and energy you put into transferring your knowledge to me.

Christina, you were the first friend I found in Barcelona. You made my transition into this new life so much easier. You introduced me to your friends, showed me local bars (dear readers,

do not underestimate the importance of this when you're new to a city), and through you I met **Maria,** one of the most beautiful souls I've ever known :).

And yes — I had a life before starting a PhD. High-school friendships lasting more than 15 years and still going strong. **Bita**, **Sama**, **Saba**, **Zeynab**, **Negar**, **Helia**, **Maral**, **Mahsa**, **Mahgol** — you are the apples of my eyes. I've been away for more than four years, and not a single moment did I feel left out. Our daily FaceTimes are what kept me going during loneliness and pressure. We always said that when we're in our 60s, we'll all get a place and live together happily ever after. Unfortunately… I can now actually see that happening! **Mahyar, Bahram** and **Ehsan** I have always felt so close to you guys, and I appreciate your presence in my life.

Mom, **Dad**, **Reza**, **Maryam**, **and Vihan**, I owe everything to you. You have drawn such a sacred picture of family for me, one I have rarely seen anywhere else. You've shown me a level of unconditional love and support so strong that it sometimes frightens me and makes me wonder what I would do without you. I know that you probably won't be here on the day of my defense, but the fact that you all managed to come and visit me so close to this moment means the world to me. Writing these acknowledgments while sitting in front of all of you right now is something I will carry with me forever. **Vihan**, someday when you're older, I hope curiosity draws you toward science and that you come looking for my PhD thesis. If you read this, know that when you were born, a new light shone in our family. Wherever you are, and whatever you choose to do, your happiness will always be my priority.

Abstract

The downscaling of ferroelectric materials toward the nanometer and atomic limits is fundamentally constrained by depolarizing fields, which destabilize polarization, suppress switchability, and limit retention in ultrathin films. This thesis explores an alternative screening strategy based on organic molecular layers, focusing on para-aminobenzoic acid (pABA) as a ***molecular electrode*** capable of dynamically compensating polarization charge through its chemically resonant electronic structure. The central idea is that such molecules can mitigate depolarizing fields more effectively than conventional surface adsorbates, while preserving fast switching dynamics and enabling stable ferroelectric functionality at thicknesses inaccessible to traditional electrode configurations.

The thesis begins by establishing the physical framework governing ferroelectricity in the finite-size limit, emphasizing the increasing dominance of depolarizing fields and interface effects as film thickness is reduced. It motivates the use of molecular screening as a distinct route to stabilize polarization and domain retention and situates this approach within the broader context of ferroelectric tunnel junctions, where both ultrathin barriers and robust switchability are essential.

To provide a reliable structural foundation for the subsequent functional studies, the growth of epitaxial $BaTiO_3$ (BTO)/$SrRuO_3$ (SRO) heterostructures is optimized using Radio Frequency (RF)-sputtering. By correlating deposition parameters with surface morphology and growth modes, conditions are identified that enable smooth, uniform, and reproducible ultrathin films.

The switching dynamics of ferroelectric thin films are next investigated by comparing polarization reversal in bare and pABA-functionalized BTO using Piezoresponse Force

Microscopy (PFM). The results demonstrate that pABA significantly enhances switching performance, enabling stable domain writing at substantially higher scan speeds. This behavior indicates that molecular screening by pABA adapts rapidly to polarization reversal, outperforming atmospheric adsorbates whose slow redistribution limits switching dynamics.

Building on these findings, the role of molecular screening is extended to the ultrathin regime, where conventional surface and electrode screening fail to stabilize switchable polarization. For BTO films approaching and falling below the critical thickness, pABA functionalization is shown to restore stable polarization reversal and retention, even when bare films exhibit rapid back-switching or complete loss of ferroelectric response. These results demonstrate that molecular electrodes not only accelerate switching but also reduce the minimum thickness required for robust ferroelectric functionality.

Finally, the stabilization of polarization by molecular screening is further corroborated through polarization-dependent tunneling measurements in few-unit cell BTO films. In 2-unit cell-thick films, pABA functionalization enables bistable polarization states that give rise to clear and reproducible tunneling electroresistance, confirmed through both local Conductive Atomic Force Microscopy (CAFM) and macroscopic current–voltage measurements. The observed resistance contrast arises from polarization-controlled modulation of the tunneling barrier, demonstrating that molecular screening provides a viable pathway toward functional ferroelectric tunnel junctions at the atomic scale.

Overall, this thesis establishes pABA molecular layers as effective, fast, and adaptable screening agents that simultaneously enhance switching dynamics and stabilize polarization in the ultrathin limit. By bridging fundamental ferroelectric physics and molecular interface engineering,

this work demonstrates how molecular electrodes can overcome depolarization-driven limitations in ultrathin ferroelectric films.

Resumen

La miniaturización de los materiales ferroeléctricos hasta los límites nanométrico y atómico está fundamentalmente limitada por los campos despolarizantes, que desestabilizan la polarización, suprimen la capacidad de invertir la polarización y restringen la retención en películas ultrafinas. Esta tesis explora una estrategia alternativa de apantallamiento basada en capas moleculares orgánicas, centrada en el ácido para-aminobenzoico (pABA) como electrodo molecular capaz de compensar dinámicamente la carga de polarización mediante su estructura electrónica químicamente resonante. La idea central es que este tipo de moléculas puede mitigar los campos despolarizantes de forma más eficaz que los adsorbatos superficiales convencionales, manteniendo al mismo tiempo una dinámica de inversión de la polarización rápida y permitiendo una funcionalidad ferroeléctrica estable en espesores inaccesibles para configuraciones de electrodos tradicionales.

La tesis comienza estableciendo el marco físico que gobierna la ferroelectricidad en el límite de tamaño finito, destacando el dominio creciente de los campos despolarizantes y de los efectos de interfaz a medida que se reduce el espesor de la película. Se motiva el uso del apantallamiento molecular como una vía diferenciada para estabilizar la polarización y la retención de dominios, y se sitúa este enfoque dentro del contexto más amplio de las uniones túnel ferroeléctricas, donde son esenciales tanto las barreras ultrafinas como una inversión de la polarización robusta.

Con el fin de proporcionar una base estructural fiable para los estudios funcionales posteriores, se optimiza el crecimiento de heteroestructuras epitaxiales de $BaTiO_3$ (BTO)/$SrRuO_3$ (SRO) mediante pulverización catódica por radiofrecuencia (RF-sputtering). Al correlacionar los

parámetros de deposición con la morfología superficial y los modos de crecimiento, se identifican condiciones que permiten obtener películas ultrafinas lisas, uniformes y reproducibles.

A continuación, se investigan las dinámicas de inversión de polarización de películas ferroeléctricas comparando la inversión de polarización en BTO nativo y funcionalizado con pABA mediante microscopía de fuerza piezoeléctrica (PFM). Los resultados demuestran que el pABA mejora significativamente la capacidad para invertir rápidamente la polarización, permitiendo la escritura estable de dominios a velocidades de barrido sustancialmente más altas. Este comportamiento indica que el apantallamiento molecular proporcionado por el pABA se adapta rápidamente a la inversión de polarización, superando a los adsorbatos atmosféricos cuya redistribución lenta limita la dinámica de conmutación.

A partir de estos resultados, el papel del apantallamiento molecular se extiende al régimen ultrafino, donde los mecanismos convencionales de apantallamiento superficial y de electrodo no logran estabilizar una polarización conmutable. Para películas de BTO cercanas o por debajo del espesor crítico, se demuestra que la funcionalización con pABA restablece una inversión de polarización estable y una buena retención, incluso cuando las películas no-funcionalizadas presentan una pérdida completa de la capacidad para invertir la polarización o incluso dejan de presentar respuesta ferroeléctrica. Estos resultados muestran que los electrodos moleculares no solo aceleran la inversión de la polarización, sino que también reducen el espesor mínimo requerido para una funcionalidad ferroeléctrica robusta.

Finalmente, la estabilización de la polarización mediante apantallamiento molecular se corrobora mediante medidas de túnel dependientes de la polarización en películas de BTO de pocos parámetros de red. En películas de dos celdas unidad de espesor, la funcionalización con pABA permite la existencia de estados de polarización biestables que dan lugar a una electroresistencia

túnel clara y reproducible, confirmada tanto mediante microscopía de fuerza atómica conductiva (CAFM) local como mediante medidas macroscópicas corriente–voltaje. El contraste de resistencia observado se origina en la modulación de la barrera de túnel controlada por la polarización, demostrando que el apantallamiento molecular constituye una vía prometedora hacia uniones túnel ferroeléctricas funcionales a escala atómica.

En conjunto, esta tesis establece las capas moleculares de pABA como agentes de apantallamiento eficaces, rápidos y adaptables, que mejoran simultáneamente la dinámica de conmutación y estabilizan la polarización en el límite ultrafino. Al conectar la física fundamental de la ferroelectricidad con la ingeniería de intercaras moleculares, este trabajo demuestra cómo los electrodos moleculares pueden superar las limitaciones impuestas por los campos despolarizantes en películas ferroeléctricas ultrafinas.

Resum

La miniaturització dels materials ferroelèctrics fins als límits nanomètric i atòmic està fonamentalment limitada pels camps despolaritzants, que desestabilitzen la polarització, en redueixen la capacitat d'invertir la polarització i en limiten la retenció en pel·lícules ultrafines. Aquesta tesi explora una estratègia alternativa d'apantallament basada en capes moleculars orgàniques, centrada en l'àcid *para*-aminobenzoic (pABA) com a elèctrode molecular capaç de compensar dinàmicament la càrrega de polarització mitjançant la seva estructura electrònica químicament ressonant. La hipòtesi central és que aquestes molècules poden mitigar els camps despolaritzants de manera més eficient que els adsorbats superficials convencionals, tot preservant una dinàmica de inversió de polarització ràpida i permetent una funcionalitat ferroelèctrica estable a gruixos inaccessibles per a configuracions d'elèctrodes tradicionals.

La tesi s'inicia establint el marc físic de la ferroelectricitat en el límit de mida finita, destacant el paper creixent dels camps despolaritzants i dels efectes d'interfície a mesura que es redueix el gruix de la pel·lícula. Es justifica l'ús de l'apantallament molecular com una via diferenciada per estabilitzar la polarització i la retenció de dominis, i es contextualitza aquest enfocament dins l'àmbit de les unions túnel ferroelèctriques, on són essencials tant les barreres ultrafines com una commutació robusta.

Per proporcionar una base estructural sòlida als estudis funcionals posteriors, s'optimitza el creixement d'heteroestructures epitaxials de $BaTiO_3$ (BTO)/$SrRuO_3$ (SRO) mitjançant pulverització catòdica per radiofreqüència (RF-sputtering). Mitjançant la correlació dels paràmetres de deposició amb la morfologia superficial i els modes de creixement, s'identifiquen condicions que permeten obtenir pel·lícules ultrafines llises, uniformes i reproduïbles.

La dinàmica de commutació de les pel·lícules ferroelèctriques s'analitza comparant la inversió de polarització en BTO sense funcionalitzar i en BTO funcionalitzat amb pABA mitjançant microscòpia de força piezoelèctrica (PFM). Els resultats mostren que el pABA millora significativament el comportament de commutació, permetent l'escriptura estable de dominis a velocitats d'escaneig substancialment més elevades. Aquest fet indica que l'apantallament molecular del pABA s'adapta ràpidament a la inversió de polarització, superant les limitacions dels adsorbats atmosfèrics, la redistribució lenta dels quals frena la dinàmica de commutació.

Aquest efecte s'estén al règim ultrafí, on els mecanismes convencionals d'apantallament superficial i d'elèctrode no aconsegueixen estabilitzar una polarització commutable. En pel·lícules de BTO properes o per sota del gruix crític, la funcionalització amb pABA restableix una inversió de polarització estable i una bona retenció, fins i tot quan les pel·lícules sense funcionalitzar presenten retrocommutació ràpida o una pèrdua completa de la resposta ferroelèctrica. Aquests resultats demostren que els elèctrodes moleculars no només acceleren la commutació, sinó que també redueixen el gruix mínim necessari per a una funcionalitat ferroelèctrica robusta.

Finalment, l'estabilització de la polarització mitjançant apantallament molecular s'ha confirmat mitjançant mesures de túnel dependents de la polarització en pel·lícules de BTO de poques cel·les unitat. En pel·lícules de dues cel·les unitat de gruix, la funcionalització amb pABA permet l'existència d'estats de polarització bistables que donen lloc a una electroresistència túnel clara i reproduïble, confirmada tant per microscòpia de força atòmica conductiva (CAFM) com per mesures macroscòpiques corrent–tensió. El contrast de resistència observat s'origina en la modulació de la barrera de túnel controlada per la polarització, demostrant que l'apantallament molecular constitueix una via viable cap a unions túnel ferroelèctriques funcionals a escala atòmica.

En conjunt, aquesta tesi estableix que les capes moleculars de pABA són agents d'apantallament eficients, ràpids i adaptables, que milloren la dinàmica de commutació i estabilitzen la polarització en el límit ultrafí. En connectar la física fonamental de la ferroelectricitat amb l'enginyeria d'interfícies moleculars, aquest treball demostra com els elèctrodes moleculars poden superar les limitacions imposades pels camps despolaritzants en pel·lícules ferroelèctriques ultraprimes.

Table of Contents

1 Introduction 1

1.1 Ferroelectricity 2
1.2 Ferroelectric films: finite size effects and emergence of depolarization fields 4
1.3 Ferroelectric domains: atomic probe–based visualization and control 5
1.3.1 Domain formation stages and polarization switching dynamics probed by PFM .. 7
1.3.2 Influence of depolarization fields on domain retention 10
1.4 Screening mechanisms of depolarizing fields 12
1.4.1 Limitations of atmospheric adsorbates as screening agents 14
1.4.2 Organic molecules with resonance structures as efficient screening agents 15
1.5 Ferroelectric tunnel junctions 18
References 24

2 Growth optimization of $BaTiO_3/SrRuO_3$ heterostructures 29

2.1 Introduction 30
2.2 RF-sputtering: growth behavior beyond strain effects 32
2.2.1 Growth mode of SRO: transition from island formation to layer-by-layer 32
2.2.2 Initial nucleation and growth stages of BTO thin films 37
2.3 Concluding remarks 41
References 43

3 Polarization switching dynamics of para-aminobenzoic acid-functionalized $BaTiO_3$ thin films 47

3.1 Introduction 48
3.2 Functionalization of BTO with pABA molecular layers: transfer process and spectroscopic characterization 51
3.3 Initial domain configuration and polarization state before and after pABA functionalization 53
3.4 Writing speed analysis 55
3.4.1 Critical writing speed for homogenous domain formation 55
3.4.2 Dynamics of domain wall propagation 59
3.5 Concluding remarks 62
References 63

4 Polarization switching in ultrathin $BaTiO_3$ films stabilized by para-aminobenzoic acid functionalization 67

4.1 Introduction 68
4.2 Evolution of out-of-plane lattice parameter upon thickness decrease 70
4.3 Polarization states below the critical thickness 74
4.3.1 Static domain writing by PFM lithography 74
4.3.2 Local switching behavior by SS-PFM 78
4.4 Surface molecular screening and polarization switching stability in ultrathin BTO 80
4.4.1 Static domain writing by PFM Lithography 80
4.4.2 Local switching behavior by SS-PFM 82
4.4.3 Control experiments on pABA/SRO: verifying ferroelectric origin of PFM contrast 86
4.5 Concluding remarks 88
References 89

5 Tunneling electroresistance in ultrathin films 93

5.1 Introduction 94
5.2 Structural and ferroelectric characterization of 2-unit cell BTO films 96
5.3 Polarization-dependent tunneling and TER characterization by CAFM 99
5.3.1 Thickness dependence of the TER and mechanisms 104
5.4 Adding large-area top electrode for macroscopic measurements 108
5.4.1 Graphite flakes as soft top contact 108
5.5 Concluding remarks 111
References 112

6 Summary and outlook 115

6.1 Summary 116
6.2 Future works 117
References 120

7 Appendix 123

Appendix A: Fundamentals of piezoresponse force microscopy 124
References 127
Appendix B: Strain analysis of BTO/SRO films on different substrates 128
B.1 Introduction 128

B.2 Pulsed laser deposition: strain analysis 130
B.2.1 Growth of BTO/SRO heterostructures under substrate-induced strain 130
B.2.2 Effect of epitaxial strain and relaxation on surface stoichiometry 136
B.2.3 Ferroelectric benchmarking on fully strained BTO/SRO bilayers analyzed by SS-PFM 141
B.3 Concluding remarks 143
References 144

List of Figures

Figure 1.1 Landau free energy evolution across ferroelectric phase transitions 3
Figure 1.2 Nucleation-limited and sideways growth-limited switching mechanisms 8
Figure 1.3 Time-resolved PFM analysis of domain nucleation and growth 9
Figure 1.4 Depolarization-field–induced relaxation of piezoelectric response 11
Figure 1.5 PFM observation of depolarization-driven domain relaxation..... 12
Figure 1.6 Resonance structures and charge delocalization in pABA 16
Figure 1.7 Resistive switching in a ferroelectric tunnel junction 19
Figure 1.8 Polarization-controlled barrier modulation in ferroelectric tunnel junctions 21
Figure 2.1 Classical thin-film growth modes: Frank–van der Merwe (layer-by-layer growth), Stranski–Krastanov (layer-plus-island growth), and Volmer–Weber (three-dimensional island growth)..... 33
Figure 2.2 RF-power–dependent growth mode transition in SRO films 37
Figure 2.3 Deposition-time–dependent morphology evolution of BTO films..... 39
Figure 2.4 Stabilization of layer-by-layer growth in ultrathin BTO at reduced pressure. 41
Figure 3.1 pABA transfer process and spectroscopic confirmation of molecular chemisorption on BTO..... 52
Figure 3.2 XRD structural characterization of BTO thin film and PFM comparison before and after pABA functionalization..... 54
Figure 3.3 Writing-speed dependence of domain formation and stabilization in bare and pABA-functionalized BTO..... 59
Figure 3.4 Quantitative analysis of switched area and domain width versus writing speed..... 60
Figure 3.5 Bipolar molecular screening and reversible polarization switching in pABA-functionalized BTO..... 62
Figure 4.1 Thickness-dependent structural evolution and strain state of BTO films 72
Figure 4.2 Thickness-dependent loss of polarization stability in bare BTO films 75
Figure 4.3 Atomic-scale polarization mapping in ultrathin BTO 78
Figure 4.4 Thickness dependence of local switching behavior (SS-PFM) in bare BTO films.... 79
Figure 4.5 Restoration of polarization switching in ultrathin BTO by pABA functionalization .81
Figure 4.6 Bipolar switching and retention in pABA-functionalized ultrathin BTO 82

Figure 4.7 Comparison of local hysteresis behavior through SS-PFM in bare and pABA-functionalized ultrathin BTO 84
Figure 4.8 Effect of metallic (SRO) versus molecular (pABA) screening on local switching behavior through SS-PFM 86
Figure 4.9 Control experiment: Absence of artificial PFM contrast in pABA-coated SRO 88
Figure 5.1 Structural and ferroelectric characterization of 2-unit cell BTO films 98
Figure 5.2 Temporal stability of written domains in pABA-functionalized 2-unit cell BTO 99
Figure 5.3 Polarization-controlled tunneling transport and WKB barrier analysis in pABA-functionalized 2-unit cell BTO 101
Figure 5.4 Thickness dependence of polarization stability in pABA-functionalized 1- and 4-unit cell BTO films 105
Figure 5.5 Polarization-dependent transport in 4-unit cell BTO films 106
Figure 5.6 Macroscopic tunneling transport measurements using graphite top electrodes 109
Figure A.1 Schematic configuration and operating principles of vertical and lateral PFM 125
Figure B.1 Reciprocal space mapping of strain states in BTO/SRO bilayers across different substrates 133
Figure B.2 Influence of increased SRO bottom electrode thickness on the strain state of BTO on various substrates 135
Figure B.3 Laser-fluence–driven strain relaxation in BTO/SRO/STO films 139
Figure B.4 Ferroelectric switching behavior of fully strained BTO/SRO bilayers 142

List of Tables

Table B.1 Lattice mismatch values between different substrates and SRO and BTO 131
Table B.2 Growth parameters and stoichiometry–strain relaxation correlation in BTO/SRO bilayers 138

1 Introduction

This Chapter begins by introducing the fundamental aspects of ferroelectricity, and the physical parameters governing ferroelectric behavior. The discussion then advances toward ferroelectrics in the finite-size limit, where reducing the physical dimensions of the system enhances the role of interfaces and makes depolarizing fields increasingly significant. The Chapter then provides an overview of the evolution of atomic force microscopy–based techniques—from their initial use in imaging ferroelectric domains to their development as tools for writing and manipulating domains, where the impact of depolarizing fields on the lifetime of written domains becomes a central consideration. Conventional screening mechanisms for compensating depolarizing fields are briefly revisited, followed by the introduction of an alternative approach employing organic molecules with resonance structures for efficient charge screening. Finally, the Chapter outlines how this concept provides the basis for the present thesis, which aims to investigate the role of such molecular screening in enhancing switching dynamics and polarization stability in ultrathin ferroelectric films—an essential prerequisite for realizing functional ferroelectric tunnel junctions, whose principles are discussed at the end of the Chapter.

1.1 Ferroelectricity

Ferroelectric materials are characterized by spontaneous electric polarization that can be reversed by an external electric field once the field exceeds the coercive value E_c. In thermal equilibrium, polarization (P) can exist in two equivalent orientations +P and -P, corresponding to energetically degenerate stable states. This bistability is reflected in the typical hysteretic behavior of the polarization–electric-field (P-E) or displacement current–electric field (D-E) curves, which reflects the reversible switching between thermodynamically stable polarization states. Such intrinsic hysteresis distinguishes true ferroelectrics from non-crystalline electrets, in which charge alignment is metastable and arises from trapped charges rather than from an equilibrium ferroelectric phase. At the atomic level, ferroelectricity arises from ions displaced within a double-well potential, where the two minima represent the opposite polarization states of a local dipole. In perovskite oxides such as $BaTiO_3$ (BTO), for instance, the Ti^{4+} ion shifts from the centrosymmetric position, generating an electric dipole moment. Below the Curie temperature T_c, a non-centrosymmetric lattice configuration is stabilized in which the dipoles align cooperatively to form ferroelectric domains. Above T_c, thermal fluctuations restore centrosymmetry, and the spontaneous polarization vanishes, resulting in a paraelectric phase. The macroscopic description of these phenomena was developed through the Landau theory of phase transitions (1937)[1] and its specific application to ferroelectrics by Devonshire (1949).[2] In this framework, the Helmholtz free energy F (P,T,E) is expanded as a power series in the order parameter —the polarization P, and A, B, and C are coefficients:

$$F(P,T,E) = -EP + c + AP^2 + BP^4 + CP^6 \tag{1.1}$$

Coefficient A takes the form of:

$$A(T) = A_0(T - T_C), \tag{1.2}$$

and that the other coefficients are independent of temperature. It should be noted that the Curie temperature is not necessarily equal to phase transition temperature T_0. This distinction arises in first-order ferroelectric transitions, where the polarization changes discontinuously and the system exhibits thermal hysteresis, whereas in second-order transitions, T_c and T_0 coincide and the change in polarization is continuous. The equilibrium polarization corresponds to the minimum of F with respect to P. If B > 0, the coefficient C can be neglected and the transition is continuous (second-order), while for B < 0 transition is first-order, involving a discontinuous jump in polarization. The evolution of the free energy potential with temperature, illustrated in Fig. 1.1, shows how the wells become progressively shallower as the system approaches the Curie temperature, eventually merging into a single minimum above T_c. This transition corresponds to the disappearance of spontaneous polarization and marks the transformation from the ferroelectric to the paraelectric phase.[3–5]

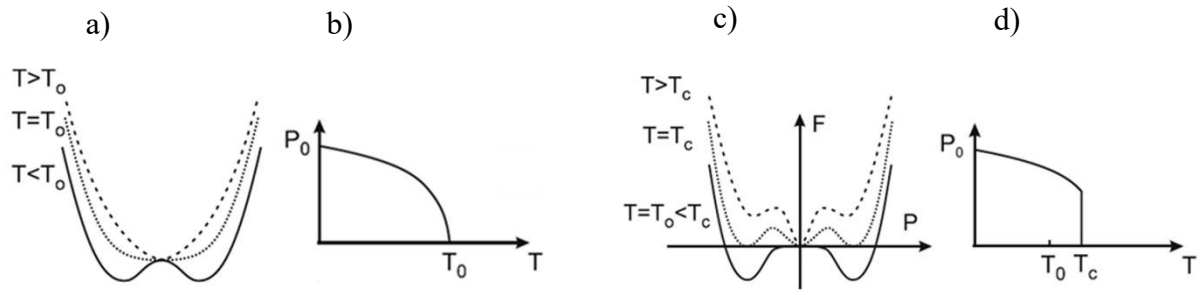


Figure 1.1 *Temperature dependence of the Landau–Devonshire free energy potential for ferroelectrics. (a) a second-order and (c) a first-order ferroelectric phase transition. Spontaneous polarization as a function of temperature showing a continuous change for second-order transition (b) and abrupt change at Tc for first-order transition (d). Adapted from Ref [5].*

1.2 Ferroelectric films: finite size effects and emergence of depolarization fields

The emergence of ferroelectricity originates from collective off-center ionic displacements, arising from the competition between long-range dipole–dipole Coulomb interactions and short-range covalent repulsions.[6] Ferroelectric materials are therefore highly sensitive to electromechanical boundary conditions because of the long-range nature of their electrostatic and mechanical (strain) interactions and, as the physical dimensions of a system are reduced, the ratio of surface or interface atoms to those in the bulk increases, making surface effects on bulk ferroelectric behavior unavoidable.[6,7] When the spontaneous polarization is oriented normal to the film surface, uncompensated surface charges can accumulate at the interfaces. If these charges are not screened, they give rise to an internal depolarizing field (E_d), which opposes spontaneous polarization. The presence of this field makes it energetically unfavorable for the system to maintain a uniform polarization state, often leading to the formation of ferroelectric domains as a means of minimizing electrostatic energy. The strength of the depolarizing field scales inversely with the film thickness; hence, thinner films experience stronger depolarizing effects that can suppress or even eliminate ferroelectricity altogether.[5] A theoretical study by Batra and Silverman (1972)[8] demonstrated that the polar state of a ferroelectric thin film between semiconducting electrodes with incomplete screening is unstable below a critical thickness of 400 nm, while this instability occurs at much smaller thicknesses when metal electrodes are used. Building on this, Tilley and Žekš[9] analyzed how the polarization P(z) varies spatially across the film thickness and how this non-uniformity affects the transition temperature T_0. Their analysis showed that T_0 decreases relative to the bulk value approximately in proportion

to 1/d, and that below a critical thickness, ferroelectricity ceases to be a stable thermodynamic phase.

The thermodynamic behavior of ferroelectric thin films is also strongly influenced by mechanical boundary conditions, owing to the tight coupling between polarization and elastic strain. In the 1990s, several studies demonstrated that mechanical clamping of the film by the substrate can profoundly modify the order parameters—namely, the polarization components—through the imposition of biaxial (2D) strain.[10,11] The substrate material and film thickness therefore serve as powerful parameters for tuning internal stress and, consequently, the ferroelectric and dielectric properties of the film. For instance, Choi et al.,[12] demonstrated that homogeneous misfit strain can be precisely controlled in epitaxial BTO films, enabling strain-engineering that enhances the spontaneous polarization beyond the bulk value. Furthermore, theoretical studies incorporated homogeneous epitaxial strain—arising from substrate–film lattice mismatch—into the Landau free energy formalism. Their analysis produced temperature–misfit strain phase diagrams, revealing the existence of "epitaxial phases" that are thermodynamically stable only under strain, and not in bulk ferroelectric crystals.[13,14]

1.3 Ferroelectric domains: atomic probe–based visualization and control

As discussed earlier, in a ferroelectric crystal, the spontaneous polarization does not necessarily remain uniform throughout the entire sample but often divides into regions of uniform polarization orientation, known as domains, separated by domain walls. Each domain represents a region where dipoles are aligned coherently in a specific direction corresponding to one of the free-energy minima. The formation of such domains minimizes the system's total energy by

balancing electrostatic, elastic, and gradient contributions. In thin films, the polarization configuration can range from a nearly monodomain state—where the entire film is uniformly polarized—to a polydomain state, comprising regions with different polarization orientations. The emergence of antiparallel domain configurations commonly serves to a screen depolarizing fields arising from finite-size effects and imperfect charge compensation at interfaces.[6] These screening mechanisms will be discussed in more detail in section 1.4.

Macroscopic susceptibilities in ferroelectrics, such as dielectric, piezoelectric, and switching responses, are strongly governed by domain-wall motion and domain reconfiguration. Therefore, capturing detailed information about domain structures is crucial for understanding and tailoring ferroelectric performance. A comprehensive overview of domain observation techniques can be found in the textbook work Domains in Ferroic Crystals and Thin Films by Tagantsev et al.,[15]. Among these, Atomic Force Microscopy (AFM)–based methods have represented a major breakthrough. Their application to ferroelectric systems enabled nondestructive nanoscale visualization -and manipulation- of domain structures and allowed researchers to determine whether a film exhibits an average monodomain state or a polydomain configuration. Beyond imaging, AFM techniques have made it possible to map surface potential distributions, measure local electromechanical and dielectric responses, and probe polarization stability with nanometer precision.

Moreover, the use of a conductive AFM tip to apply local electric fields introduced the ability to induce and control ferroelectric domains directly, rather than merely observing them. This capability is not only of fundamental interest but also of technological importance: the ability to reversibly switch polarization states underlies the operation of ferroelectric-based memory and logic devices, where information is stored in distinct polarization orientations that remain stable

after the external field is removed. Controlled domain writing and their reversible erasure thus provide a nanoscale analogue of bit manipulation in non-volatile memories, while also serving as a powerful model system for probing the intrinsic switching behavior of ferroelectrics. Using this approach, one can systematically explore whether switching is possible in a given system, identify the characteristic stages and kinetics of domain reversal, and evaluate the stability and retention of the newly written domains. These aspects of Piezoresponse Force Microscopy (PFM) are at the core of this thesis, and the operating principles behind them are described in Appendix A.

1.3.1 Domain formation stages and polarization switching dynamics probed by PFM

Polarization switching in ferroelectric materials is commonly described within the Kolmogorov–Avrami framework, as formulated by Ishibashi and Takagi[16] and later extended by Shur[17]. This model treats the evolution of the ferroelectric domain structure under an applied electric field as a phase transformation process involving the nucleation and subsequent growth of reversed polarization regions. For thin films, it is generally accepted that the forward domain growth—along the direction of the applied electric field—is much faster than the sideways (lateral) growth within the film plane. However, several studies have also reported cases where the opposite occurs, and the forward growth becomes the rate-determining step of the switching process.[18] These two switching scenarios are schematically illustrated in Fig. 1.2.

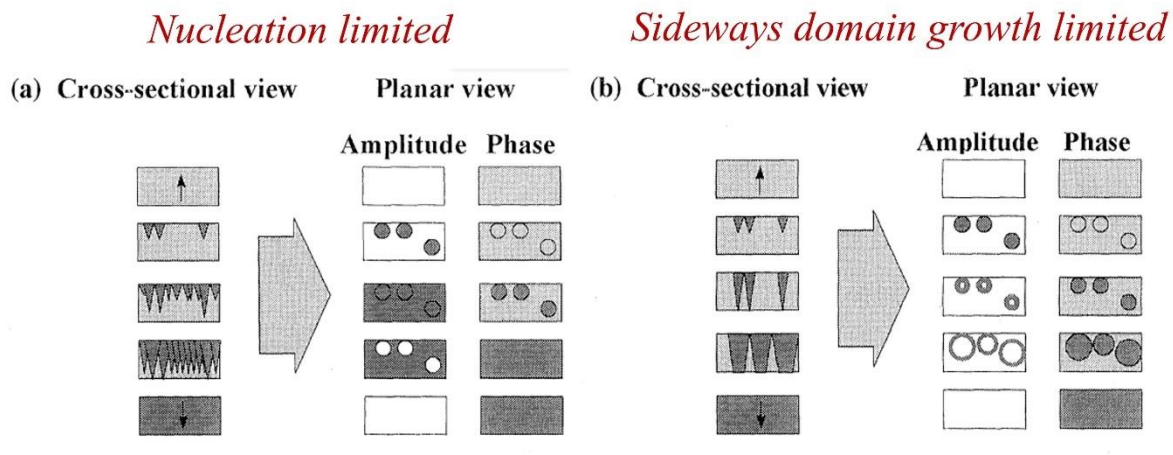


Figure 1.2 *Schematic illustration of polarization switching mechanisms in ferroelectric thin films through atomic force-based technique. (a) Nucleation and forward domain growth being the rate-limiting mechanism, where switching is governed by the appearance and forward propagation of domains along the electric field direction. (b) Sideways domain growth being the rate-limiting mechanism, where lateral expansion within the film plane dominates the overall switching process. Adapted from Ref [*[18]*].*

A major advance in understanding polarization reversal at the nanoscale was made by Gruverman et al.,[19] who performed direct studies of domain switching dynamics in ferroelectric thin films using PFM combined with pulsed electrical excitation. Their pump-probe experimental approach allowed sequential imaging of intermediate domain configurations during switching, enabling the evaluation of domain wall motion in both the forward (through-thickness) and lateral (in-plane) directions. By correlating the transient evolution of the PFM amplitude and phase signals with the applied voltage pulses, they were able to extract the characteristic times of domain nucleation, forward propagation, and lateral expansion. Analysis of the switched area as a function of time showed that the Kolmogorov–Avrami–Ishibashi (KAI) model accurately describes the nucleation-dominated regime of switching, while deviations at longer times reflect the transition to slower lateral growth. This study provided a direct experimental visualization of the multistage

nature of polarization reversal and established PFM as a powerful tool for correlating local switching kinetics with theoretical models. Representative results are shown in Fig. 1.3, illustrating (a) the evolution of domain configuration during switching, (b) the corresponding time dependence of the number of nuclei and switched area, and (c) schematic stages of domain nucleation, forward growth, and lateral expansion.

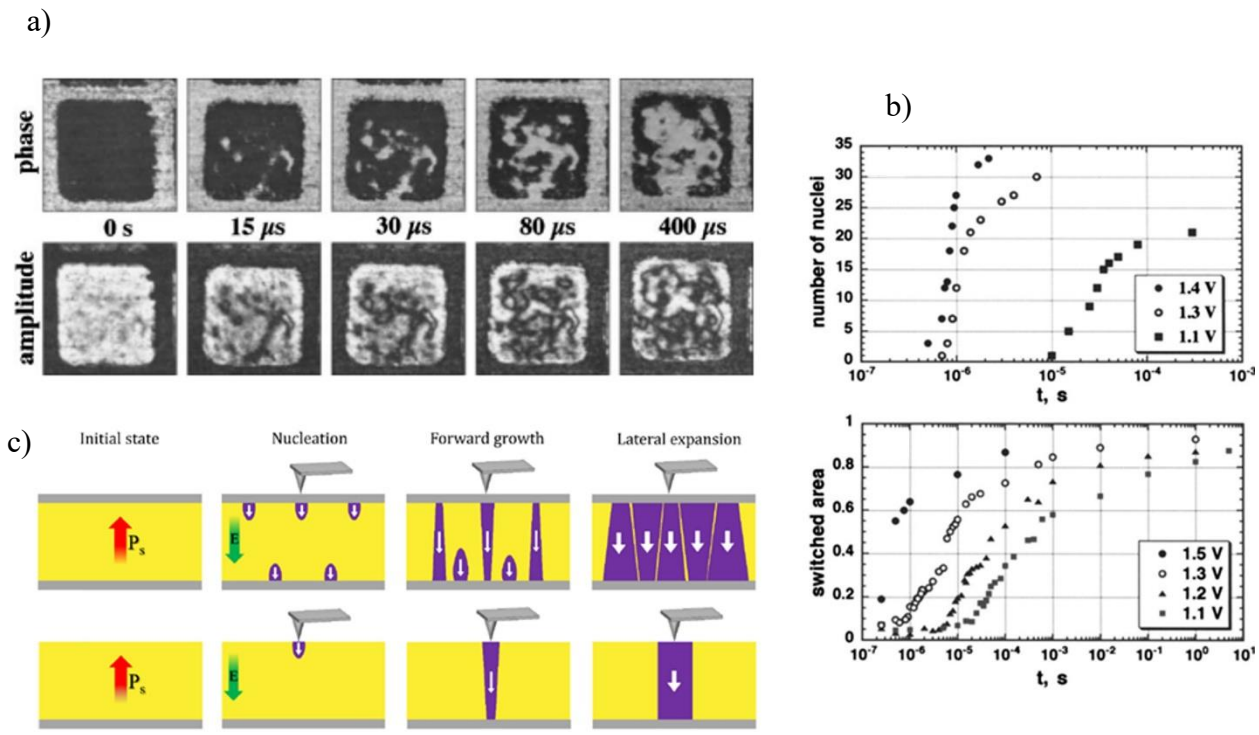


Figure 1.3 *(a, b) PFM phase and amplitude images of instantaneous domain configurations and the corresponding temporal evolution of nucleation and switched area during polarization reversal in a 3 × 3 μm² $Pb(Zr,Ti)O_3$ capacitor, adapted from Ref [[19]]. (c) Schematic illustration of the domain switching process, showing successive stages of nucleation, forward domain growth through the film thickness, and lateral expansion within the film plane, adapted from Ref [[7]].*

1.3.2 Influence of depolarization fields on domain retention

An equally important aspect of ferroelectric behavior, besides the domain formation stages and kinetics of domain wall motions, concerns the stability of the written domains. Long-term persistence of the switched state is governed by different physical mechanisms, among which depolarizing fields play a central role. These internal electric fields, arising from incomplete charge compensation at the film interfaces, can induce partial back-switching or relaxation of polarization over time, ultimately limiting the retention of the poled state. A seminal contribution to understanding such depolarization effects in ferroelectric thin films was made by Kholkin et al. (1997), who systematically investigated piezoelectric and dielectric aging in $Pb(Zr,Ti)O_3$ thin films and compared them with bulk ceramics.[20] Using precise interferometric measurements of the longitudinal piezoelectric coefficient (d_{33}), they monitored its temporal evolution during and after poling. The d_{33} response showed an initial rapid decay followed by a slower logarithmic relaxation (Fig. 1.4), attributed to back-switching of previously aligned domains driven by depolarizing fields. The study concluded that in thin films the strong depolarizing fields, inherent to their confined geometry, dominates piezoelectric relaxation.

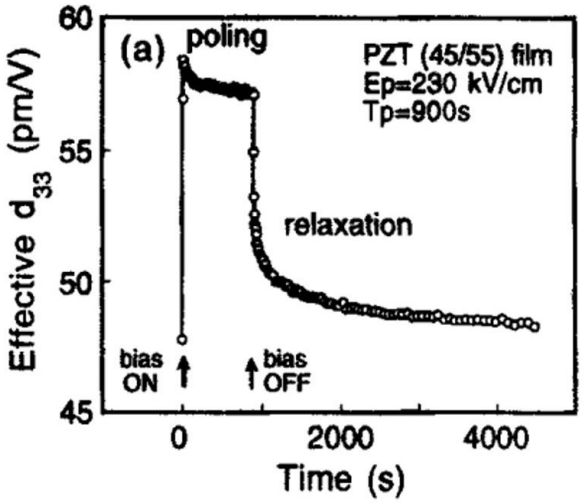


Figure 1.4 *Time dependence of the effective longitudinal piezoelectric coefficient d_{33} in a $Pb(Zr,Ti)O_3$ thin film during poling and subsequent relaxation. The observed decay reflects the back-switching of previously aligned domains induced by internal depolarizing fields. Adapted from Ref [*[20]*].*

While such macroscopic electrical measurements provided valuable averaged information on retention behavior, the subsequent introduction of atomic probe–based techniques, such as AFM and PFM, made it possible to probe these phenomena locally, at the nanoscale. Early PFM investigations revealed that, in addition to effects from defect pinning, trapped charges, and fatigue,[21–23] depolarizing fields play a central role in the loss of piezoresponse over time. These nanoscale studies demonstrated that retention degradation may appear either as a gradual shrinkage of poled domains[24,25] or as a reduction of the local amplitude and phase contrast in PFM images, arising from the formation of nanosized reverse domains below the spatial resolution of the probe.[26] Representative examples of such depolarization-field–driven relaxation phenomena are shown in Fig. 1.5, where domain shrinkage, polarization back-switching and stability of switched regions are visualized over time using PFM.

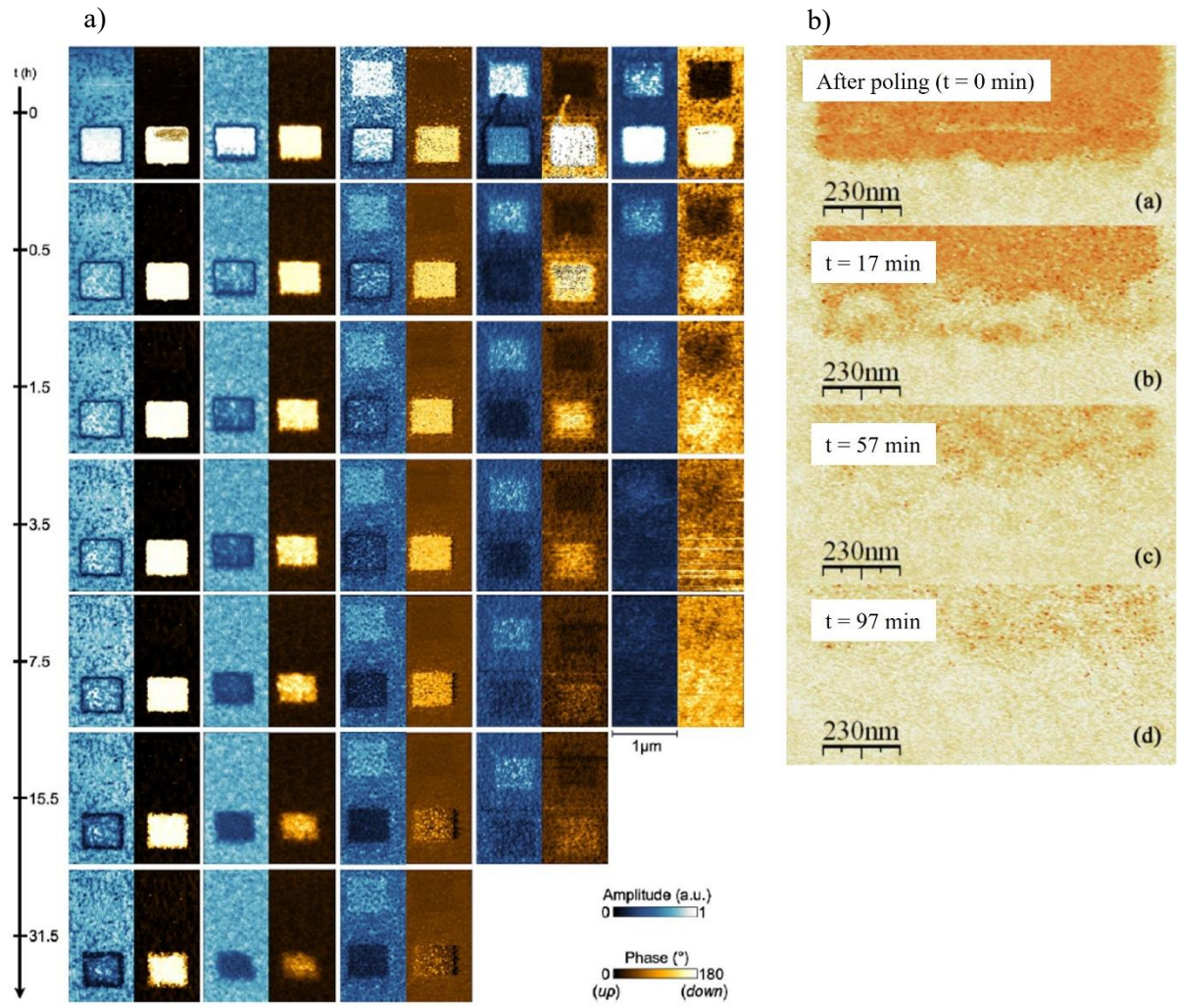


Figure 1.5 *PFM visualization of depolarization-field–driven relaxation and stability of written domains in ferroelectric thin films. (a,b) Adapted from Lichtensteiger et al.[26] and Morelli et al.[25] respectively.*

1.4 Screening mechanisms of depolarizing fields

In the previous sections, we discussed how depolarizing fields, arising from incomplete charge compensation at ferroelectric interfaces, play a crucial role in determining the stability of polarization and retention of switched states. Their influence has been demonstrated both macroscopically, through piezoresponse relaxation measurements, and at the nanoscale via PFM, where gradual relaxation and back-switching of domains were directly visualized. Understanding

how ferroelectric systems can counteract these destabilizing fields is therefore essential for achieving stable and switchable polarization, especially in thin films. In ferroelectric thin films, several screening mechanisms—both internal and external—can operate simultaneously to minimize the depolarization field. These mechanisms have been comprehensively discussed and categorized by Kalinin et al.,[27] Lichtensteiger et al.,[6] and Spasojević et al.[7] :

(i) **Internal screening:** arises from the redistribution of mobile charge carriers or charged point defects within the film towards the uncompensated surfaces. This redistribution generates surface dipoles and induces corresponding band bending. Among the most common internal screening agents are ionized oxygen vacancies.[28]

(ii) **Electrode screening:** Another important mechanism is screening by metallic electrodes, particularly in ferroelectric capacitor structures where the thin film is sandwiched between top and bottom electrodes. Ideally, metallic electrodes should fully compensate the bound surface charges; however, even atomically perfect interfaces do not provide complete screening. This imperfect screening originates from the finite Thomas–Fermi screening length of the metal,[29] which causes a spatial separation between the bound polarization charge and its compensating free charge in the electrode.

(iii) **Domain formation** represents another intrinsic mechanism for reducing depolarization fields. By splitting into 180° domains, a ferroelectric film can achieve an average surface charge close to zero, thereby minimizing the overall depolarizing energy. The number, size, and periodicity of these domains are determined by the competition between electrostatic energy, domain-wall formation energy, and elastic strain energy within the film.

(iv) **External screening** may occur through adsorption of environmental species, particularly water molecules, on the ferroelectric surface. In ambient conditions, water can physisorb or dissociate into hydroxyl (OH^-) and proton/hydronium (H^+/H_3O^+) species, which subsequently chemisorb on the surface. These adsorbates interact strongly with the surface polarization charge, partially compensating it and modifying the chemical boundary conditions at the interface.

1.4.1 Limitations of atmospheric adsorbates as screening agents

External screening by atmospheric adsorbates—particularly water-related species—can efficiently compensate the surface bound charges of ferroelectric thin films under ambient conditions and, in some cases can stabilize surface polarization more effectively than electrodes limited by finite screening length.[29] However, molecular screening mechanisms are constrained by both kinetics and charge capacity, which become critical during fast polarization switching and in ultrathin films.

The critical writing speed for successful polarization reversal and the stability of written ferroelectric domains are strongly influenced by environmental humidity, which directly governs the density and mobility of adsorbed water molecules on the surface. Experimental studies have shown that at low humidity levels, the critical writing speed decreases markedly, meaning that stable polarization switching becomes increasingly difficult to achieve.[30] This behavior originates from two concurrent factors: (i) the reduced surface coverage of polar water species, which diminishes the total available screening charge, and (ii) the finite reorientation time associated with molecular dipole adjustment upon polarization reversal. The resulting transient depolarizing field

can drive partial back-switching or incomplete domain stabilization, effectively limiting the achievable switching speed in ambient environments.

In the ultrathin regime, these limitations are exacerbated because the available charge from atmospheric adsorbates is insufficient to compensate the bound charge density, leading to large residual depolarizing fields, diminishing the polarization retention times, and ultimately constraining the thickness range over which stable switchable polarization can be achieved under ambient screening alone.

1.4.2 Organic molecules with resonance structures as efficient screening agents

While atmospheric adsorbates such as water-related species can partially compensate depolarizing fields in ferroelectric thin films, their ability to provide sufficient and stable charge compensation is inherently limited by slow molecular reorientation and incomplete dipole reversal. These deficiencies motivated the exploration of more robust screening strategies capable of delivering stable and bidirectional compensation of polarization charges. Among these, organic molecules possessing resonance-stabilized structures have emerged as promising candidates due to their intrinsic charge delocalization and tunable electronic properties.

Among various molecular candidates, para-aminobenzoic acid (pABA) is a particularly attractive system. The amino ($–NH_2$) group in pABA acts as an electron donor, capable of coupling its lone electron pair with the benzene ring and further with the lone electron pairs of the oxygen atoms in the carboxylic (–COOH) group. This intramolecular delocalization enables electrons to be distributed across the entire molecular backbone, resulting in a resonance structure that can flexibly redistribute charge across the molecule structure.[31,32] Schematics of electronic

configurations of some of the chemical resonance structures of pABA molecules are shown in Fig. 1.6.

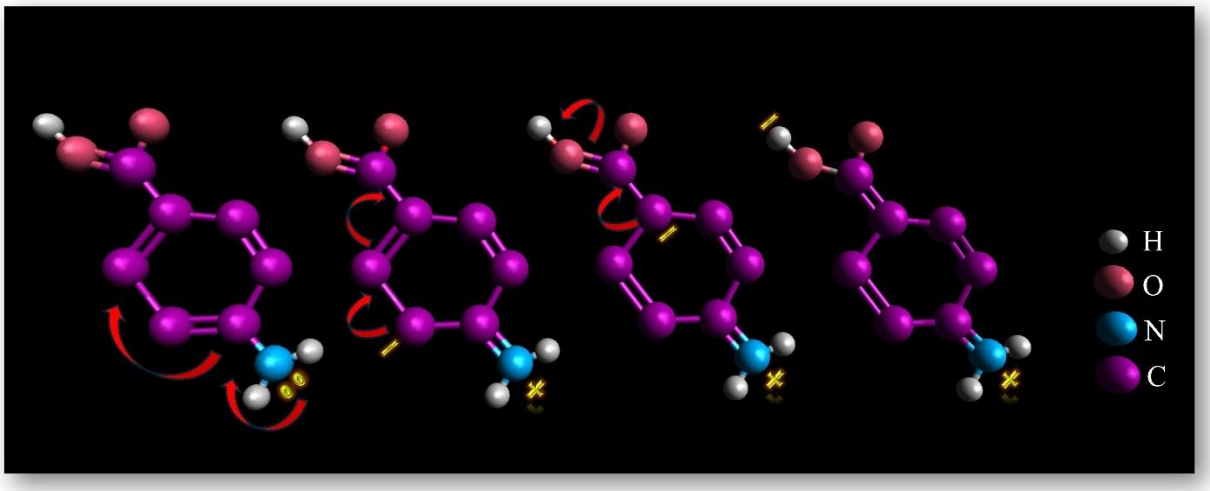


Figure 1.6 *Some resonance structures of pABA aromatic molecule. The* $-NH_2$ *group is an electron donor able to couple its lone electron pair with the high electron density of benzene ring and further with lone electron pairs of oxygen atoms in the carbonyl (C=O) group and the -OH group of the carboxylic (COOH) substituent, giving rise to the resonance hybrid structure. Adapted from Ref [*[31]*].*

Before its introduction into ferroelectric systems, pABA was employed in perovskite solar cells as an interfacial modifier between oxide transport layers and methyl-ammonium lead halide perovskites. Chemisorption of its carboxyl group onto metal-oxide surfaces such as TiO_2 or ZnO improves interfacial contact, passivates surface defects, and facilitates charge transfer across the junction. These effects collectively suppress interfacial recombination and enhance carrier extraction, leading to improved device performance and stability.[33,34] Building upon these interfacial properties, Spasojević et al.[32] first proposed coupling pABA molecules with ferroelectric thin films to harness their resonance-driven charge redistribution as an efficient mechanism for screening polarization charges. In their work on BTO films, the pABA molecular

layer was found to interact with the surface polarization, providing bidirectional screening for upward and downward polarization states. Fourier Transform Infrared Spectroscopy (FT-IR) revealed that pABA molecules chemically attach to the BTO surface through an ester-like monodentate linkage between one oxygen atom of the carboxylic group and a surface Ti^{4+} site—consistent with previous adsorption studies on TiO_2 surfaces.[34] This bonding configuration preserves the conjugated π-system of the aromatic ring, enabling dynamic redistribution of electron density between the amino group and carboxyl terminus upon polarization reversal, without requiring any molecular reorientation on the surface. As a result, the molecular layer can stably screen both polarization directions and effectively suppress depolarizing fields in ferroelectric films.

Based on the fact that this molecular screening mechanism relies on the fast internal redistribution of delocalized electrons—rather than the slower dipole reorientation typical of atmospheric adsorbates—this thesis explores two key aspects of pABA-functionalized (BTO) ferroelectric thin films.

(i) First, we investigate whether the presence of pABA molecules can promote faster polarization switching dynamics compared to bare BTO films (i.e., films exposed to ambient atmospheric conditions without molecular modification), focusing on relatively thick films where depolarizing fields are not expected to dominate the polarization stability.

(ii) Second, we examine whether the incorporation of pABA onto ultrathin BTO films, with thicknesses below the critical limit for stable ferroelectricity, can enhance polarization retention and mitigate depolarizing field effects, thereby enabling robust and long-lasting switchable polarization states at lower critical thickness than with atmospheric adsorbates. As I will show, it is indeed possible to achieve stable monodomain polarization in ultra-thin BTO thin films whose

surface is functionalized with pABA. In turn, the stability of monodomain polarization in the ultrathin regime allows exploring tunnelling electrorresistive functionality.

1.5 Ferroelectric tunnel junctions

Ever since observation of bistable switching phenomena in ferroelectric thin films, these materials have been proposed as candidates for non-volatile memories.[3] Ferroelectricity persisting down to sub-nanometer scale thicknesses opens a possibility to further miniaturize electronic devices, particularly as tunnel barriers in metal–ferroelectric–metal (M–FE–M) junctions.[35] Early studies by Contreras et al. demonstrated that electrical resistance in M-FE-M junctions with ultrathin barriers depends on the orientation of the ferroelectric polarization.[36] In their studies, current–voltage (I–V) characteristics of the M-FE-M junctions involving a 6-nanometer-thick $Pb(Zr_{0.52}Ti_{0.48})O_3$ barriers exhibited reproducible resistive switching events at well-defined electric fields. These changes in conductance were attributed to polarization reversal within the barrier and the resulting modulation of tunneling transport. An example of such polarization-induced resistive switching behavior is presented in Fig. 1.7.

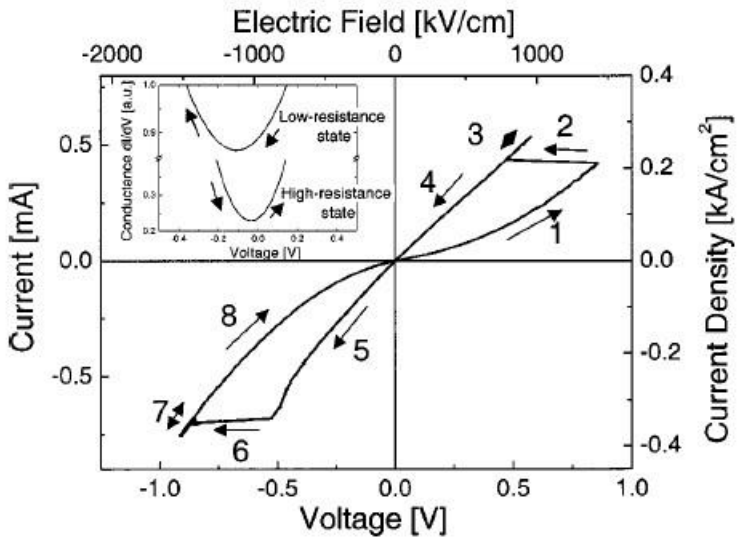


Figure 1.7 *I –V characteristic of M-FE-M tunnel junction with a 6-nm-thick $PbZr_{0.52}Ti_{0.48}O_3$ as FE barrier layer, showing a resistive switching behavior. Image is adapted from Ref [*[36]*].*

Building on these observations, Tsymbal and co-workers developed a theoretical model incorporating the finite screening of polarization charges in metallic electrodes and quantum-mechanical tunneling across the ferroelectric layer.[37] Their analysis proposes that the so-called tunneling electroresistance arises from the modulation of the electrostatic potential profile across the barrier upon polarization reversal. The polarization-dependent redistribution of screening charges at the interfaces modifies the average barrier height experienced by tunneling electrons, thereby generating distinct conductance states corresponding to the two polarization orientations. This polarization-dependent modulation of the tunneling conductance can be understood intuitively by examining how the ferroelectric polarization alters the electrostatic potential landscape across the junction. To illustrate this effect, we consider a ferroelectric layer sandwiched between two dissimilar metallic electrodes with unequal screening capabilities:

At the surface of a ferroelectric barrier, bound polarization charges accumulate depending on the orientation of the spontaneous polarization. These charges attract or repel free carriers in the adjacent electrode, producing an electrostatic potential step at the ferroelectric/electrode interface. Because charge compensation in real metals is not perfect, the screening of polarization charges occurs over a finite distance, determined by the Thomas–Fermi screening length, which depends on the carrier density at the Fermi level. As a result, a finite depolarizing field persists inside the ferroelectric layer, leading to a polarization-dependent modification of the electrostatic potential profile across the junction. When polarization points toward the better-screening electrode (with the shorter screening length), the imperfect compensation of polarization charge at that bottom interface produces a potential profile that tilts upward, increasing the average tunnel barrier height (Φ^{+}) and leading to a low-conductance (high-resistance/OFF) state (Fig. 1.8a-right). Conversely, when the polarization is reversed to point toward the less efficient electrode, the electrostatic potential reverses its asymmetry, decreasing the average barrier height (Φ^{-}) and yielding a high-conductance (low-resistance/ON) state (Fig. 1.8a-left). Because the tunneling current depends exponentially on the barrier height and width, even modest polarization-induced changes in the interfacial potential can produce orders-of-magnitude variations in conductance—a phenomenon known as the tunneling electroresistancre effect.[38] Although the archetypal model assumes electrodes with unequal screening capabilities, structural or chemical asymmetries at the ferroelectric interfaces can produce a similar modulation of the potential profile.[39,40]

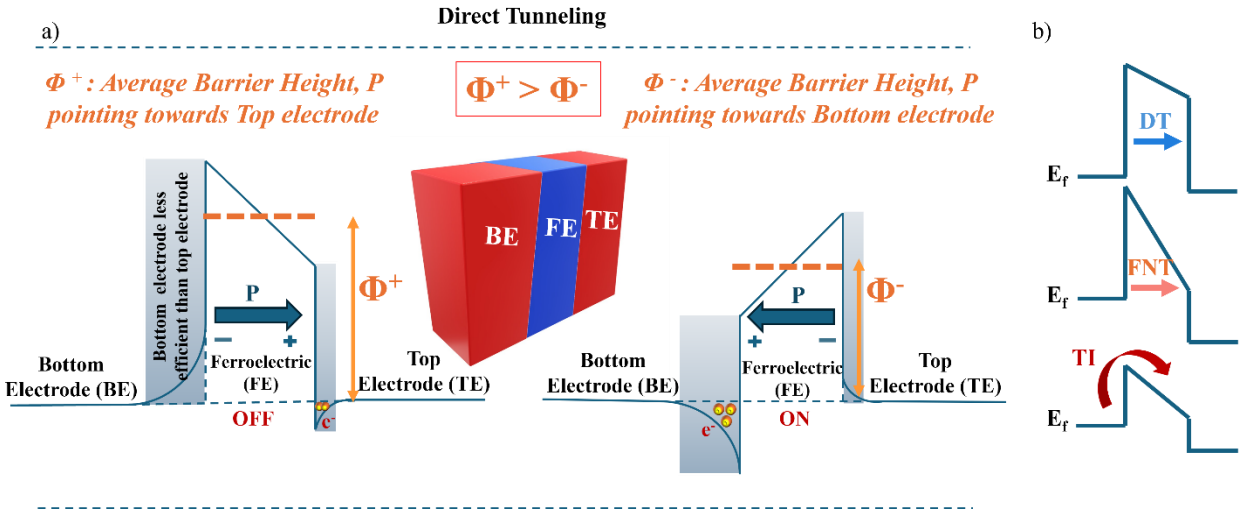


Figure 1.8 *a) Schematic illustration of the tunneling electroresistance effect in a ferroelectric tunnel junction. The ferroelectric (FE) barrier is sandwiched between two metallic electrodes (BE and TE) with different screening efficiencies. (Left) When polarization points toward the better-screening electrode (TE), imperfect charge compensation results in a higher average barrier height (Φ^+), yielding a low-conductance (high-resistance) state. (Right) Reversal of polarization toward the less efficient electrode (BE) inverts the potential asymmetry, producing a lower average barrier height (Φ^-) and a high-conductance (low-resistance) state. b) Transport mechanisms through an ultrathin ferroelectric barrier, involving direct tunneling (DT), Fowler–Nordheim tunneling (FNT), and thermionic injection (TI). (a,b) Adapted from Ref [39].*

Following the early demonstration of polarization-dependent tunneling currents, Pantel and Alexe[41] developed a more comprehensive framework describing charge transport across metal–ferroelectric–metal junctions. Recognizing that purely direct tunneling could not account for all observed current–voltage characteristics in ultrathin ferroelectric barriers, they incorporated three coexisting transport processes—direct tunneling, Fowler–Nordheim tunneling (FNT), and thermionic injection. In their analysis, the FNT process was described as an extension of direct tunneling into the high-field regime, where electrons traverse the triangular portion of the barrier once the applied bias significantly tilts the potential profile. Consequently, as in direct tunneling,

the average barrier height remains the key factor governing current modulation by polarization reversal. In contrast, thermionic injections refer to charge transport by carriers that overcome the potential barrier through thermal excitation rather than quantum tunneling. The effective barrier height in this case is reduced by image-force lowering, a phenomenon known as the Schottky effect. As a result, the thermionic current is highly sensitive to both the bias polarity and the polarization-dependent barrier height at the injecting interface. In this regime, one polarization orientation does not necessarily correspond to a uniformly higher conductance for both voltage polarities. Depending on which interface dominates carrier injection, the system can exhibit either positive or negative electroresistance ratios. Schematics of these three transport regimes—direct tunneling, Fowler–Nordheim tunneling, and thermionic injection—are illustrated in Fig. 1.8b.

Crucial to any of the discussed ferroelectric electroresistance schemes, is the need to have two distinct homogeneous polar states. As we have also shown in this thesis, such requirement is difficult to meet in the ultra-thin regime, where depolarization fields can lead to loss of ferroelectricity or a breakdown into polydomain states where the net polarization is zero. Since pABA layers are expected to have higher screening efficiencies and thus have the potential to stabilize monodomain ferroelectricity down to lower critical thicknesses, in the final part of this thesis, we extend the investigation of organic–ferroelectric hybrid systems into the regime of ferroelectric tunnel junctions. To experimentally probe tunneling electroresistance in these molecularly functionalized ultrathin films, we employed Conductive Atomic Force Microscopy (CAFM) for nanoscale current mapping and local I–V spectroscopy, complemented by preliminary attempts to measure macroscopic devices fabricated from similar heterostructures. Specifically, we examine whether the molecular functionalization strategy introduced earlier—using pABA organic molecules—can enable stable and switchable polarization states in BTO films with unit

cell-scale thickness, where electron tunneling is expected to become the dominant transport mechanism.

References

1 L. LANDAU, “The Theory of Phase Transitions,” Nature 138(3498), 840–841 (1936).

2 A.F. Devonshire, “XCVI. Theory of barium titanate,” The London, Edinburgh, and Dublin Philosophical Magazine and Journal of Science 40(309), 1040–1063 (1949).

3 J.F. Scott, *Ferroelectric Memories* (Springer Berlin Heidelberg, Berlin, Heidelberg, 2000).

4 M.E. Lines, and A.M. Glass, *Principles and Applications of Ferroelectrics and Related Materials* (Oxford University Press, 2001).

5 K.M. Rabe, C.H. Ahn, and J. Triscone, editors , *Physics of Ferroelectrics* (Springer Berlin Heidelberg, Berlin, Heidelberg, 2007).

6 C. Lichtensteiger, P. Zubko, M. Stengel, P. Aguado-Puente, J. Triscone, P. Ghosez, and J. Junquera, “Ferroelectricity in Ultrathin-Film Capacitors,” in *Oxide Ultrathin Films*, (Wiley, 2011), pp. 265–230.

7 I. Spasojević (Author), N. Domingo Marimon (Director), and G. Catalán Bernabé (Director), Interplay Between Ferroelectricity and Surface Chemistry in BaTiO3, 2022.

8 I.P. Batra, and B.D. Silverman, “Thermodynamic stability of thin ferroelectric films,” Solid State Commun. 11(1), 291–294 (1972).

9 D.R. Tilley, and B. Žekš, “Landau theory of phase transitions in thick films,” Solid State Commun. 49(8), 823–828 (1984).

10 N.A. Pertsev, A.G. Zembilgotov, and A.K. Tagantsev, “Effect of Mechanical Boundary Conditions on Phase Diagrams of Epitaxial Ferroelectric Thin Films,” Phys. Rev. Lett. 80(9), 1988–1991 (1998).

11 S.B. Desu, Z.J. Chen, V.P. Dudkevich, P. V. Dudkevich, I.N. Zakharchenko, and G.L. Kushlyan, “The Phase Diagram of Epitaxial BaTiO3 Films under Bi-Axial Stress,” MRS Proceedings 433, 345 (1996).

12 K.J. Choi, M. Biegalski, Y.L. Li, A. Sharan, J. Schubert, R. Uecker, P. Reiche, Y.B. Chen, X.Q. Pan, V. Gopalan, L.-Q. Chen, D.G. Schlom, and C.B. Eom, “Enhancement of Ferroelectricity in Strained BaTiO3 Thin Films,” Science (1979). 306(5698), 1005–1009 (2004).

13 N.A. Pertsev, A.G. Zembilgotov, and A.K. Tagantsev, “Equilibrium states and phase transitions in epitaxial ferroelectric thin films,” Ferroelectrics 223(1), 79–90 (1999).

14 Z.G. Ban, and S.P. Alpay, “Phase diagrams and dielectric response of epitaxial barium strontium titanate films: A theoretical analysis,” J. Appl. Phys. 91(11), 9288–9296 (2002).

15 A.K. Tagantsev, L.E. Cross, and J. Fousek, *Domains in Ferroic Crystals and Thin Films* (Springer New York, New York, NY, 2010).

16 Y. Ishibashi, and Y. Takagi, "Note on Ferroelectric Domain Switching," J. Physical Soc. Japan 31(2), 506–510 (1971).

17 V. Shur, E. Rumyantsev, and S. Makarov, "Kinetics of phase transformations in real finite systems: Application to switching in ferroelectrics," J. Appl. Phys. 84(1), 445–451 (1998).

18 S. Hong, "Polarization Switching and Fatigue of Ferroelectric Thin Films Studied By PFM," in *Nanoscale Phenomena in Ferroelectric Thin Films*, (Springer US, Boston, MA, 2004), pp. 111–131.

19 A. Gruverman, B.J. Rodriguez, C. Dehoff, J.D. Waldrep, A.I. Kingon, R.J. Nemanich, and J.S. Cross, "Direct studies of domain switching dynamics in thin film ferroelectric capacitors," Appl. Phys. Lett. 87(8), (2005).

20 A.L. Kholkin, A.K. Tagantsev, E.L. Colla, D. V. Taylor, and N. Setter, "Piezoelectric and dielectric aging in pb(zr,ti)o3 thin films and bulk ceramics," Integrated Ferroelectrics 15(1–4), 317–324 (1997).

21 O. Auciello, A. Gruverman, H. Tokumoto, S.A. Prakash, S. Aggarwal, and R. Ramesh, "Nanoscale Scanning Force Imaging of Polarization Phenomena in Ferroelectric Thin Films," MRS Bull. 23(1), 33–42 (1998).

22 V.V. Shvartsman, A.L. Kholkin, C. Verdier, Z. Yong, and D.C. Lupascu, "Investigation of fatigue mechanism in ferroelectric ceramic via piezoresponse force microscopy," J. Eur. Ceram. Soc. 25(12), 2559–2561 (2005).

23 V. Anbusathaiah, V. Nagarajan, and S. Aggarwal, "High-resolution piezoresponse force microscopy investigation of imprint in ferroelectric thin films," Appl. Phys. Lett. 89(13), (2006).

24 A.L. Kholkin, I.K. Bdikin, D.A. Kiselev, V. V. Shvartsman, and S.H. Kim, "Nanoscale characterization of polycrystalline ferroelectric materials for piezoelectric applications," J. Electroceram. 19(1), 81–94 (2007).

25 A. Morelli, S. Venkatesan, G. Palasantzas, B.J. Kooi, and J.T.M. De Hosson, "Polarization retention loss in PbTi O3 ferroelectric films due to leakage currents," J. Appl. Phys. 102(8), (2007).

26 C. Lichtensteiger, S. Fernandez-Pena, C. Weymann, P. Zubko, and J.M. Triscone, "Tuning of the depolarization field and nanodomain structure in ferroelectric thin films," Nano Lett. 14(8), 4205–4211 (2014).

27 S. V Kalinin, Y. Kim, D.D. Fong, and A.N. Morozovska, "Surface-screening mechanisms in ferroelectric thin films and their effect on polarization dynamics and domain structures," Reports on Progress in Physics 81(3), 036502 (2018).

28 Y.M. Kim, A. Morozovska, E. Eliseev, M.P. Oxley, R. Mishra, S.M. Selbach, T. Grande, S.T. Pantelides, S. V. Kalinin, and A.Y. Borisevich, "Direct observation of ferroelectric field effect and vacancy-controlled screening at the BiFeO3/LaxSr1 - xMnO3 interface," Nat. Mater. 13(11), 1019–1025 (2014).

29 P. Zubko, H. Lu, C.-W. Bark, X. Martí, J. Santiso, C.-B. Eom, G. Catalan, and A. Gruverman, "On the persistence of polar domains in ultrathin ferroelectric capacitors," Journal of Physics: Condensed Matter 29(28), 284001 (2017).

30 I. Spasojevic, A. Verdaguer, G. Catalan, and N. Domingo, "Effect of Humidity on the Writing Speed and Domain Wall Dynamics of Ferroelectric Domains," Adv. Electron. Mater. 8(6), 2100650 (2022).

31 A.P. Cismesia, G.R. Nicholls, and N.C. Polfer, "Amine vs. carboxylic acid protonation in ortho-, meta-, and para-aminobenzoic acid: An IRMPD spectroscopy study," J. Mol. Spectrosc. 332, 79–85 (2017).

32 I. Spasojevic, J. Santiso, J.M. Caicedo, G. Catalan, and N. Domingo, "Tunable Molecular Electrodes for Bistable Polarization Screening," Small 19(30), (2023).

33 B. Li, Y. Chen, Z. Liang, D. Gao, and W. Huang, "Interfacial engineering by using self-assembled monolayer in mesoporous perovskite solar cell," RSC Adv. 5(114), 94290–94295 (2015).

34 A.G. Thomas, M.J. Jackman, M. Wagstaffe, H. Radtke, K. Syres, J. Adell, A. Lévy, and N. Martsinovich, "Adsorption studies of p-aminobenzoic acid on the anatase TiO_2(101) surface," Langmuir 30(41), 12306–12314 (2014).

35 N.A. Spaldin, "Fundamental Size Limits in Ferroelectricity," Science (1979). 304(5677), 1606–1607 (2004).

36 J. Rodríguez Contreras, H. Kohlstedt, U. Poppe, R. Waser, C. Buchal, and N.A. Pertsev, "Resistive switching in metal–ferroelectric–metal junctions," Appl. Phys. Lett. 83(22), 4595–4597 (2003).

37 M.Ye. Zhuravlev, R.F. Sabirianov, S.S. Jaswal, and E.Y. Tsymbal, "Giant Electroresistance in Ferroelectric Tunnel Junctions," Phys. Rev. Lett. 94(24), 246802 (2005).

38 A. Gruverman, D. Wu, H. Lu, Y. Wang, H.W. Jang, C.M. Folkman, M.Y. Zhuravlev, D. Felker, M. Rzchowski, C.B. Eom, and E.Y. Tsymbal, "Tunneling electroresistance effect in ferroelectric tunnel junctions at the nanoscale," Nano Lett. 9(10), 3539–3543 (2009).

39 V. Garcia, and M. Bibes, "Ferroelectric tunnel junctions for information storage and processing," Nat. Commun. 5(1), 4289 (2014).

40 E.Y. Tsymbal, and H. Kohlstedt, “Tunneling Across a Ferroelectric,” Science (1979). 313(5784), 181–183 (2006).

41 D. Pantel, and M. Alexe, “Electroresistance effects in ferroelectric tunnel barriers,” Phys. Rev. B 82(13), 134105 (2010).

2 Growth optimization of $BaTiO_3/SrRuO_3$ heterostructures

Achieving reliable ferroelectric functionalities in thin films critically depends on the structural and morphological quality established during growth. Since parameters such as power, background pressure, temperature, and deposition rate play an interconnected role in determining adatom mobility, nucleation behavior, and interface coherence, these factors ultimately govern the transition from rough, three-dimensional islanded surfaces to uniform 2D layers. The quality of these films directly dictates the ferroelectric functionalities explored in later Chapters. In this Chapter, we therefore focus on the systematic optimization of growth conditions for $BaTiO_3/SrRuO_3$ (BTO/SRO) heterostructures, as a necessary foundation for achieving controlled switching dynamics, robust ferroelectric polarization retention in the ultrathin regime, and ultimately reliable tunneling electroresistance at the atomic scale.

2.1 Introduction

The growth of high-quality oxide thin films via physical vapor deposition methods depends critically on a set of fundamental parameters that can be controlled during deposition (such as substrate temperature, deposition rate, or deposition pressure).[1,2] These factors are strongly interdependent and therefore cannot be optimized in isolation. Their interplay not only determines the film's microstructure and properties but also guides the choice of the most suitable deposition technique for a given material system. In recent decades, several methods have been employed to grow complex oxide thin films, as comprehensively reviewed by Martin et al.[3] Among them, Pulsed Laser Deposition (PLD) and Radio Frequency (RF)-sputtering have emerged as two of the most widely used techniques. While both can produce high-quality epitaxial films, their process stability and reproducibility differ, which has direct implications for systematic growth optimization.

In PLD, maintaining reproducible growth conditions can be challenging because the laser fluence depends strongly on the condition of the excimer laser gas. The halogen donor gas is continuously consumed during operation, and by-products of the discharge reduce efficiency; therefore, periodic "refresh" injections or complete gas refills are required.[4,5] These fluctuations make it difficult to maintain constant fluence across multiple growth runs, thereby compromising precise control of the growth mode. Moreover, lowering the laser energy is not always a viable workaround, as the optimal fluence window is substrate-dependent, due to different growth kinetics for different substrates. By contrast, RF-sputtering offers intrinsically higher stability and control. The power delivered to the target is defined electronically and can be continuously monitored through the DC self-bias potential,[6] providing reproducible and finely tunable deposition conditions. This reliability makes RF-sputtering particularly well suited for systematic

growth optimization, where small variations in deposition parameters can be directly correlated with changes in film morphology and quality.

Besides the choice of growth technique, numerous studies have demonstrated that deposition parameters directly influence ferroelectric characteristics. For example, tuning growth pressure can alter tetragonality, polarization stability, and coercive fields,[7–9] while growth energy and rate have been shown to affect defect dipole formation, dielectric permittivity, and overall functional performance.[10,11] Beyond their impact on ferroelectric functionality, deposition parameters also govern the structural evolution of the films—determining how atoms nucleate, coalesce, and eventually form continuous layers. These factors control not only crystallinity but also surface morphology, interface quality, and reproducibility across samples. Understanding these growth mechanisms is therefore essential for obtaining smooth, uniform, and functionally reliable BTO/SRO heterostructures, which form the basis of the ferroelectric studies presented in later Chapters.

In this Chapter, we focus on the growth of BTO/SRO heterostructures by RF-sputtering, emphasizing the optimization of deposition conditions to achieve uniform coverage, smooth surfaces, and high-quality interfaces. Prior strain-analysis experiments performed by PLD (summarized in Appendix B) established a suitable lattice-mismatch window and guided the selection of substrates for the present sputtering work. However, for the extensive series of growths required to optimize deposition parameters and growth modes, RF-sputtering was adopted to ensure higher stability and reproducibility, thereby avoiding issues related to gas refilling and laser-energy fluctuations inherent to PLD. Building upon the insights gained from the PLD studies, this Chapter presents a detailed investigation of how growth parameters—such as pressure, power, and deposition time—govern nucleation, coalescence, and film smoothness. AFM was employed to

examine the resulting surface topographies and to identify the transition from rough, three-dimensional islanded growth toward smooth, two-dimensional layer-by-layer films. The optimized BTO/SRO heterostructures obtained under these conditions serve as the structural foundation for the ferroelectric analyses presented in the following Chapters.

2.2 RF-sputtering: growth behavior beyond strain effects

For the past few decades, growth of epitaxial oxide films under controlled oxygen partial pressure has been demonstrated.[12] Precise adjustment of parameters such as substrate temperature, background gas composition, and RF power enables the deposition of high quality ultrathin, stoichiometric, and epitaxial oxide layers. Sputtering is based on the physical ejection of atoms from a target via momentum transfer during bombardment by energetic ions, typically Ar^+. In RF-sputtering, the plasma is sustained by a radiofrequency field, and the oscillating potential allows charge-neutral operation while maintaining efficient ionization. A negative bias applied to the target accelerates Ar^+ ions toward it, initiating a collision cascade that ejects atoms with a broad energy distribution. To enhance the ionization efficiency, ring-shaped magnets (magnetrons) are employed to confine electrons near the target, thereby increasing the sputtering rate. The ejected species then condense on the substrate to form the thin film.[3,13–15]

2.2.1 Growth mode of SRO: transition from island formation to layer-by-layer

The epitaxial growth mode of thin films is governed by several factors, with the most critical being the thermodynamic driving force and the lattice misfit between the film and the substrate. The growth mode determines the nucleation process and subsequent film evolution, and

it has a direct impact on the resulting morphology and structural properties of the films. In the case of heteroepitaxial growth, three classical modes are typically observed (schematics are shown in Fig. 2.1) [16–18]:

- **Frank–van der Merwe:** layer-by-layer two-dimensional growth
- **Stranski–Krastanov:** initial wetting layer formation followed by three-dimensional island growth
- **Volmer–Weber:** direct three-dimensional island growth

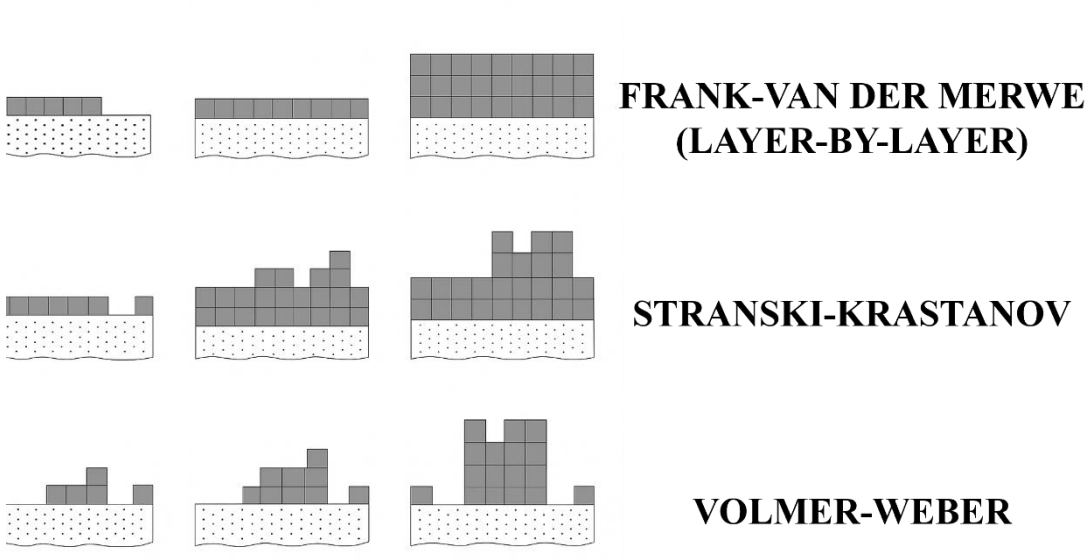


Figure 2.1 *Schematic illustration of the three classical thin-film growth modes: (a) Frank–van der Merwe (layer-by-layer), (b) Stranski–Krastanov (layer plus island), and (c) Volmer–Weber (island) growth. Adapted from Ref [17].*

During Frank–van der Merwe (layer-by-layer) growth, a new layer ideally nucleates only after the completion of the one beneath it, allowing step-flow over long distances. However, even under this mode, the formation of two-dimensional islands or multilayered mounds (often referred

to as "wedding-cake" structures) can occur. The likelihood of such stable island formation depends strongly on the adatom supersaturation. Since the flux of adatoms arriving from the gas phase is spatially homogeneous, any local supersaturation and inhomogeneity must arise from constraints in surface diffusion. The physical origin of this effect is the Ehrlich–Schwoebel (ES) barrier: an additional energy barrier that impedes adatoms from descending from an upper terrace to a lower one, as the transition state involves reduced coordination. This barrier introduces a kinetic instability into the nominally layer-by-layer growth, since adatoms diffusing across the surface tend to accumulate at step edges rather than cross them easily.[15,19–22] Previous studies have shown that increasing the substrate temperature can effectively reduce mound formation, as the enhanced adatom diffusivity helps overcome the ES energy barrier and promotes smoother step-flow growth.[15]

In the case of Volmer–Weber (island) growth, deposition begins with adsorption of vapor atoms on the substrate surface, followed by the agglomeration of adatoms into spatially separated nuclei. These islands grow in size, eventually impinge on one another, and coalesce to form larger structures. With continued deposition, the remaining inter-island gaps are gradually filled. This growth mode is typically driven by weak film–substrate interactions, where the surface energy of the film/substrate is lower than that of the deposited adatoms. As a result, Volmer–Weber growth is most often observed in weakly interacting film/substrate systems, where the film favors three-dimensional island formation over two-dimensional wetting layers.[23–25]

Stranski–Krastanov growth is generally considered an intermediate mode between Frank–van der Merwe and Volmer–Weber. Initially, deposition proceeds in a layer-by-layer fashion, producing atomically smooth layers characteristic of Frank–van der Merwe growth. However, as deposition continues, the coherently strained wetting layer accumulates elastic energy due to lattice

mismatch between the film and the substrate. Once the film thickness exceeds a critical value, this strain energy becomes energetically unfavorable, and the growth mode transitions abruptly to island formation, similar to Volmer-Weber growth. In epitaxial heterostructures with significant lattice mismatch, Stranski–Krastanov growth is therefore the most likely scenario, since the islanding process provides an efficient strain-relaxation mechanism beyond the critical thickness.[26,27]

We used off-axis RF magnetron sputtering to grow SRO thin films on $DyScO_3$ (DSO), using a 1.5-in. ceramic SRO target at 100 mTorr, in a constant Ar/O_2 flow of 24/16 sccm, with the substrate held at 635 °C, and an applied RF power of 30 W. Under these conditions, AFM topography images (Fig. 2.2) revealed a predominantly three-dimensional (3D) growth mode characterized by distinct islands and trenches (holes) between them. As discussed earlier in the context of Volmer–Weber growth, this morphology indicates that island coalescence and subsequent hole filling were not yet complete. Similar behavior has been reported for $La_{2/3}Ca_{1/3}MnO_3$ (LCMO) films on $SrTiO_3$ (STO) (110), where a pronounced 3D growth mode was observed and the island morphology was attributed to thermodynamic driving forces.[15] In such cases, Volmer-Weber growth arises when the substrate surface energy is lower than the combined surface and interface energies of the film, favoring the nucleation of separated islands rather than a continuous layer.[15] We hypothesize that continued deposition would eventually lead to coalescence, as has been observed in the later growth of BTO films (see Section 2.2.2).

To further explore this behavior, we investigated the effect of sputtering power on the evolution of the SRO growth mode. As shown in Fig. 2.2, increasing the RF power from the initial 30 W to 45 W —while proportionally reducing the deposition time to maintain comparable film thickness (approximately 30 nm)—led to a progressive improvement in morphology, evolving

from rough 3D islanded surfaces (Fig. 2.2a,b) toward smoother, step-like features consistent with layer-by-layer growth (Fig. 2.2c,d). This transition can be attributed to the increase in energetic ion flux at higher sputtering powers. More energetic ions enhance the sputtering yield at the target, thereby increasing the flux of adatoms arriving at the substrate.[28–30] At the same time, the other possibility is that the higher kinetic energy of arriving species promotes surface diffusion, allowing adatoms to migrate more effectively, fill valleys, and integrate into existing layers. At low sputtering power, by contrast, the reduced surface mobility favors stronger adatom–adatom bonding, which drives island nucleation. With increasing power, the balance shifts toward substrate–adatom bonding and continuous layer completion, resulting in the observed transition toward layer-by-layer growth.[30,31]

As summarized in Fig. 2.2(a–d), the progressive smoothing of the SRO surface with increasing sputtering power reflects a clear enhancement in adatom mobility and surface diffusion efficiency. The film deposited at 45 W exhibits the lowest roughness (RMS ≈ 0.2 nm) and well-defined step terraces, indicative of continuous, epitaxial growth. These conditions were therefore identified as optimal for achieving high-quality SRO bottom electrodes, providing smooth and structurally coherent templates for the subsequent growth of BTO/SRO heterostructures discussed in the following sections.

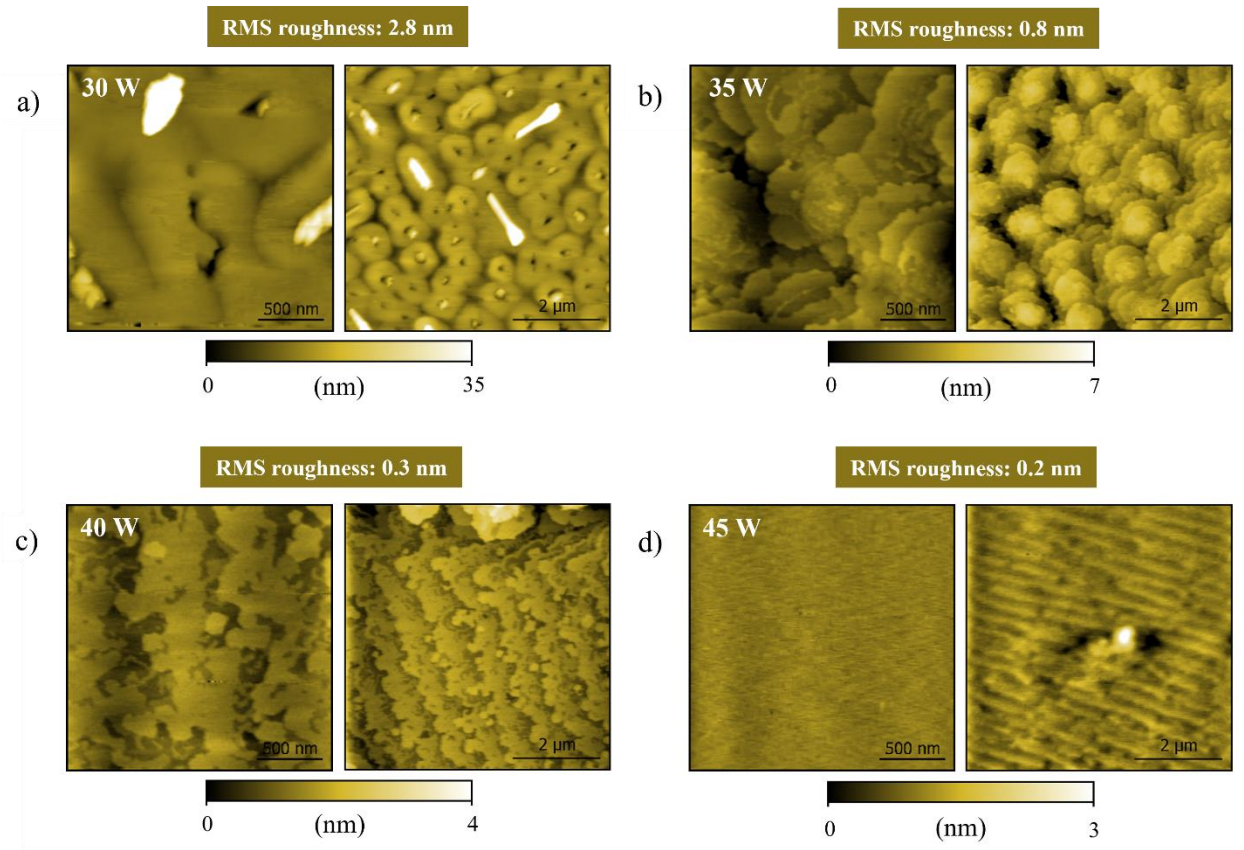


Figure 2.2 *AFM topography images of SRO films grown on DSO substrates under varying RF-sputtering powers: (a) 30 W, (b) 35 W, (c) 40 W, and (d) 45 W. At 30 W, the films exhibit a pronounced 3D Volmer–Weber–type growth mode with islanded morphology and trenches between grains. Increasing the sputtering power progressively improves the surface morphology, with 35 W and 40 W showing partial smoothing and step-like features, while 45 W yields the smoothest surface consistent with a transition toward layer-by-layer growth. Scan areas: left 2 × 2 µm², right 6 × 6 µm².*

2.2.2 Initial nucleation and growth stages of BTO thin films

With the optimized SRO growth conditions established, BTO films were subsequently deposited on top using initial sputtering parameters of 55 W, 50 mTorr, and 650 °C. These conditions were selected to achieve an acceptable growth rate, since the growth kinetics of BTO were considerably slower than those of SRO when using the same background pressure of 100 mTorr. Under these conditions, a 180 min deposition yielded films of approximately 18 nm

thickness (as checked via High Resolution X-ray Diffraction (HR-XRD) measurements discussed in Chapter 3). AFM topography revealed smooth surfaces with well-developed two-dimensional (2D) layer-by-layer morphology (Fig. 2.3a).

To have a series as a function of thickness, we next reduced the deposition time while keeping the growth conditions fixed. As expected, the resulting thicknesses decreased with deposition time ranging from approximately 18 nm (180 min) down to about 2.5 nm (40 min), (details discussed in Chapter 4, where polarization switching is investigated as a function of thickness); however, AFM images revealed a change in surface morphology at reduced thicknesses (Fig. 2.3). Specifically, while the thicker films (180 and 120 min) showed continuous layers, thinner films exhibited increasingly rough surfaces. The 60 min sample displayed partial separation between multilayer islands, and for the 40 min deposition the morphology resembled the low-power SRO case described previously—namely, distinct 3D islands and trenches with incomplete coalescence. At this stage, further reduction in thickness under the same growth conditions was discontinued. The films shown in Fig. 2.3 were therefore used as reference samples for subsequent ferroelectric studies presented in Chapters 3 and 4, where their polarization behavior was examined in relation to film thickness. For thinner films, additional optimization of the growth conditions was required, as discussed in the following sections of this Chapter.

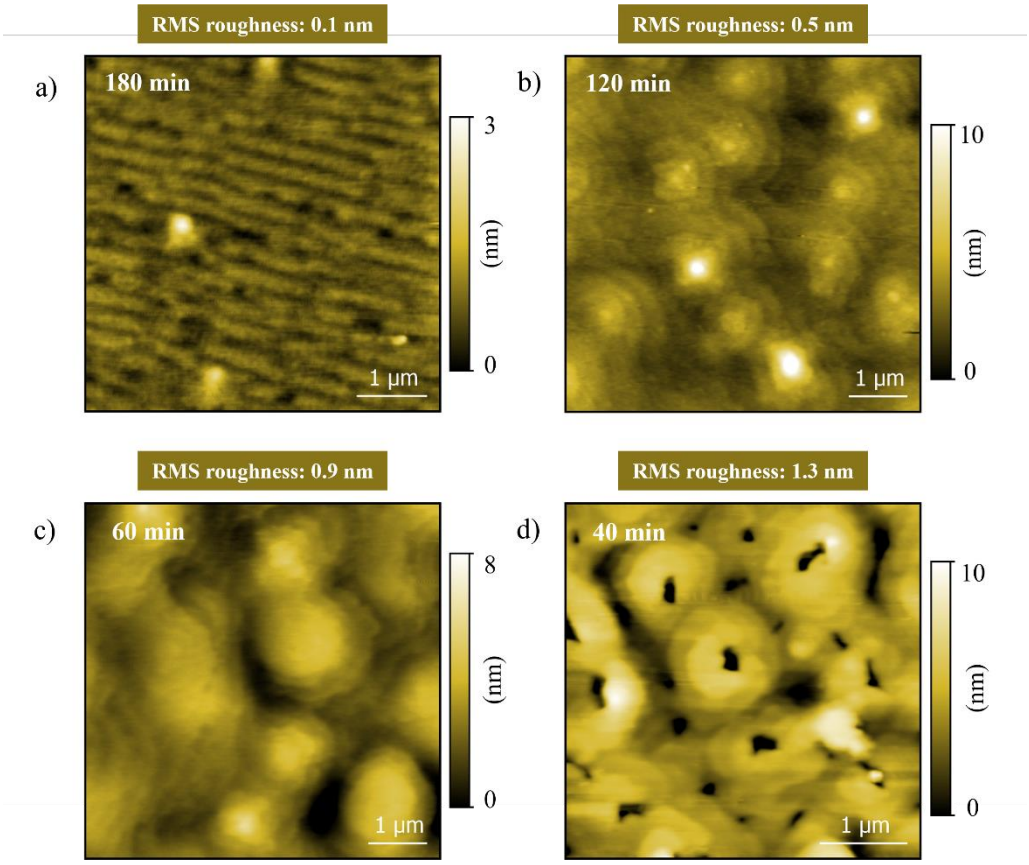


Figure 2.3 *AFM topography images of BTO films grown on SRO/DSO under identical sputtering conditions (55 W, 50 mTorr, 650 °C) with deposition times of (a) 180 min, (b) 120 min, (c) 60 min, and (d) 40 min. The corresponding RMS roughness values for the areas marked by white squares are indicated in each image. The thicker films (a, b) show smooth, continuous surfaces characteristic of 2D layer-by-layer growth, whereas shorter deposition times (c, d) yield rougher morphologies. The 60 min film exhibits partial separation between multilayer islands, while the 40 min film displays distinct 3D islands and trenches with incomplete coalescence.*

Based on the earlier SRO results, increasing sputtering power could in principle promote formation of a continuous layer or a transition back toward 2D growth by enhancing surface mobility. However, because BTO has intrinsically slower growth kinetics, modest power increases were unlikely to produce the desired effect, and higher powers were deliberately avoided to prevent possible damage or nonstoichiometry. Instead, a different strategy was pursued: reducing the

background pressure while keeping the RF power constant. Lowering the pressure increases the kinetic energy of the sputtered species, effectively mimicking the effect of increased power while maintaining controlled growth conditions. This adjustment was expected to promote smoother film growth and improved coalescence and enhanced adatom mobility.

Using this approach, a new series of ultrathin BTO samples was grown at 25 mTorr with deposition times of 5, 10, and 20 minutes. Cross-sectional High Resolution Transmission Electron Microscopy (HR-TEM) confirmed that the 10 min deposition corresponded to a thickness of 2-unit cells (discussed in detail in Chapter 5). Importantly, AFM topography of all three samples (Fig. 2.4) showed complete, continuous layers, with only minor step meandering. This indicates that reducing the pressure successfully altered the growth mode, suppressing island formation and favoring direct 2D layer growth even at ultrathin thicknesses. Our observations are in agreement with earlier reports showing that increasing the sputtering/growth pressure can induce a transition from 2D layer-by-layer growth toward a Volmer–Weber growth regime with island formation, accompanied by an increase in surface roughness.[32,33] Therefore, under these optimized low-pressure conditions, films grown for up to 20 minutes exhibited smooth and continuous surfaces, confirming the stability of the growth mode within this range. The thickness series shown in Fig. 2.4 were subsequently employed for ultrathin BTO measurements discussed in Chapter 5.

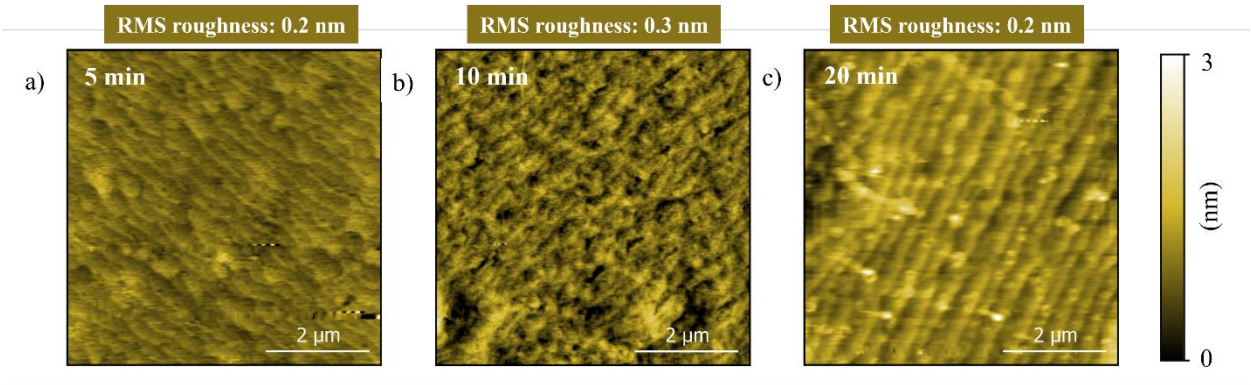


Figure 2.4 *AFM topography images of ultrathin BTO films grown on SRO/DSO at 55 W and reduced pressure of 25 mTorr for deposition times of a) 5, b) 10, and c) 20 min. All samples exhibit smooth, continuous layers with only minor step meandering, indicating suppression of island nucleation and stabilization of a 2D layer-by-layer growth mode even at ultrathin thicknesses.*

2.3 Concluding remarks

Overall, these studies highlight that the interplay between growth parameters—pressure, power, and deposition time—is the key factor governing film morphology. Rather than relying on a single fixed recipe, the growth pathway should be adapted dynamically based on the evolving status of the film.

1. 3D islands with trenches can reflect incomplete Volmer–Weber evolution. If roughness stems from uncompleted coalescence/hole filling, increasing the growth rate through higher sputtering power can yield a continuous film (as observed in growth optimization of SRO).

2. At fixed flux, increased growth time can also close trenches. In BTO thickness series grown at constant power/rate, extending deposition time finished coalescence and produced continuous layers.

3. Reducing the background pressure increases the kinetic energy and narrows the angular spread of the arriving species, enhancing surface diffusion and effectively mimicking the effect of higher sputtering power by increasing the flux of energetic species reaching the substrate. This leads to a transition toward smoother, more continuous films and a shift from three-dimensional to two-dimensional growth behavior.

References

1 P.R. Willmott, “Deposition of complex multielemental thin films,” Prog Surf Sci 76(6–8), 163–217 (2004).

2 G.K. Hubler, and J.A. Sprague, “Energetic particles in PVD technology: particle-surface interaction processes and energy-particle relationships in thin film deposition,” Surf Coat Technol 81(1), 29–35 (1996).

3 L.W. Martin, Y.H. Chu, and R. Ramesh, “Advances in the growth and characterization of magnetic, ferroelectric, and multiferroic oxide thin films,” Materials Science and Engineering R: Reports 68(4–6), 89–133 (2010).

4 K. O’Brien, W. Dunstan, R. Jacques, and D. Brown, “Lithography line productivity impact using Cymer GLX technology,” in *Optical Microlithography XXII*, (SPIE, 2009), p. 72743N.

5 A. Garscadden, M.J. Kushner, and J.G. Eden, “Plasma physics issues in gas discharge laser development,” IEEE Transactions on Plasma Science 19(6), 1013–1031 (1991).

6 L.T. Lamont, and F.T. Turner, “ROLE OF DC SELF-BIAS POTENTIAL IN THE CONTROL OF RF SPUTTERING.,” in *J Vac Sci Technol*, (1974), pp. 47–51.

7 Y. Jiang, E. Parsonnet, A. Qualls, W. Zhao, S. Susarla, D. Pesquera, A. Dasgupta, M. Acharya, H. Zhang, T. Gosavi, C.-C. Lin, D.E. Nikonov, H. Li, I.A. Young, R. Ramesh, and L.W. Martin, “Enabling ultra-low-voltage switching in BaTiO3,” Nat Mater 21(7), 779–785 (2022).

8 J.P.B. Silva, K.C. Sekhar, A. Almeida, J. Agostinho Moreira, M. Pereira, and M.J.M. Gomes, “Effects of oxygen partial pressure on the ferroelectric properties of pulsed laser deposited Ba0.8Sr0.2TiO3 thin films,” Appl Phys A Mater Sci Process 113(3), 817–824 (2013).

9 J.H. Huang, L. Yang, L.Q. Wei, T. Wang, W.C. Fan, K. Qu, Z. Guan, B. Bin Chen, P.H. Xiang, C.G. Duan, and N. Zhong, “Influence of oxygen pressure on the ferroelectricity of pulsed laser deposition fabricated epitaxial Y-doped HfO2,” J Appl Phys 136(1), (2024).

10 A. Dasgupta, S. Saremi, X. Ruijuan, L.R. Dedon, S. Pandya, A.R. Damodaran, and L.W. Martin, “Nonstoichiometry, structure, and properties of Ba1−xTiOy thin films,” J Mater Chem C Mater 6(40), 10751–10759 (2018).

11 A.R. Damodaran, E. Breckenfeld, Z. Chen, S. Lee, and L.W. Martin, “ Enhancement of Ferroelectric Curie Temperature in BaTiO 3 Films via Strain-Induced Defect Dipole Alignment ,” Advanced Materials 26(36), 6341–6347 (2014).

12 M. Dawber, “Sputtering techniques for epitaxial growth of complex oxides,” in *Epitaxial Growth of Complex Metal Oxides*, (Elsevier, 2015), pp. 31–45.

13 P.R. Willmott, and J.R. Huber, *RMP Colloquia Pulsed Laser Vaporization and Deposition* (n.d.).

14 P.J. Kelly, and R.D. Arnell, "Magnetron sputtering: a review of recent developments and applications," Vacuum 56(3), 159–172 (2000).

15 I. Cañero Infante (Author), F. Sánchez Barrera (Director), and J. Fontcuberta i Griñó (Director), (001) and (110) La 2/3 Ca 1/3 MnO 3 Epitaxial Ferromagnetic Electrodes: A Comparative Study, 2008.

16 J.W. Evans, Y. Han, B. Ünal, M. Li, K.J. Caspersen, D. Jing, A.R. Layson, C.R. Stoldt, T. Duguet, P.A. Thiel, W. Wang, K. Tsukamoto, and D. Wu, "From Initial to Late Stages of Epitaxial Thin Film Growth: STM Analysis and Atomistic or Coarse-Grained Modeling," (American Institute of Physics, 2010), pp. 26–44.

17 Hans. Scheel, and Tsuguo. Fukuda, *Crystal Growth Technology* (Wiley, 2005).

18 H. Brune, "Epitaxial Growth of Thin Films," in *Surface and Interface Science*, (Wiley-VCH Verlag GmbH & Co. KGaA, Weinheim, Germany, 2014), pp. 421–492.

19 M.G. Lagally, and Z. Zhang, "Thin-film cliffhanger," Nature 417(6892), 907–909 (2002).

20 J. Krug, "Four lectures on the physics of crystal growth," Physica A: Statistical Mechanics and Its Applications 313(1–2), 47–82 (2002).

21 P. Politi, G. Grenet, A. Marty, A. Ponchet, and J. Villain, "Instabilities in crystal growth by atomic or molecular beams," Phys Rep 324(5–6), 271–404 (2000).

22 A. Redkov, "Impact of Schwoebel Barriers on the Step-Flow Growth of a Multicomponent Crystal," Crystals (Basel) 14(1), 25 (2023).

23 J. Colin, A. Jamnig, C. Furgeaud, A. Michel, N. Pliatsikas, K. Sarakinos, and G. Abadias, "In situ and real-time nanoscale monitoring of ultra-thin metal film growth using optical and electrical diagnostic tools," Nanomaterials 10(11), 1–30 (2020).

24 A. Jamnig, N. Pliatsikas, M. Konpan, J. Lu, T. Kehagias, A.N. Kotanidis, N. Kalfagiannis, D. V. Bellas, E. Lidorikis, J. Kovac, G. Abadias, I. Petrov, J.E. Greene, and K. Sarakinos, "3D-to-2D Morphology Manipulation of Sputter-Deposited Nanoscale Silver Films on Weakly Interacting Substrates via Selective Nitrogen Deployment for Multifunctional Metal Contacts," ACS Appl Nano Mater 3(5), 4728–4738 (2020).

25 V. Elofsson, B. Lü, D. Magnfält, E.P. Münger, and K. Sarakinos, "Unravelling the physical mechanisms that determine microstructural evolution of ultrathin Volmer-Weber films," J Appl Phys 116(4), (2014).

26 J.Q. He, E. Vasco, R. Dittmann, and R.H. Wang, “Growth dynamics and strain relaxation mechanisms in BaTiO3 pulsed laser deposited on SrRuO3 SrTiO3,” Phys Rev B Condens Matter Mater Phys 73(12), (2006).

27 J.E. Prieto, and I. Markov, “Stranski–Krastanov mechanism of growth and the effect of misfit sign on quantum dots nucleation,” Surf Sci 664, 172–184 (2017).

28 M.T. Le, Y.U. Sohn, J.W. Lim, and G.S. Choi, “Effect of sputtering power on the nucleation and growth of Cu films deposited by magnetron sputtering,” Mater Trans 51(1), 116–120 (2010).

29 C. Zhou, T. Li, X. Wei, and B. Yan, “Effect of the Sputtering Power on the Structure, Morphology and Magnetic Properties of Fe Films,” Metals (Basel) 10(7), 896 (2020).

30 F.M. Mwema, J.M. Wambua, T.-C. Jen, and E.T. Akinlabi, “Influence of Sputtering DC Sputtering Power on the Surface Evolution of Ti Thin Films: A Fractal Description,” JOM 77(2), 564–577 (2025).

31 S. Müller-Pfeiffer, H. -J. Anklam, and W. Haubenreisser, “A Generalized Ballistic Aggregation Model for the Simulation of Thin Film Growth with Special Consideration of Nodular Growth,” Physica Status Solidi (b) 160(2), 491–504 (1990).

32 A. Aidoud, T. Maroutian, S. Matzen, G. Agnus, B. Amrani, K. Driss-Khodja, P. Aubert, and P. Lecoeur, “Tuning the growth and strain relaxation of ferroelectric BaTiO3 thin films on SrRuO3 electrode: Influence on electrical properties,” EPJ Applied Physics 80(3), (2017).

33 G. Zhu, M. Han, B. Xiao, and Z. Gan, “Influence of Sputtering Pressure on the Micro-Topography of Sputtered Cu/Si Films: Integrated Multiscale Simulation,” Processes 11(6), 1649 (2023).

3 Polarization switching dynamics of para-aminobenzoic acid-functionalized $BaTiO_3$ thin films

The presence of unscreened polarization at the surface of ferroelectric thin films can impair their functional response. One recently proposed way to improve screening is by using "molecular electrodes": molecules with chemically resonant bonds (i.e. energy-equivalent internal distributions of chemical bonds), such that their internal charge distribution can adapt to different depolarizing fields. However, while molecular electrodes can provide for a good electrostatic screening, we do not know what their dynamic response is, and in particular whether they allow for agile switching of ferroelectric polarization. Here, we compare the switching dynamics of BTO epitaxial thin films with and without a surface layer of pABA, a molecular electrode with a bipolar screening capacity. We test domain-writing dynamics by running the biased tip of PFM across the surface of the ferroelectric films at increasing scanning speeds and studying the continuity and width of the written domains.

3.1 Introduction

An important issue for using ferroelectrics in devices such as non-volatile memories[1,2] is their switching dynamics, i.e., the rate at which the polarization state can be reversed under an applied electric field. Initial studies focused on switching-induced displacement currents in capacitor devices with metallic top and bottom electrodes. From these studies two things became clear: (i) very thin ferroelectric capacitors often show reduced polarization retention because the finite screening length of metallic electrodes leads to depolarization fields. These fields cause the ferroelectric thin film to break into tiny antiparallel domains, reducing the net bound charge and depolarization energy.[1,3,4] (ii) the switching dynamics in capacitor devices can be limited by the screening dynamics, that is the speed at which compensating charges for depolarizing fields can be supplied to the electrodes.

Microscopy-based investigations of switching dynamics highlighted another factor: the dynamics of domain nucleation and growth. In a seminal work led by Rodriguez et al.[5], sidewise domain growth in $LiNbO_3$ single crystals was studied by measuring lateral domain size as a function of the amplitude the duration of a voltage pulse, demonstrating that domain kinetics can be described as an activation process consistent with the Miller–Weinreich model[6], which provides the microscopic basis for Merz's law. In this model, the AFM tip-induced field distribution was approximated by a charged sphere.[7] A later study extended the theory for ultrathin crystals by incorporating (i) difference in depolarization energy compared to bulk crystals and (ii) the role of a surface water layer.[8] Substituting this improved field description into the Miller–Weinreich framework allowed to calculate the dependence of equilibrium domain radius on the applied tip voltage. Building on these insights, Brugère et al.[9] developed a model for domain growth in single-crystal $LiTaO_3$ that emphasized the effect of a conductive adsorbed layer on the surface. They

proposed that tip-induced domain growth is governed not by thermal activation of domain-wall motion, but rather by the temporal expansion of the local electric field driven by the conductivity of the water layer, thereby also demonstrating the strong influence of ambient humidity. Around the same time, Shur et al.[10] investigated domain growth in $LiNbO_3$ crystals, likewise highlighting the essential role of adsorbed surface layers in screening depolarization fields.

These concepts were also studied in thin films. Paruch et al.[11] and Tybell et al.[12] showed that domain-wall rates in $Pb(Zr_{0.2}Ti_{0.8})O_3$ (PZT) thin films follow a creep-like behavior at low electric fields, representing a modified form of Merz's law in which the dynamic exponent (μ) deviates from unity. Their findings indicated that the stochastic nucleation model of Miller and Weinreich alone cannot fully account for the observed dynamics. The nonlinear propagation of domain walls in epitaxial thin films across different regimes (creep, depinning, and flow) was subsequently clarified in detail by Jo et al.[13,14] Importantly, the influence of humidity also emerged in thin-film studies: in a later work, Paruch et al. demonstrated that subcritical switching dynamics in PZT thin films are strongly dependent on ambient humidity, underscoring the key role of surface adsorbates as dynamic screening charges rather than attributing creep solely to defects and pinning sites.[15]

More recently, Spasojević et al.[16] investigated the switching dynamics of BTO thin films under varying humidity and showed a strong dependence of the dynamic exponent on relative humidity, which cannot be only explained by defects in creep regime, again supporting the crucial role of surface adsorbates. These studies collectively establish that the dynamics of domain growth during polarization switching are governed by a delicate balance between the rate of screening charge accumulation and the speed of domain wall motion.[17] Such studies have consistently

reported the existence of a critical writing speed beyond which homogenous domain formation is inhibited, and thus ferroelectric "bits" cannot be reliably switched.

Having established the importance of atmospheric adsorbates in electrostatically screening depolarizing fields in thin films, and in governing domain-wall motion and growth, it must also be recognized that they pose a dynamic challenge: upon switching, the chemisorbed charge needs to change sign to adapt to the reversal of polarization, and this requires redistribution of surface adsorbates, which in general involves slow processes. As discussed in the Introduction Chapter, an alternative strategy is to use chemically resonant structures that provide a superior screening capacity for both polarization states. One promising candidate as proposed by Spasojević et el.[18] is pABA, that can effectively act as a "molecular electrode" providing comparable and, in some regimes, superior effective screening of polarization charge than metallic electrodes. However, in order to be useful in electronic devices, namely FeRAM where processing times are critical, the rate at which this molecular electrode provides the charge must be fast enough. So far, the polarization switching dynamics of ferroelectrics integrating molecular electrodes has not been explored.

In this Chapter, we investigate the switching dynamics of bare BTO films, and their counterparts functionalized with pABA molecular electrodes. Our results demonstrate that pABA molecular layers enable much faster switching of ferroelectric thin films compared to atmospheric adsorbates. This enhancement is evidenced by the improved stability of written domains under fast writing conditions (scan speeds of approximately 1 mm/s) and the formation of larger domain sizes at lower scan speeds.

3.2 Functionalization of BTO with pABA molecular layers: transfer process and spectroscopic characterization

Functionalization of our BTO samples with pABA molecular layers was carried out using a stamping method employing polydimethylsiloxane (PDMS). A schematic of the transfer process is shown in Fig. 3.1a. This approach allowed coverage of relatively large, millimeter-scale areas, enabling a quantitative evaluation of the molecular screening effects on domain-wall kinetics over a wide range of writing speeds and voltages. The pABA solution was prepared following the recipe of Spasojevic et al.[18] where pABA solution (0.1 M) was prepared by dissolving sublimation-purified pABA (≥99%, Sigma-Aldrich) in gamma-butyrolactone (GBL, ReagentPlus, ≥99%, Sigma-Aldrich). Due to the hygroscopic nature of pABA, all reagents were handled and the solution prepared inside a controlled-humidity glovebox. FT-IR was performed to confirm the successful attachment of pABA molecules to the BTO surface (Fig. 3.1b). The peaks observed at 1641 and 1434 cm^{-1} correspond to the symmetric and asymmetric vibrations of C=O bond from the carboxylic group (COOH), which remains intact. This indicates that bonding to the BTO surface occurs through monodentate linkage following COOH deprotonation.[18–20] The remaining peaks at 3368, 2339, 1320 and 1228 cm^{-1} are identified as the stretching vibrations of -OH group of unbonded molecules, $-NH_2$, and C-O groups respectively.

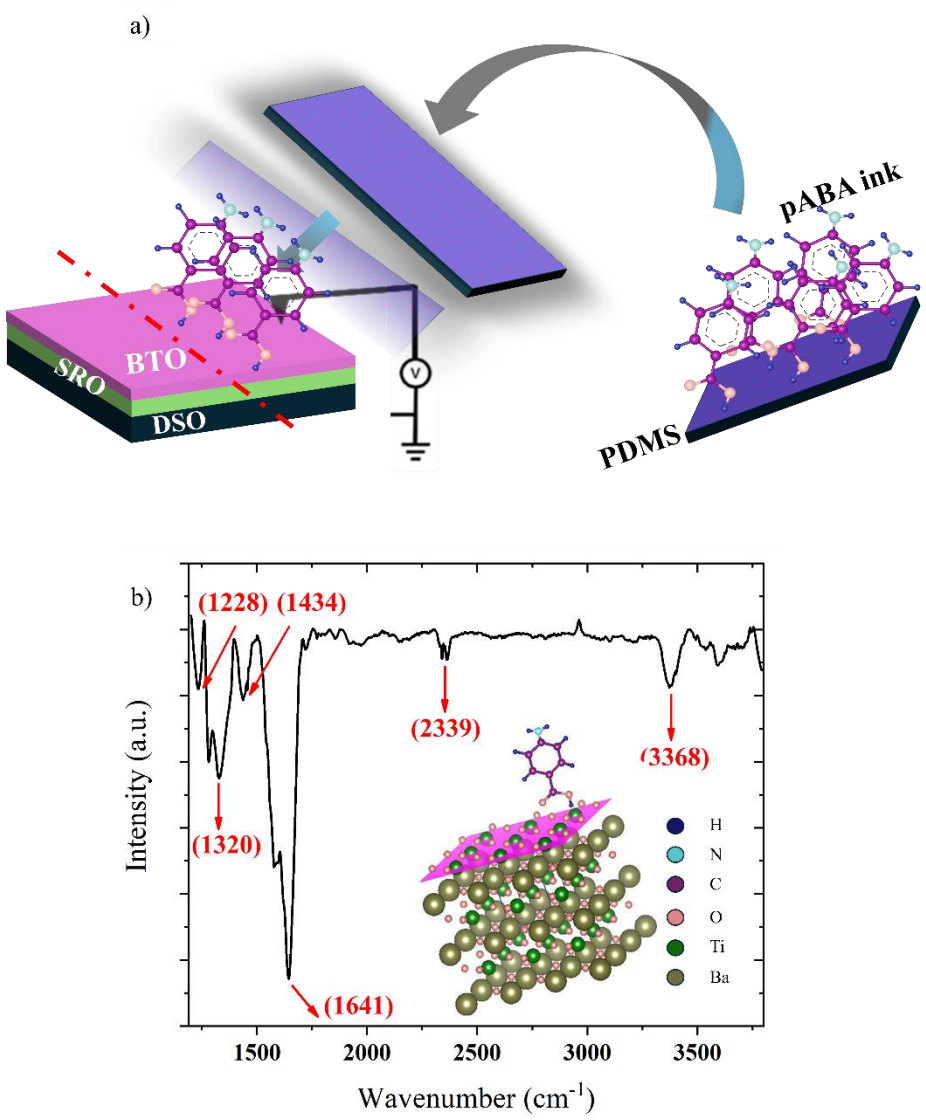


Figure 3.1 *(a) Schematic illustration of the transfer process for functionalizing BTO thin films with pABA using a PDMS stamp coated with pABA ink. Molecular attachment occurs through COOH deprotonation and monodentate bonding to surface Ti sites. (b) FT-IR spectrum of pABA-functionalized BTO showing characteristic vibrational peaks at 1641 and 1434 cm⁻¹ (C=O stretching of COOH), and at 3368, 2339, 1320, and 1228 cm⁻¹ (–OH, –NH₂, and C–O vibrations). The inset depicts a schematic of a pABA molecule chemisorbed on the BTO surface.*

3.3 Initial domain configuration and polarization state before and after pABA functionalization

Most often, studying initial domain configurations and domain wall dynamics is achieved by applying voltage pulses of different magnitudes and durations to the conductive tip of AFM in contact with the ferroelectric film surface, and measuring the size of the thus-written domains via PFM.[12,15,16,21] In our measurements, PtIr-coated PPP-EFM tips (Nanosensors) with an elastic constant k = 2.8 N/m were used. The cantilever was driven near its contact resonance (300–400 kHz) with an AC voltage of 800 mV to improve the signal-to-noise ratio and maximize sensitivity to the piezoresponse signal.[22] The samples used for these studies were epitaxial BTO (18 nm)/SRO (30 nm) thin-film heterostructures, grown on (110)-oriented DSO substrates using off-axis RF-sputtering, with the optimized growth conditions at a pressure of 50 mTorr, discussed in Chapter 2. Structural XRD characterization of these films (Fig. 3.2a) indicates an out-of-plane lattice expansion of the tetragonal BTO unit cell (c-axis lattice parameter of 4.187 Å), consistent with the compressive in-plane strain induced by the substrate. Laue oscillations around the BTO and SRO peaks are indicative of high crystalline quality.[23] The domain structure and polarization switching of BTO was investigated with PFM. Within the AFM resolution (~10 nm), no domain contrast was observed in the as-grown film. The initial polarization state of the films was investigated by the application of a DC bias of +10 V between the AFM tip and the SRO electrode. A 180-degree phase contrast was observed, indicating that the polarization of the as-grown film, here after called bare BTO, was initially pointing upward and switched to downward by a positive voltage (Fig. 3.2b). In the next step, the pABA molecules were transferred to the BTO film, and PFM writing measurements were repeated on the functionalized areas to verify that the polarization orientation of the films remained unchanged by the pABA. As shown in Fig. 3.2b, a clear 180° phase contrast

is observed between the downward-poled domain and the surrounding unpoled area, confirming polarization switching. Notably, the domain walls in the pABA-functionalized regions appear sharper and better defined compared to those in the bare BTO areas, which may indicate improved electrostatic screening at the surface and enhanced stabilization of the switched domains due to the presence of the molecular layer.[24]

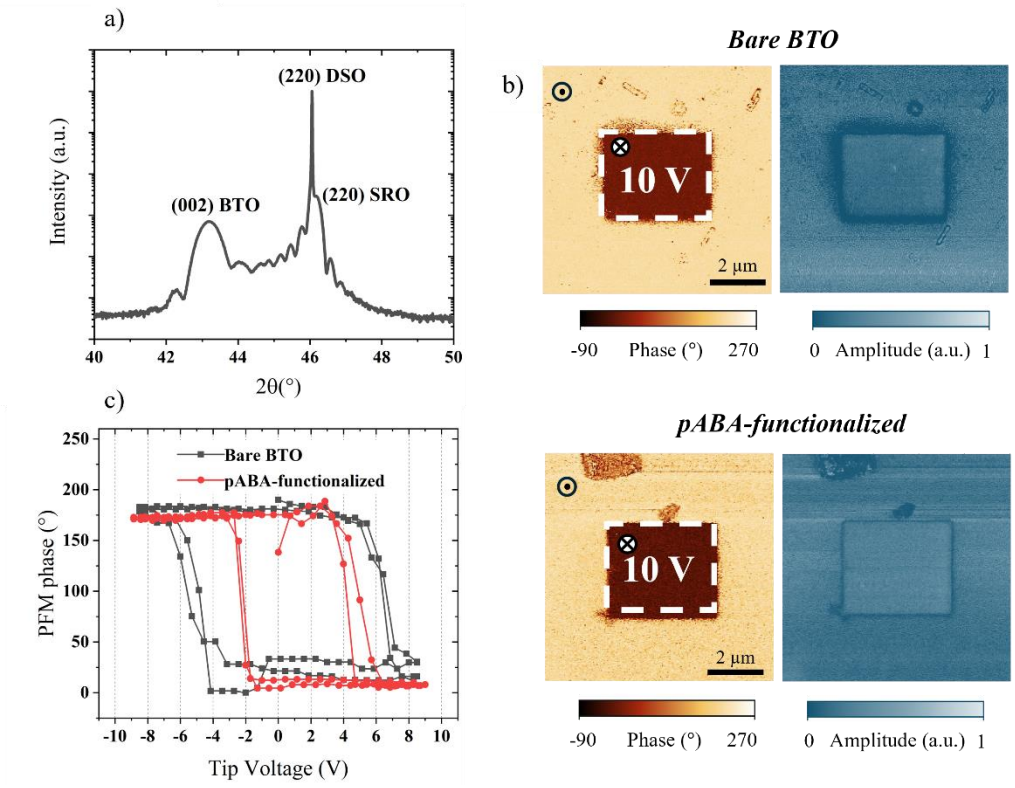


Figure 3.2 *(a) XRD scan of BTO/SRO/DSO films. (b) PFM phase (left) and amplitude (right) images of +10 V-written domains on bare (top panel) and pABA-functionalized BTO (bottom panel) thin films. A clear 180° phase contrast confirms polarization reversal in both cases, while the sharper domain boundaries observed in the pABA-functionalized region indicate enhanced electrostatic screening and improved domain stability. (c) Representative SS-PFM phase–voltage hysteresis loops measured at 1 Hz for bare (black) and pABA-functionalized (red) BTO films. Both exhibit robust ferroelectric switching, with the functionalized surface showing a lower coercive voltage.*

Hysteresis loops were subsequently collected in Switching Spectroscopy PFM (SS-PFM) at a frequency of 1 Hz, and representative curves were selected based on multiple acquisitions (Fig. 3.2c). Both bare and pABA-functionalized BTO show robust ferroelectric hysteresis, with a lower coercive voltage for the functionalized surface. This can be interpreted as faster domain wall motions during lateral growth stage of domain formation process.[16]

3.4 Writing speed analysis

A key parameter for quantifying ferroelectric switching dynamics is the critical writing speed, i.e., the minimum scanning rate at which stable and continuous domain structures can be written; above this speed, the polarization can no longer be reliably reversed. Writing speed provides practical insight into how quickly polarization reversal can be driven in real nanoscale switching scenarios. Therefore, in the following section, we compare the domain-writing performance of bare and pABA-functionalized BTO surfaces as a function of tip scan rate in order to determine both the critical writing speed for continuous domain formation and the dynamics of domain wall propagation.

3.4.1 Critical writing speed for homogenous domain formation

To evaluate the critical writing speed, we performed a set of lithography experiments for both bare and pABA-functionalized BTO, by applying a constant DC bias to the AFM tip while scanning across the film surface at progressively increasing tip velocities. This method has enabled us to construct a map of domain size evolution.[16] Linear domains were tentatively written using the MacroBuilder feature of the AFM software, with two different sets of scans: The slow regime

with speeds varying from 0.3 up to 12 μm/s and also the fast regime with the range of 21 up to 780 μm/s. Subsequent PFM mapping of the written areas allowed us to measure the existence, continuity, and width of the switched polarization stripes. We selected three writing voltages: 5 V (near the coercive voltage of the pABA-functionalized part of the film), 7 V (near the coercive voltage of the bare BTO) and 10 V (beyond the saturation voltage for both bare and pABA parts). For bare BTO, we observe that, for 5V (sub-coercive voltage for the bare BTO), line domains can only be written for the slow scan regime (Fig. 3.3a). As we increase the applied voltage (Fig. 3b,c), the written domains become wider, as observed in the phase contrast, the domain walls become clearer, and the critical speed required to observe continuous stripes is slightly increased; however, we still cannot successfully switch polarization homogeneously in linear domains for scanning speeds faster than 35 μm/s in the fast scan regime. Since the reproducibility of these results was verified across multiple scans, and both the slow and fast regimes were performed consecutively, we can rule out experimental artifacts such as tip degradation. The speed limitation in the bare BTO area is attributed to the reduced mobility of adsorbed water molecules and ionic species such as hydroxyl groups that provide the atmospheric screening charges at the surface.[16] Upon switching, the slow timescales associated to molecule rotation and reassembly of the ionic charges limit the time required to stabilize the switched domains.[25]

In contrast, in the pABA-functionalized part of the same BTO film, PFM phase and amplitude images show that continuous domains can be written up to the maximum speed reachable with our scan size (780 μm/s), and across all voltages (Fig. 3.3d-f). This indicates that pABA molecules enable domain writing at much faster speeds than in bare BTO in atmospheric conditions (where a critical speed of 35 μm/s was identified), by a factor of at least 22 (=780/35) when writing at 10V. This fast switching is enabled by the fast electronic charge reconfiguration

between different resonant structures of pABA, which can provide the requisite screening without having to change their molecular orientation.[18]

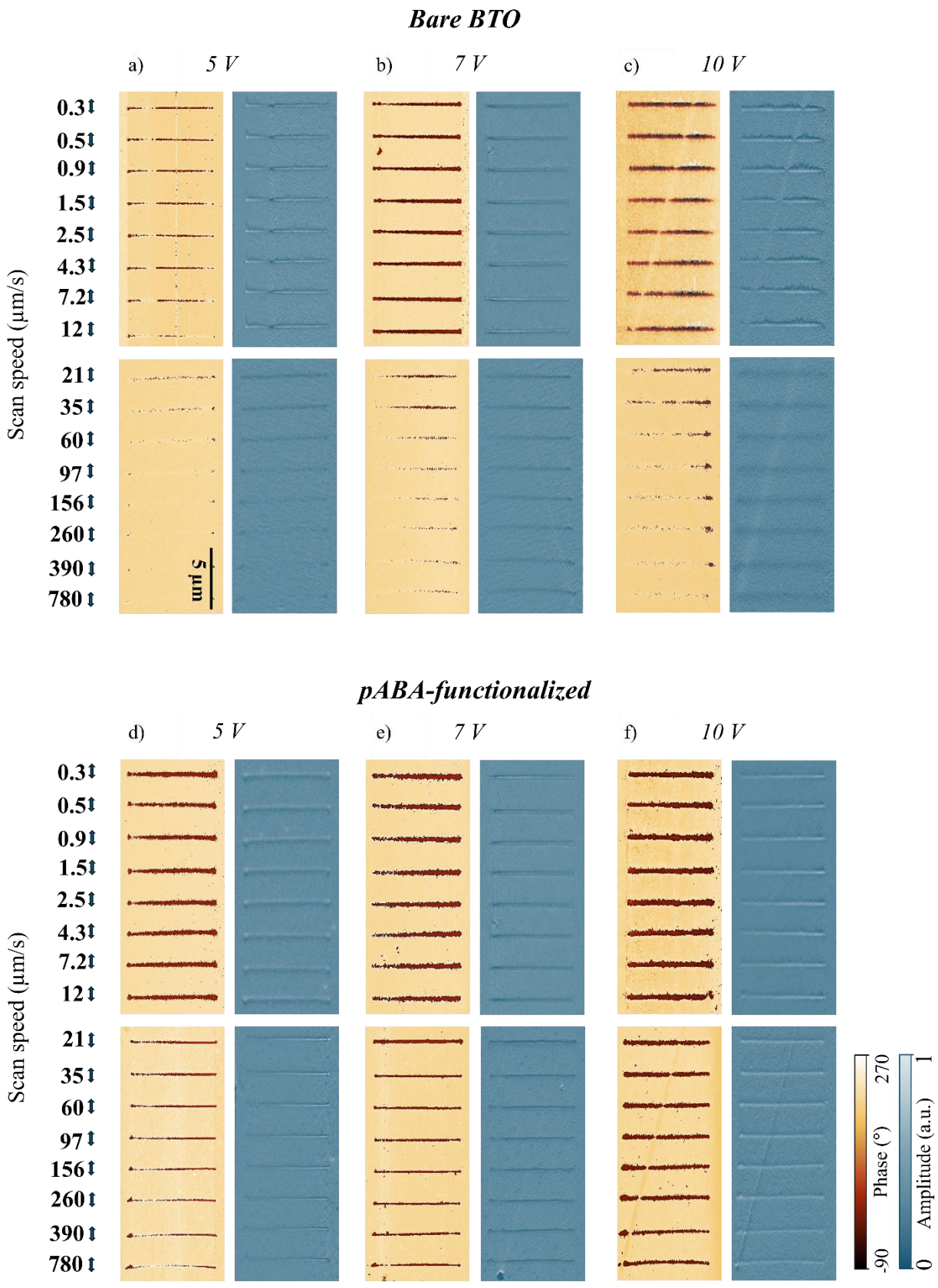

Bare BTO
a) 5 V
b) 7 V
c) 10 V
Scan speed (µm/s)
0.3
0.5
0.9
1.5
2.5
4.3
7.2
12
21
35
60
97
156
260
390
780
5 µm
pABA-functionalized
d) 5 V
e) 7 V
f) 10 V
Phase (°)
-90
270
Amplitude (a.u.)
0
1

Figure 3.3 *PFM phase (left) and amplitude images (right) of ferroelectric line domains switched to down polarization by increasing writing speeds at a constant tip bias of 5, 7, and 10 V for bare BTO (a-c), and pABA-functionalized BTO (d-f).*

3.4.2 Dynamics of domain wall propagation

In addition to the differences in critical writing speed discussed above, we also observe a systematic change in the domain size written at a given tip velocity. Specifically, the domains written on the pABA-functionalized BTO are wider than those written on bare BTO under the same writing conditions. To quantify the kinetics of domain growth for our biggest applied voltage (10 V), the average domain widths were extracted from PFM phase images by calculating the switched areas (based on pixel counts) and dividing them by the domain line length. These values were plotted on a log-log scale, and found to follow a power law (Fig. 3.4a), which was fitted using the equation (3.1),

$$Log\ (W) = \emptyset Log\ (S) - k \tag{3.1}$$

where W, S and $\emptyset$ denote average domain width, scan speed, and growth exponent respectively, and k is the logarithm of the proportionality constant in the power law. Since writing time is inversely proportional to scan speed, this result indicates that domain size scales as a power of writing time, [9,16] consistent with the idea that domain switching follows avalanche dynamics.[26] As shown in Fig. 3.4a, the slope of the fitted lines, corresponding to the growth exponent, is calculated as -0.04 and -0.29 for pABA-functionalized and bare BTO respectively. The near-zero growth exponent for the pABA-functionalized area indicates that changing the scanning speed makes almost no difference, in other words, the domains have achieved their saturation width already at the fastest scanning speed, so that slowing down the scan rate makes little difference. In contrast,

the bigger growth exponent of bare BTO indicates a faster decrease in domain width with increasing speed, and therefore a slower rate of growth.

In a complementary analysis, we examined the evolution of the growth exponent of domain width in the pABA-functionalized regions depending on the applied voltage (Fig. 3.4b). The maximum domain widths extracted from Fig. 3.3d-f, were found to increase with applied voltage, from approximately 260 nm at 5 V to about 320 nm at 10 V, measured at the slowest scan speeds. As the applied bias approaches the coercive voltage (e.g., at 5 V), the domain width becomes increasingly sensitive to the writing speed. In this regime, the pulse duration becomes the limiting factor, and the difference in domain width between different voltages becomes more pronounced at higher scan speeds. This behavior is reflected in the steeper slope of the power-law dependence, where the extracted growth exponent decreases from –0.04 at 10 V to –0.16 at 5 V, confirming that lower voltages lead to a stronger dependence on the duration of the applied bias.

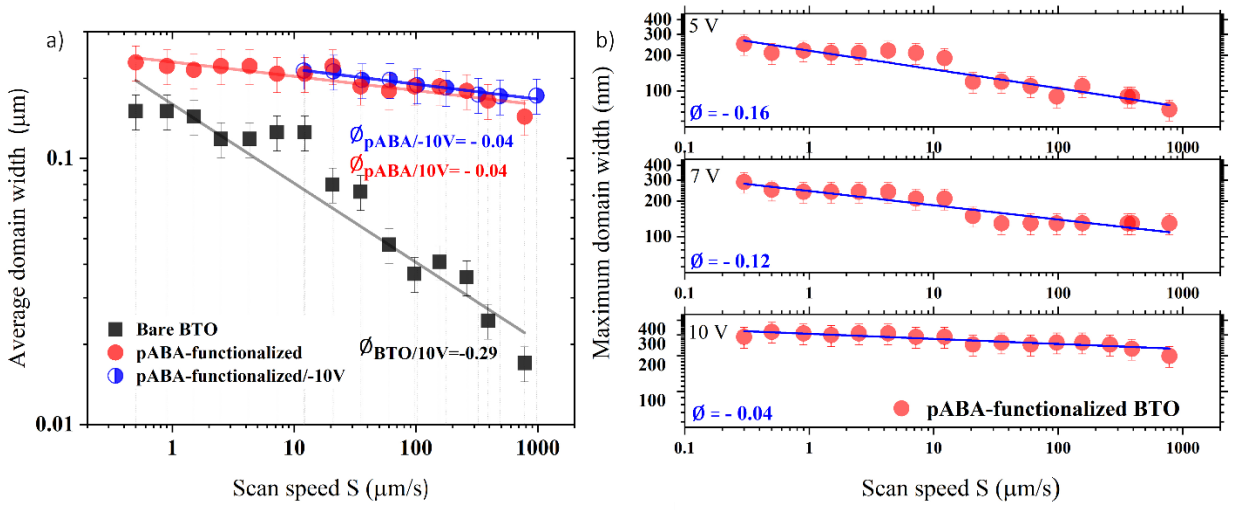


Figure 3.4 *(a) Evolution of switched domain area divided by line length as a function of writing speed at a constant tip bias. Data are shown for bare BTO (black) and pABA-functionalized BTO written with +10 V (red), together with data for the pABA-functionalized surface, pre-poled at +10 V and subsequently written with –10 V (blue). Corresponding PFM images for these bipolar writing experiments are shown in Fig. 3.5.*

(b) Maximum domain width as a function of scan speed for pABA-functionalized BTO films at 5 V, 7 V, and 10 V. The data follow a power-law dependence, where the growth exponent (Ø) decreases from –0.04 at 10 V to –0.16 at 5 V, indicating an increasing sensitivity of domain width to scan speed as the applied voltage approaches the coercive value. All data are fitted (continuous lines) with Eq. (3.1).

We also explored the bipolar screening capability of the pABA-functionalized surface by conducting additional writing speed experiments. In this experiment, the functionalized region was first pre-poled with a +10 V bias to reverse the polarization direction, and domain lines were subsequently written using a –10 V bias at various scan speeds from approximately 12 µm/s up to 1 mm/s. To ensure reproducibility, bipolar switching measurements were performed on 2 separate samples with identical thicknesses. As shown in Fig. 3.5, robust and continuous switching was still achieved, and the calculated domain widths nearly matched those obtained on the sample written with +10 V (Fig. 3.4a). The growth exponent extracted from this data (−0.04) confirms the fast-switching behavior and efficient screening provided by pABA.

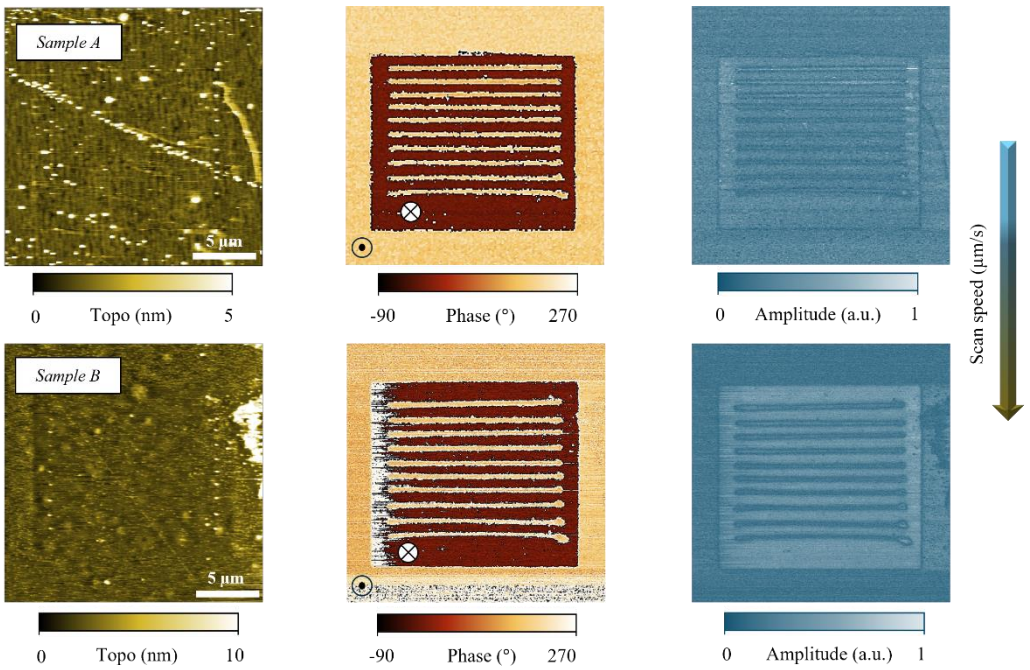


Figure 3.5 *PFM topography, phase and amplitude images (from left to right) demonstrating the bipolar screening capability of the pABA-functionalized BTO surface. The measurements correspond to the opposite-polarity writing experiments, where the surface was pre-poled with +10 V and lines were subsequently written with –10 V (blue data in Fig. 3.4a). Samples A and B correspond to two independent films grown and measured under identical conditions to confirm the reproducibility of the bipolar switching behavior.*

3.5 Concluding remarks

In this Chapter we investigated the initial polarization state and switching dynamics of BTO/SRO/DSO heterostructures, both in their bare form and after functionalization with pABA molecular layers serving as surface screening agents. Our measurements show that the presence of pABA markedly enhances their switching dynamics, facilitating fast switching of ferroelectric domains of either polarity, even at the maximum writing speeds of our scans (close to 1 mm/s). Moreover, bigger and more constant domain widths were obtained as a function of writing speed compared to their bare BTO counterparts. The faster dynamics is attributed to the inherent ability of chemically resonant molecules to adapt their internal charge distribution to electric fields and thus to the ferroelectric depolarizing field. In contrast, bare BTO films are constrained by the unipolar nature of atmospheric adsorbates, which must desorb and resorb with a different polarity to screen the switched polarization. Overall, these findings suggest that “molecular electrodes” (resonant chemical compounds), based on pABA or other suitable organic compounds, may indeed be a useful paradigm in electrodes, merging the superior screening of chemisorption with the fast dynamics required for electronic devices.

References

1 M. Dawber, K.M. Rabe, and J.F. Scott, “Physics of thin-film ferroelectric oxides,” Rev Mod Phys 77(4), 1083–1130 (2005).

2 J.F. Scott, *Ferroelectric Memories* (Springer Berlin Heidelberg, Berlin, Heidelberg, 2000).

3 A.M. Bratkovsky, and A.P. Levanyuk, “Continuous theory of ferroelectric states in ultrathin films with real electrodes,” J Comput Theor Nanosci 6(3), 465–489 (2009).

4 N. Strkalj, G. De Luca, M. Campanini, S. Pal, J. Schaab, C. Gattinoni, N.A. Spaldin, M.D. Rossell, M. Fiebig, and M. Trassin, “Depolarizing-Field Effects in Epitaxial Capacitor Heterostructures,” Phys Rev Lett 123(14), 147601 (2019).

5 B.J. Rodriguez, R.J. Nemanich, A. Kingon, A. Gruverman, S. V. Kalinin, K. Terabe, X.Y. Liu, and K. Kitamura, “Domain growth kinetics in lithium niobate single crystals studied by piezoresponse force microscopy,” Appl Phys Lett 86(1), (2005).

6 R.C. Miller, and G. Weinreich, “Mechanism for the Sidewise Motion of 180° Domain Walls in Barium Titanate,” Physical Review 117(6), 1460–1466 (1960).

7 B.D. Terris, J.E. Stern, D. Rugar, and H.J. Mamin, “Contact electrification using force microscopy,” Phys Rev Lett 63(24), 2669–2672 (1989).

8 A. Agronin, M. Molotskii, Y. Rosenwaks, G. Rosenman, B.J. Rodriguez, A.I. Kingon, and A. Gruverman, “Dynamics of ferroelectric domain growth in the field of atomic force microscope,” J Appl Phys 99(10), (2006).

9 A. Brugère, S. Gidon, and B. Gautier, “Finite element method simulation of the domain growth kinetics in single-crystal LiTaO3: Role of surface conductivity,” J Appl Phys 110(5), 052016 (2011).

10 V.Ya. Shur, A. V. Ievlev, E. V. Nikolaeva, E.I. Shishkin, and M.M. Neradovskiy, “Influence of adsorbed surface layer on domain growth in the field produced by conductive tip of scanning probe microscope in lithium niobate,” J Appl Phys 110(5), (2011).

11 P. Paruch, T. Giamarchi, T. Tybell, and J.M. Triscone, “Nanoscale studies of domain wall motion in epitaxial ferroelectric thin films,” J Appl Phys 100(5), (2006).

12 T. Tybell, P. Paruch, T. Giamarchi, and J.-M. Triscone, “Domain wall creep in epitaxial ferroelectric Pb(Zr 0.2 Ti 0.8)O3 thin films,” Phys Rev Lett 89(9), 097601 (2002).

13 J.Y. Jo, S.M. Yang, T.H. Kim, H.N. Lee, J.-G. Yoon, S. Park, Y. Jo, M.H. Jung, and T.W. Noh, “Nonlinear Dynamics of Domain-Wall Propagation in Epitaxial Ferroelectric Thin Films,” Phys Rev Lett 102(4), 045701 (2009).

14 J.Y. Jo, H.S. Han, J.G. Yoon, T.K. Song, S.H. Kim, and T.W. Noh, “Domain switching kinetics in disordered ferroelectric thin films,” Phys Rev Lett 99(26), (2007).

15 C. Blaser, and P. Paruch, “Subcritical switching dynamics and humidity effects in nanoscale studies of domain growth in ferroelectric thin films,” New J Phys 17(1), 013002 (2015).

16 I. Spasojevic, A. Verdaguer, G. Catalan, and N. Domingo, “Effect of Humidity on the Writing Speed and Domain Wall Dynamics of Ferroelectric Domains,” Adv Electron Mater 8(6), 2100650 (2022).

17 P. Sharma, R.G.P. McQuaid, L.J. McGilly, J.M. Gregg, and A. Gruverman, “Nanoscale Dynamics of Superdomain Boundaries in Single-Crystal BaTiO3 Lamellae,” Advanced Materials 25(9), 1323–1330 (2013).

18 I. Spasojevic, J. Santiso, J.M. Caicedo, G. Catalan, and N. Domingo, “Tunable Molecular Electrodes for Bistable Polarization Screening,” Small 19(30), 2207799 (2023).

19 B. Li, Y. Chen, Z. Liang, D. Gao, and W. Huang, “Interfacial engineering by using self-assembled monolayer in mesoporous perovskite solar cell,” RSC Adv 5(114), 94290–94295 (2015).

20 A.G. Thomas, M.J. Jackman, M. Wagstaffe, H. Radtke, K. Syres, J. Adell, A. Lévy, and N. Martsinovich, “Adsorption Studies of p-Aminobenzoic Acid on the Anatase TiO2 (101) Surface,” Langmuir 30(41), 12306–12314 (2014).

21 C. Dehoff, B.J. Rodriguez, A.I. Kingon, R.J. Nemanich, A. Gruverman, and J.S. Cross, “Atomic force microscopy-based experimental setup for studying domain switching dynamics in ferroelectric capacitors,” Review of Scientific Instruments 76(2), 023708 (2005).

22 B.J. Rodriguez, C. Callahan, S. V Kalinin, and R. Proksch, “Dual-frequency resonance-tracking atomic force microscopy,” Nanotechnology 18(47), 475504 (2007).

23 C. Weymann, C. Lichtensteiger, S. Fernandez-Peña, A.B. Naden, L.R. Dedon, L.W. Martin, J. Triscone, and P. Paruch, “Full Control of Polarization in Ferroelectric Thin Films Using Growth Temperature to Modulate Defects,” Adv Electron Mater 6(12), 2000852 (2020).

24 C. Lichtensteiger, S. Fernandez-Pena, C. Weymann, P. Zubko, and J.-M. Triscone, “Tuning of the Depolarization Field and Nanodomain Structure in Ferroelectric Thin Films,” Nano Lett 14(8), 4205–4211 (2014).

25 J. Junquera, and P. Ghosez, “Critical thickness for ferroelectricity in perovskite ultrathin films,” Nature 422(6931), 506–509 (2003).

26 B. Casals, G.F. Nataf, and E.K.H. Salje, “Avalanche criticality during ferroelectric/ferroelastic switching,” Nat Commun 12(1), 345 (2021)

4 Polarization switching in ultrathin $BaTiO_3$ films stabilized by para-aminobenzoic acid functionalization

In Chapter 3, we discussed how the integration of pABA molecules as an extra screening agent could provide compensating charges during polarization reversal, much faster than atmospheric adsorbates, owing to the molecule's resonant electronic structures. In this Chapter we investigate whether pABA functionalization can also stabilize polarization reversal in BTO films below the critical thickness, where insufficient screening by atmospheric adsorbates can de-stabilize the monodomain polarization configuration seen in thicker films and hinder stable polarization switching. For this reason, in this Chapter we employ the pABA functionalization method described in Chapter 3 for a series of BTO films below the critical thickness and use PFM lithography to write domains on the pABA-functionalized areas. The aim is to determine whether pABA can be used not only to increase switching speed (as proven in Chapter 3) but also to reduce critical thickness for robust switchable ferroelectricity.

4.1 Introduction

As discussed in Chapter 1, reducing ferroelectric film thickness makes stabilization of the polarization against depolarizing fields increasingly challenging. Both theoretical and experimental studies have proposed critical thicknesses below which polarization becomes unstable in perovskite ferroelectrics. For SRO/BTO/SRO/STO, first-principles calculations predict a monodomain critical thickness of ~ 6-unit cell,[1] while experimental reports vary depending on several factors such as epitaxial strain and growth conditions. For example, Zubko et al.,[2] reported a monodomain state with switchable polarization in ultrathin BTO (4.8 nm (~12-unit cell)) films grown on SRO/STO, confirmed through direct observations, employing PFM. De Luca et al.[3] reported monodomain polarization emerging from 4-unit cell of BTO/SRO/STO using in-situ Second Harmonic Generation (SHG) during growth. In another work Strkalj et al.[4] also reported same results for similar structures. However, in both latter cases, switching capability through PFM lithography was only showcased for relatively thicker films of ~30-unit cell thickness, underlining that structural signatures of polarization do not automatically imply polarization switchability and retention at the ultrathin limit.

Domain formation provides an intrinsic mechanism to reduce depolarizing energy, but it comes at a cost: net polarization is suppressed in the polydomain state (that is in fact the point of domain formation) and it compromises retention of written domains, as they tend to relax back toward the polydomain state. Lichtensteiger et al.[5] demonstrated that relaxation of switched states in polydomain films occurs on much shorter timescales than in native monodomain structures. Therefore, several approaches have been proposed to mitigate depolarizing-field–induced domain breakdown. A seminal example is the work of Fong et al.[6] who employed a strategy in which the $PbTiO_3$ (PTO) film surfaces were exposed to a controlled vapor environment during Metal Organic

Chemical Vapor Deposition (MOCVD). Using in situ high-resolution synchrotron X-ray scattering, they reported the absence of satellite peaks in the diffuse X-ray scattering—features that appear when equilibrium 180° stripe domains are present—thereby indirectly indicating a monodomain polar state for films down to 1.2 nm (~3-unit cell). Moreover, in their work they were able to write inverted domains through PFM for their thickest film (9.2 nm(~22-unit cell)). These results highlighted the adequacy of "chemical" rather than "electronic" mechanisms for reducing depolarizing fields.

More recently, Strkalj et al.[7] demonstrated emerging polarization in PTO from the very first unit cell, albeit with a polarization gradient across the thickness; by employing cooperative interface configurations, they stabilized a bulk polarization state down to ~10-unit cell and further reported stable PFM switching for 20-unit cell PTO. In another study, the critical thickness limit in BTO was strongly suppressed by replacing metallic bottom electrodes with an in-plane–polarized ferroelectric buffer that promotes polarization continuity at the interface.[8] Using this approach, successful PFM writing was demonstrated on 10 nm (~24-unit cell) BTO grown on a $Bi_5FeTi_3O_{15}$ buffer.

While these studies highlight the extensive efforts made to avoid domain breakdown, they often emphasize structural detection of polarization (e.g., SHG, XRD, HR-TEM) rather than directly probing the ability to locally switch domains and maintain their stability. In this context, the central question of this Chapter is not whether polarization can exist in a monodomain state instead of polydomain state in ultrathin BTO, but whether stable polarization switching can be achieved and retained. Even a nominally monodomain state does not guarantee switchability, if the reversed polarization state cannot be adequately screened and/or the imprint field is larger than the coercive field. A clear example is provided by the work by Lu et al.[9], who studied 6-unit cell

BTO/ $La_{0.67}Sr_{0.33}MnO_3$ (LSMO)/STO structures. In their work, they reported a monodomain state for bare BTO surface, but the switched polarization state was unstable, showing little retention. However, when an NH_3 interfacial molecular layer was introduced at the graphene/BTO interface, polarization stability was dramatically enhanced, with both upward and downward states retained for several days. This stabilization arises from the ability of NH_3 molecules to realign their dipole moments with the polarization direction of BTO, thereby providing efficient screening of depolarizing fields.

Building on this idea, in our work we sought to explore whether a similar stabilizing effect could be achieved using pABA molecules. In the previous Chapter, we showed that pABA can improve the switching dynamics of relatively thick BTO films. Here, we extend this concept to ultrathin BTO, investigating whether molecular electrodes can facilitate stable polarization switching and retention down to just a few-unit cells. The films studied were grown on DSO substrates by RF-sputtering under the optimized conditions established in Chapter 2.

4.2 Evolution of out-of-plane lattice parameter upon thickness decrease

For the films grown in this Chapter, the deposition parameters were kept identical to those described in Chapter 3, with the BTO layers deposited at an oxygen pressure of 50 mTorr. As shown in Fig. 4.1a, XRD patterns confirm the presence of well-defined (002) BTO reflections, with peak broadening associated to reduced film thicknesses down to approximately 2.5 nm. For the thicker samples, the film thicknesses were determined using X-ray reflectivity (finite thickness oscillations). To further verify the structural quality and accurately assess the thickness of the ultrathin BTO films—particularly where peak broadening complicates XRD analysis, HR-TEM

was performed on the 4.9 nm sample, which will be further discussed in the following sections. The thickness of the thinnest sample (2.5 nm) was extrapolated based on calibrated deposition rates. The out-of-plane lattice parameters were extracted using *interactiveXRDFit*, a software developed by Céline Lichtensteiger[10], consisting in a custom MATLAB-based simulation tool that calculates diffracted intensity profiles for oxide thin films and heterostructures using a built-in library of inorganic materials (Fig. 4.1b).

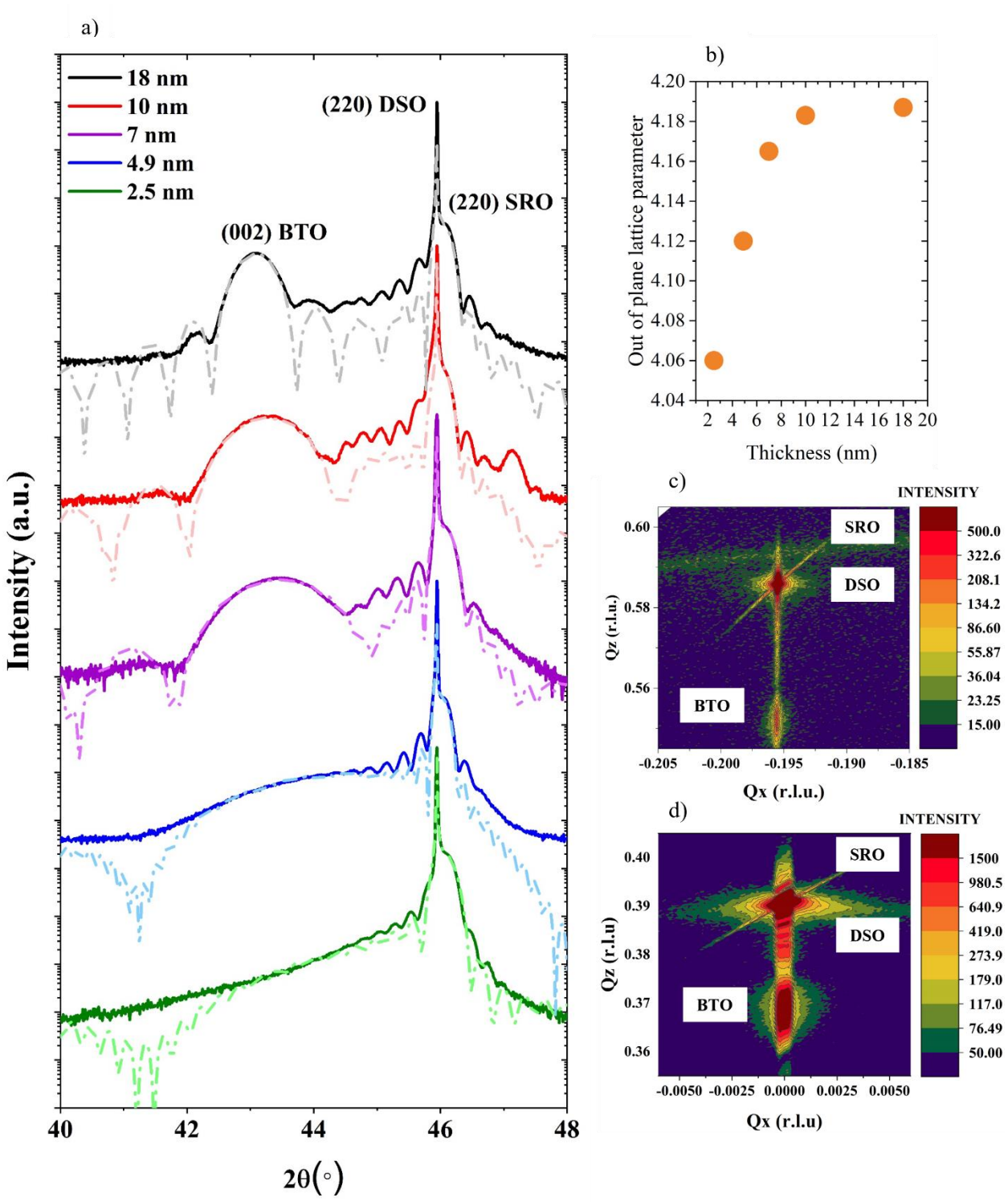


Figure 4.1 *(a) XRD scans of BTO films with different thicknesses grown on SRO/DSO substrates. Well-defined (002) BTO reflections are observed alongside substrate (220) DSO and SRO peaks. Systematic peak shifts and broadening confirm reduced thicknesses down to 2.5nm. Dashed lines are simulations using*

interactiveXRDFit software. (b) Evolution of the out-of-plane lattice parameter as a function of film thickness, showing a gradual reduction with decreasing thickness. RSMs of the 10 nm BTO film recorded around the (33-2) (c) and (220) (d) reflections of the DSO substrate. Both maps show sharp, coherent peaks without diffuse scattering or in-plane satellite features, confirming fully strained epitaxial growth. The absence of periodic satellite peaks indicates that long-range periodic 180° domain structures are not present.

A detailed structural and ferroelectric characterization of the reference 18 nm BTO film—used as a baseline for comparison—was already presented in Chapter 3. This film exhibited an out-of-plane lattice parameter of approximately 4.187 Å. As the thickness is reduced to 10 nm and 7 nm, the lattice parameter decreases slightly to 4.183 Å and 4.165 Å, respectively. However, once the thickness approaches 4.9 and 2.5 nm, the reduction becomes more pronounced, with the out-of-plane parameter reaching approximately 4.12 and 4.06 Å respectively. Since BTO tetragonality is coupled to polarization, the decrease of out-of-plane lattice parameter suggests a reduction of polarization as thickness decreases. Such loss of tetragonality and polarization instability has been reported in literature and attributed to - a dense structure of 180° domains with a high domain wall density.[2,5,11,12] It is nevertheless worth noting that for ultrathin films, the accuracy of lattice parameter extraction becomes increasingly limited due to peak broadening and reduced signal intensity, which may affect the precision of the fitting.

Since the following sections of this Chapter focus on the ferroelectric switching and electromechanical responses of these films, it was essential to ensure that the structural state of the samples was free from concurring effects such as strain gradients or partial relaxation that could affect their functional behavior. To confirm structural integrity and epitaxial quality, reciprocal space mapping (RSM) was performed on the 10 nm BTO film—the thickest sample discussed in this Chapter. Measurements around the (33-2) and (220) reflections (Fig. 4.1c,d) verified fully

coherent epitaxial growth, with no signs of diffuse scattering or in-plane satellite peaks—features typically associated with 180° periodic stripe domains.[13–15] These results thus confirm that the films remain coherently strained and structurally uniform, providing a reliable basis for the subsequent analysis of their ferroelectric behavior.

4.3 Polarization states below the critical thickness

4.3.1 Static domain writing by PFM lithography

To investigate the polarization state and switching capability of our BTO thin films, we performed PFM lithography. Local domains were electrically written by applying ±10 V to the conductive tip (+10 V will induce downward polarization if the as-grown polarization is upward, and –10 V will switch the polarization upward if the as-grown polarization is downward). During all the lithography experiments, the writing conditions—specifically the scan speeds (kept consistent with those used in Chapter 3) and the relative humidity (maintained between 55–60%)—were controlled. As the BTO film thickness was decreased from 18 to 10 nm, we observed a loss of stable polarization switching (Fig.4.2a,b) despite the film still being strongly tetragonal according to the XRD (Fig. 4.1).

As shown in Fig. 4.2b,c, for 10 and 7 nm films, the PFM phase image reveals that regions poled with negative voltage exhibit back-switching (although incomplete), indicating that the films have a preferential average downward polarization in the as-grown state. This contrasts with the behavior observed in the thicker 18 nm reference sample, where the film exhibited a native up-polarized state and allowed stable switching of the domains into either polarity. As the film thickness is reduced even further, this instability becomes more pronounced. In both the 4.9 and

2.5 nm samples, we observed immediate polarization relaxation following voltage application, with no stable retention of the written domains.

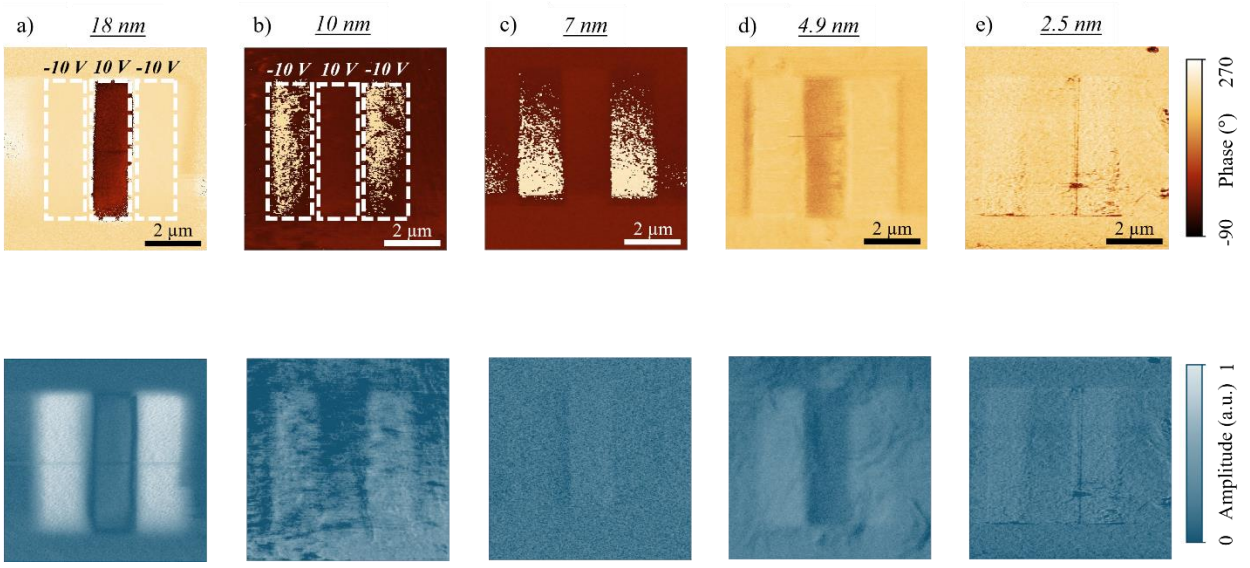


Figure 4.2 *PFM phase (upper panels) and amplitude (bottom panels) images of BTO films with different thicknesses: (a) 18 nm (reference sample), (b) 10 nm, (c) 7 nm, (d) 4.9 nm, and (e) 2.5 nm, showing the evolution of polarization contrast and switching stability as the film approaches the critical thickness. Local domains were written with alternating ±10 V bias, as indicated in panels (a) and (b). The 18 nm film (reference sample) exhibits well-defined and stable domains with clear phase contrast, indicating robust ferroelectric switching. At 10 nm, the written regions display non-uniform contrast and partial back-switching, suggesting incomplete polarization reversal. Similar inhomogeneous switching behavior is observed for the 7 nm film. For the ultrathin 4.9 nm and 2.5 nm films, no stable retention of the written domains is achieved, as immediate relaxation occurs after bias removal.*

Since all the films are epitaxially coherent (i.e. no in-plane strain relaxation), the contrasting PFM behavior between the 18 nm and thinner 10 and 7 nm films must arise from the interplay between thickness, interfacial built-in field and surface boundary conditions. It is well-established that when depolarizing fields grow in magnitude, surface effects —particularly the adsorption and dissociation of atmospheric species—become indispensable for stabilizing the

polarization, providing crucial compensating charge that complements internal screening mechanisms and electronic screening from the bottom electrode.[16–18] Upon exposure to ambient conditions, water molecules dissociate at the surface. Negatively charged OH^- species couple to Ba or Ti cations at the surface favoring upward polarization,[19,20] while H^+ binds to the lattice oxygen atoms at or even below the surface, favoring downward polarizations.[20] In our case, it is possible that as thickness decreases, these two opposing ionic compensation mechanisms may compete, and neither species may supply sufficient screening on its own to sustain a homogeneous polarization. In fact, recent depth-resolved structural characterization using X-ray standing waves on BTO/SRO/DSO heterostructures, suggested an upward polarization orientation in the surface of these films, favored by negatively charged OH^- or O^{2-} adsorbed molecules, with the Ti atom displacement decreasing for the layers below the surface of the film and ultimately reversing the orientation of the polarization in the bulk of the film.[20] This configuration mitigates the depolarizing field, resulting in an average downward polarization with a few unit cells near the surface pointing upward. Similar examples of adsorbates influencing the polarization direction—either driving complete polarization reversals through the entire film or modifying only the topmost unit cells—have been widely reported in thin ferroelectrics.[19–22]

Thus, we argue that, as the thickness decreases from the 18 nm reference, the interplay between depolarizing fields, interfacial screening, and surface chemistry stabilizes a net downward polarization, likely accompanied by upward-biased surface layers due to negatively charged adsorbates. This accounts for the partial and unstable reversal observed in the 10 and 7 nm films under negative bias. The irregular phase contrast and incomplete domain switching indicate rapid back-switching, consistent with limited stabilization of the switched state in ultrathin films.

Subsequently, we examined the thickness distribution of polarization in thinner films using HR-TEM in a cross-sectional lamella prepared by conventional Focused Ion Beam (FIB) milling from the 4.9 nm sample. The High-Angle Annular Dark-Field (HAADF) image (Fig. 4.3a) confirms that interfaces are atomically sharp and that the film growth was coherent. We then analyzed the Ti displacements relative to the Ba sublattice using atomic column position extraction performed with the Atomap Python library (Fig. 4.3b).[1] Since BTO polarization is dominated by Ti–Ba displacement (with a smaller, opposite contribution from O), these displacements provide a reliable estimate of the polarization orientation. The vector map shows small (below 5 pm) and non-uniform displacement vectors, and in some cases even reversed. It should be noted that diffuse contrast in the topmost unit cells, together with the susceptibility of the near-surface layers to FIB-induced damage, may compromise the accuracy of the extracted displacement vectors in the uppermost atomic planes. Such suppression of bulk polarization, combined with the tendency of surface-induced polarization to remain pinned and non-switchable,[20,21] explains why no stable switched domains were detected in PFM. Similar depth-dependent displacement profiles—strong polarization near the surface gradually suppressed toward the electrode—have also been reported for ultrathin PTO films.[7]

[1] FIB sample preparation was conducted by Marcos Rosado Iglesias and Francisco Javier Belarre Triviño; TEM measurements were carried out by Bernat Mundet Bolós and Kapil Gupta; and atomic column analysis was performed by Xinxin Hu.

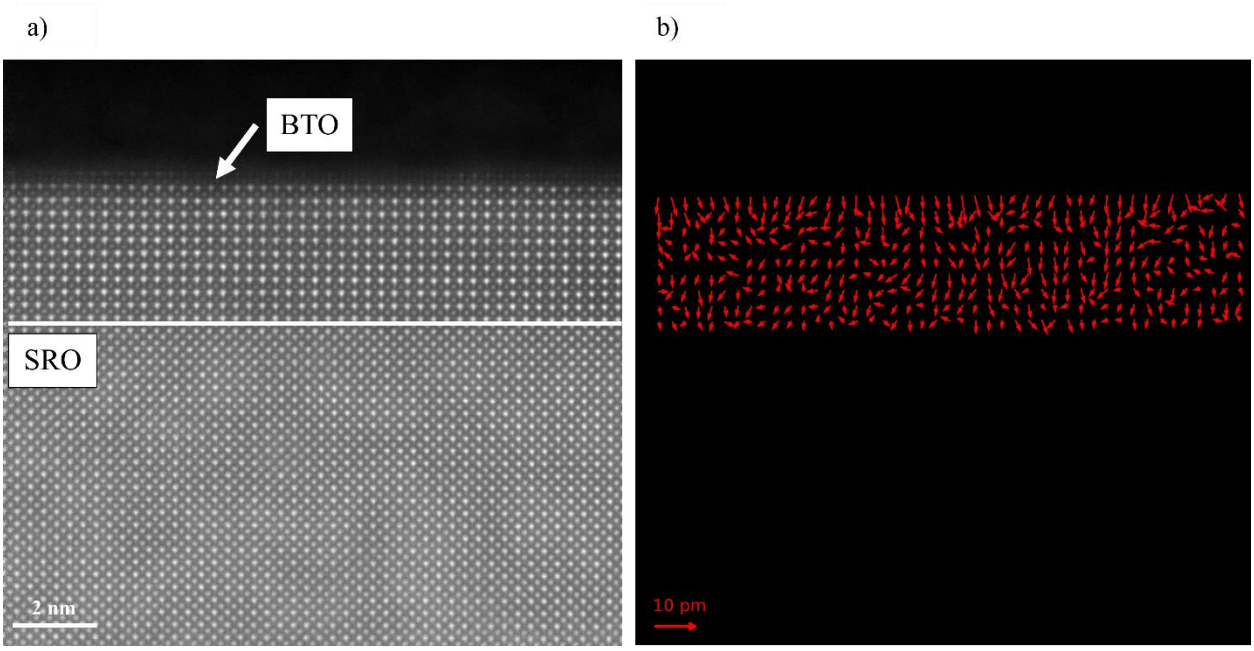


Figure 4.3 *(a) HR-TEM HAADF image of 4.9 nm BTO film on SRO, showing atomically sharp interfaces and coherent epitaxy. (b) The corresponding Ti displacement relative to Ba vector map highlights a non-uniform polarization within the ultrathin film.*

4.3.2 Local switching behavior by SS-PFM

In addition to the domain writing experiments, we conducted SS-PFM measurements using triangular pulsed waveforms and plotted the OFF-state response (i.e., the signal acquired after the tip bias was removed) to probe the switching dynamics across the thickness series. As shown in Fig. 4.4, both the 10 nm and 7 nm films retain switchable ferroelectricity with a ~180° phase contrast between up- and down-polarized states. However, their loops exhibit reduced coercive voltages and a slight negative built-in bias compared to the 18 nm reference sample, which could be consistent with destabilization of the switched domains and rapid back-switching. Meanwhile, the even thinner 4.9 and 2.5 nm films display phase contrasts well below 180°, with the latter barely reaching ~100°. Therefore, while moderately thin films (7–10 nm) still sustain switching

despite some back-switching tendencies observed through lithography, further reduction in thickness leads to a greater suppression of the polarization switching, where written domains relax on a timescale shorter than the measurement window, which is set by the duration of the voltage pulses (≈1 s for the 1 Hz SS-PFM waveform).

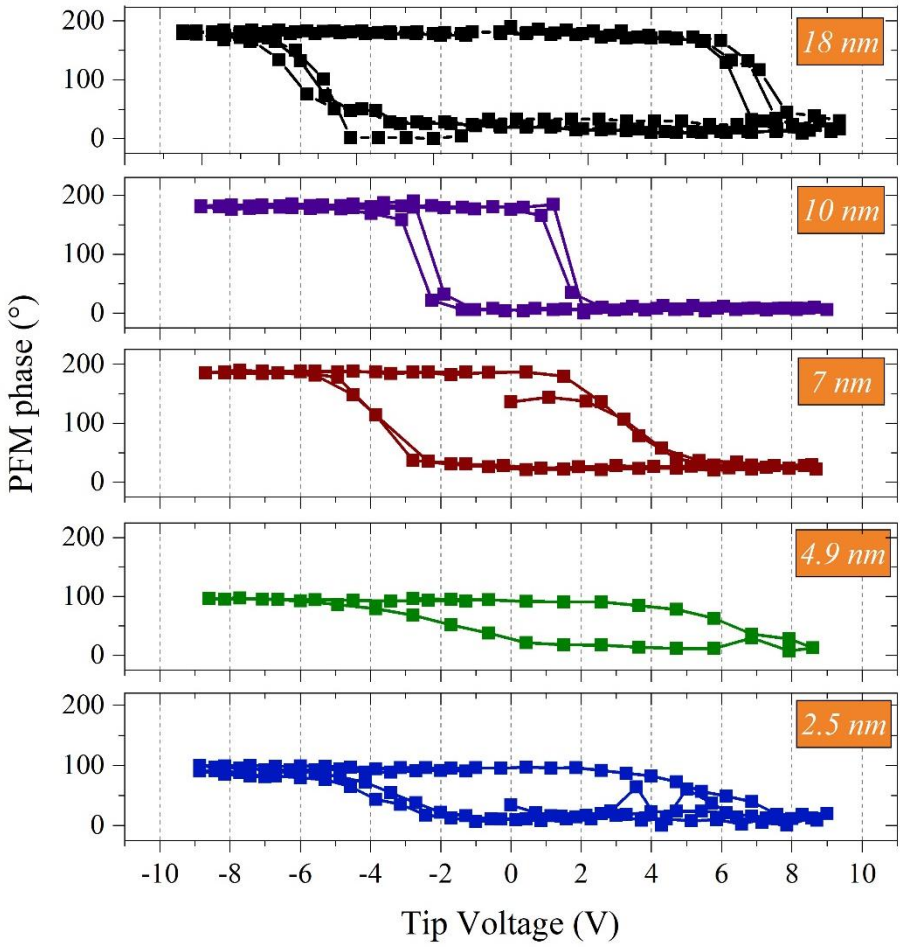


Figure 4.4 *SS-PFM hysteresis loops of BTO films with different thicknesses, showing the evolution of switching behavior with decreasing thickness. The 18 nm reference sample (discussed in Chapter 3) is also shown for comparison. The 10 nm and 7 nm films retain switchable polarization with ~180° phase contrast but display reduced mean coercive voltages and a slight negative built-in bias, consistent with internal fields driving destabilization of written domains. In ultrathin films (4.9 and 2.5 nm), the loops show phase shifts <180° with an imprint larger than the negative "coercive voltage". The results thus suggest that in the two thinnest films, their polarization is not perpendicular to the surface and/or is not robustly switchable.*

4.4 Surface molecular screening and polarization switching stability in ultrathin BTO

4.4.1 Static domain writing by PFM Lithography

After treatment with pABA molecular electrodes, as shown in Fig. 4.5, a clear enhancement in switching stability is observed across all thicknesses. Notably, long-lived domain contrast is observed even for the thinnest BTO sample discussed in this section — a regime where stable polarization switching is notoriously difficult to achieve. In 10 and 7 nm BTO samples, after pABA functionalization, application of -10 V, locally switches domain to up direction. However, unlike in bare films, this time the switched domains remain written without any backswitching. A clear 180° phase contrast is preserved between the written regions and the surrounding area, and the amplitude shows comparable values inside the domains with local minimum at the domain walls. Meanwhile, the even thinner 4.9 and 2.5 nm films also show pronounced stabilization of written domains. The 180° contrast obtained after writing with positive bias in these ultrathin samples subtly suggests that, under the enhanced surface-screening conditions provided by pABA, a residual switchable polarization component—which was previously strongly suppressed and effectively non-switchable due to depolarizing fields—re-emerges with a preferential upward orientation. The results suggest that pABA has important screening properties capable of stabilizing ferroelectricity down to smaller thicknesses than even metals such as SRO (for which the experimental critical thickness for stable monodomain polarization of BTO is above 5 nm).[2]

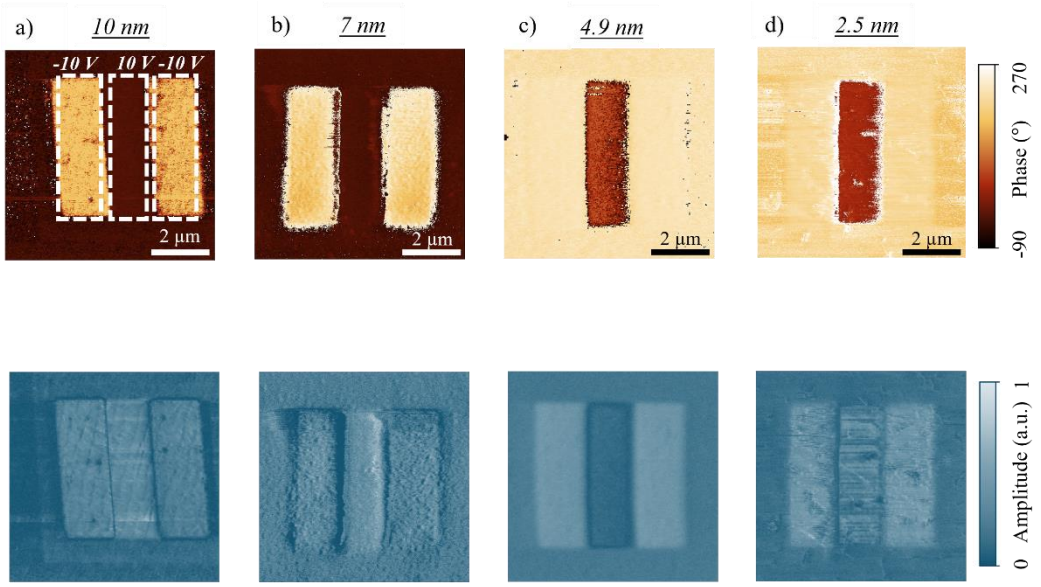


Figure 4.5 *PFM phase (upper panels) and amplitude (bottom panels) images of pABA-functionalized BTO films with different thicknesses: (a) 10 nm, (b) 7 nm, (c) 4.9 nm, and (d) 2.5 nm. Local domains were written with alternating ±10 V bias, as indicated in panel (a). All films exhibit clear and homogenous polarization contrast, demonstrating that molecular functionalization with pABA effectively stabilizes ferroelectric switching down to the ultrathin regime.*

Further evidence of the bipolar screening capability of pABA molecules and the stability of written domains is provided by domain writing experiments performed in a square-in-square configuration (Fig. 4.6). In these tests, the films were first uniformly poled using –10 V (for the 10 nm film) or +10 V (for the 4.9 nm film), followed by writing an inner square region with the opposite voltage. The results, shown for both the 10 nm and 4.9 nm samples, demonstrate robust bipolar switching behavior after surface functionalization with pABA. The written domain patterns remained clearly distinguishable when imaged approximately 48 hours (10 nm film) and 15 hours (4.9 nm film) after the initial poling, indicating long-term retention of the switched polarization states of either sign.

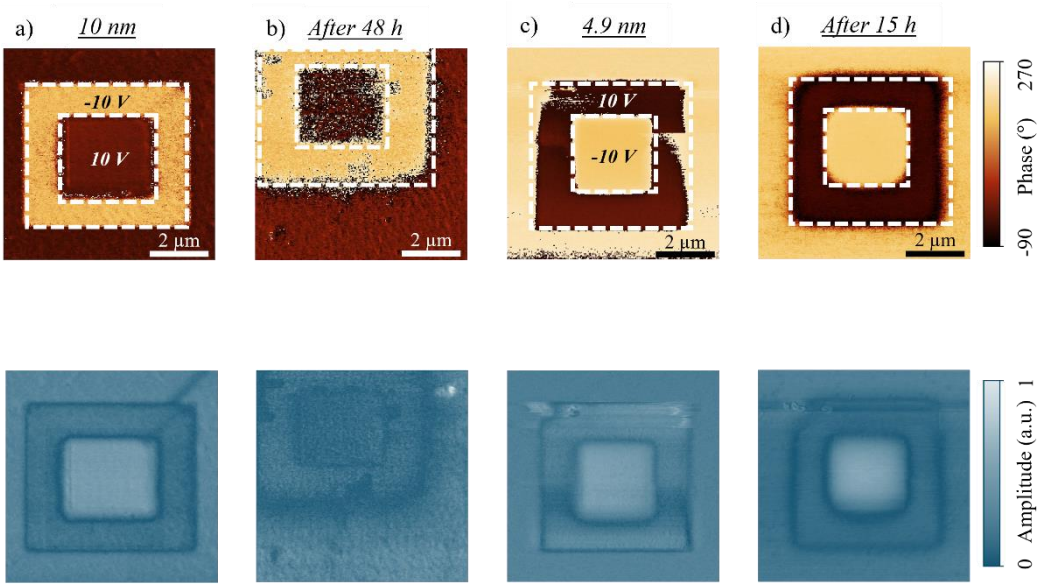


Figure 4.6 *PFM phase (upper panels) and amplitude (bottom panels) images of pABA-functionalized BTO films showing bipolar switching and long-term retention. (a, b) Images correspond to the 10 nm film, which was first pre-poled with –10 V over the entire area, followed by writing a central square with +10 V. Panels (a) and (b) show the initial state and the same region after 48 h, respectively. (c, d) The same sequence is shown for the 4.9 nm film, where the surface was first pre-poled with +10 V and the inner square was written with –10 V, consistent with its opposite average polarization direction. Panels (c) and (d) correspond to the initial and 15 h retention states, respectively.*

4.4.2 Local switching behavior by SS-PFM

The SS-PFM hysteresis loops obtained on pABA-functionalized regions of BTO films are shown in Fig. 4.7. They show improved phase contrast upon switching and general enhancement of coercive voltages compared to bare BTO samples. Although this increase in coercive voltages after pABA functionalization might appear to contrast with the switching-spectroscopy behavior of the thicker 18 nm BTO/DSO reference film discussed in Chapter 3, the origin of this difference can be rationalized by considering how the electromechanical response evolves with thickness, hence depolarizing fields. In general, the electromechanical response captured in a hysteresis loop

reflects a combination of the A) voltage required to switch the polarization and B) the stability of the switched state against depolarizing fields. In a thicker film such as the 18 nm sample, where stabilization of the switched domains is not a limiting factor, narrower loops and lower coercive voltages can simply indicate faster domain-wall motion and the formation of bigger written domains (as observed in Chapter 3 after pABA functionalization). However, when depolarizing fields grow in magnitude, the stability of the switched state becomes the limiting factor in the overall loop response, and narrow loops together with fast domain-wall motion can also translate into more rapid back-switching of the written domains. In contrast, wider loops and increased coercive voltages after pABA functionalization indicate that the switched polarization is better stabilized against depolarizing-field–driven relaxation.

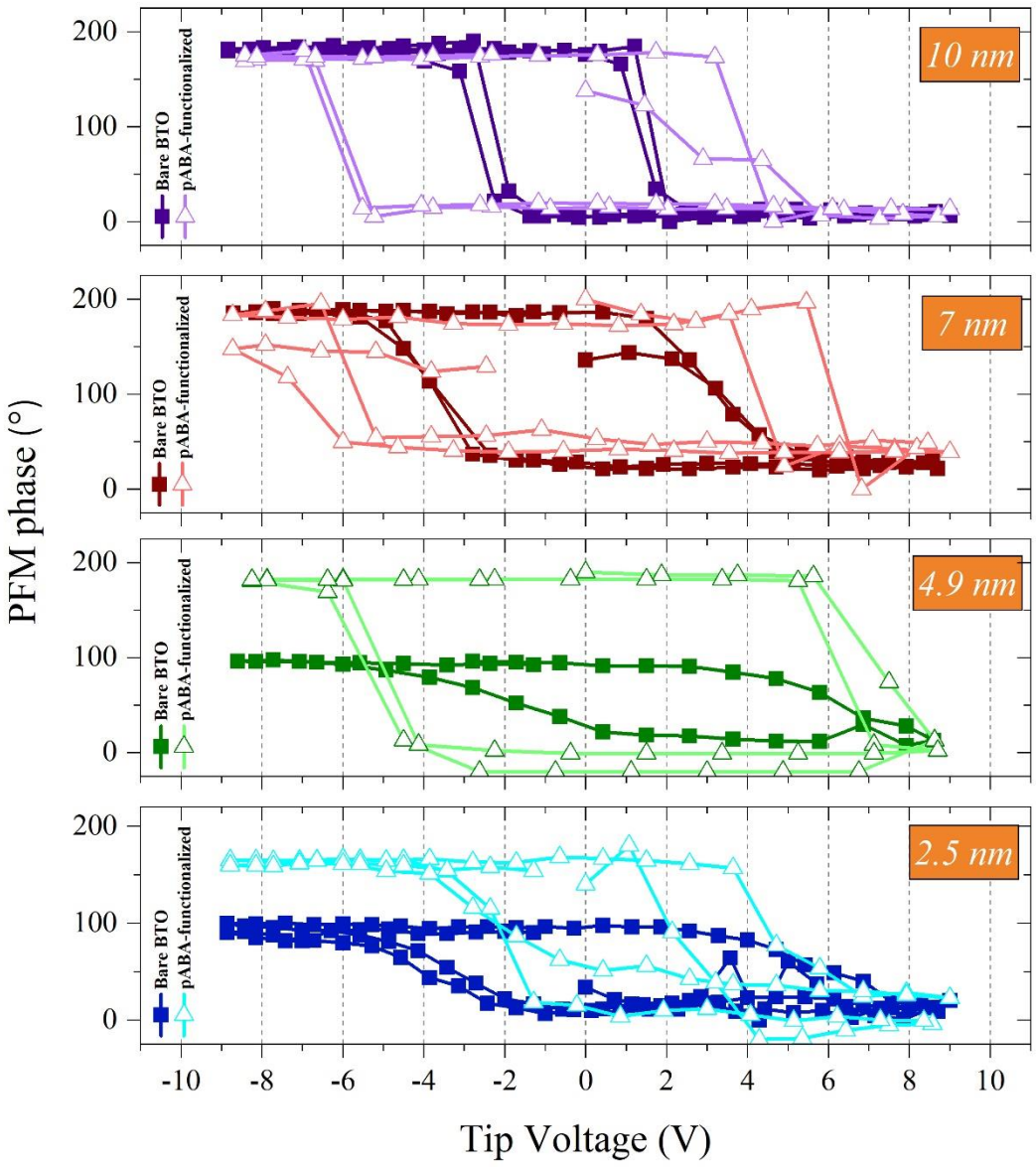


Figure 4.7 *SS-PFM phase–voltage hysteresis loops obtained for bare (solid squares) and pABA-functionalized (open triangles) BTO films with thicknesses of 10 nm (purple), 7 nm (red), 4.9 nm (green), and 2.5 nm (blue). The films exhibit enhanced coercive voltages and improved phase contrast (stability of switched states) compared to bare films.*

In order to directly compare the screening efficiency of molecular electrodes with that of a conventional metallic electrode, we additionally grew SRO top electrodes on 10 nm

BTO/SRO/DSO heterostructures. The SRO layer with approximate thickness of 30 nm was deposited in situ and subsequently patterned (20-50 μm diameter) via photolithography, followed by selective etching using $NaIO_4$ to produce well-defined electrode geometries. SS-PFM measurements were then performed on both the electrode regions and the adjacent bare BTO surface using the AFM tip as the top contact. The bare BTO areas (Fig. 4.8a) exhibited ferroelectric switching in both the "ON" state—where the applied bias probes domain dynamics under field—and the "OFF" state—where domain stability is assessed at zero field after application of DC poling pulses. The corresponding OFF-state hysteresis loops displayed the hallmark ferroelectric signatures: butterfly-shaped amplitude curves and 180° phase reversals at the amplitude minima. As the 10 nm and 7 nm bare BTO films discussed in section 4.3.2, the loops were shifted slightly toward negative voltages, consistent with an average downward polarization. Minor variations in coercive voltages compared to earlier results are likely attributable to processing effects introduced during the photolithography and etching steps. In contrast, the SRO-covered regions showed a markedly different response. While the ON-state loops displayed a narrow hysteresis—indicating some polarization switching under bias—the OFF-state measurements revealed no discernible phase or amplitude contrast between oppositely poled areas (Fig. 4.8b). This lack of remanent contrast suggests that the switched polarization rapidly relaxes once the field is removed.

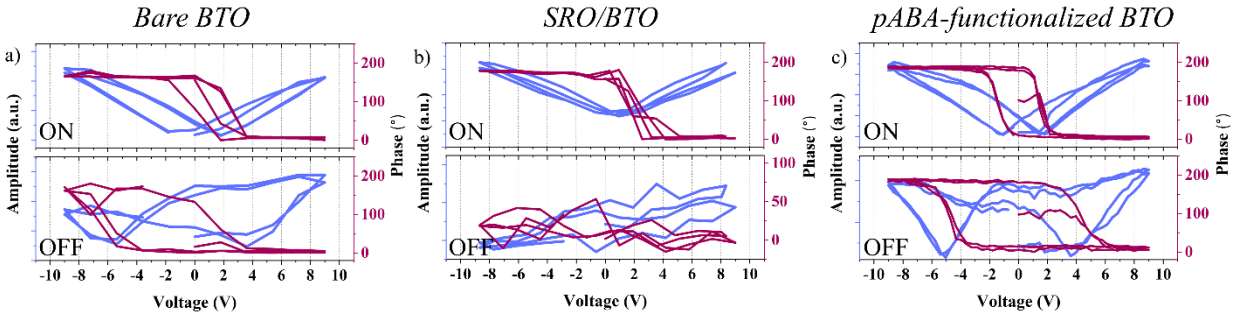


Figure 4.8 *SS-PFM hysteresis loops of 10 nm BTO/SRO/DSO: (a) ON- and OFF-state phase and amplitude loops of bare BTO regions, showing ferroelectric switching. (b) Corresponding ON- and OFF-state loops of SRO-covered regions, where remanent switching is suppressed. Both ON and OFF signals, as well as amplitude responses, are shown here to provide a clearer link with the discussion in the text. (c) ON- and OFF-state phase and amplitude loops for pABA-functionalized (10 nm) BTO film shown for comparison.*

The SS-PFM results of pABA-functionalized (10 nm) BTO, is also shown here for comparison, where both ON and OFF signals, show butterfly-shaped amplitude curves and 180° phase signals as previously discussed in section 4.4.2. These results lead to a clear conclusion: For 10 nm BTO films, atmospheric adsorbates alone are insufficient to stabilize long-lived switched domains, although the films still display switchable ferroelectric behavior when probed locally by SS-PFM in the bare state. The choice of screening mechanism therefore becomes critical. Functionalization with pABA molecular layers provides efficient interfacial screening, enhancing the ferroelectric response and enabling stable polarization retention. In contrast, integration of a metallic SRO top electrode not only fails to improve screening but actively suppresses the remanent polarization, as evidenced by SS-PFM loops.

4.4.3 Control experiments on pABA/SRO: verifying ferroelectric origin of PFM contrast

Accurate determination of local ferroelectric properties requires a careful interpretation of the PFM signal, which is influenced by multiple overlapping electromechanical and electrostatic contributions. Notably, changes in the tip-sample junction potential, caused by charge injection or relaxation phenomenon, also result in hysteresis-like behavior, with phase shifts and amplitude changes that mimic true ferroelectric switching.[23] These effects can easily be misinterpreted if not properly controlled. Thus, distinguishing between genuine ferroelectric responses and artifacts

originating from charge dynamics or electrostatic forces is essential. In our study, this concern applies particularly to the pABA molecular layer interfaced with BTO. To rule out the possibility that pABA acts merely as a passive dielectric or an electret —contributing spurious contrast via charge trapping or molecule–tip interactions—we start by referring to earlier findings from our group,[24] where the observed independence of coercive voltage as a function of pABA thickness indicated that the organic layer was unlikely to be the origin of the hysteresis. Moreover, our own results provide further evidence of genuine ferroelectric switching. Domain patterns written on pABA-functionalized BTO films remained stable and clearly visible, even 48 hours after writing, as discussed in the previous section. This long retention time strongly argues against transient effects such as charge injection, which typically relax within seconds or minutes.[25]

To further substantiate this claim, a control experiment was performed on samples consisting of SRO electrodes directly coated with pABA, but without the BTO layer. The same voltage-writing protocol applied to these samples produced no observable phase or amplitude contrast in PFM (Fig. 4.9). This outcome confirms that pABA alone does not generate artificial signals under the applied electric field, i.e. there is no ferroelectric-like contrast. The switching contrast observed in our functionalized BTO films therefore originates from stabilized ferroelectric polarization, not from tip–molecule artifacts or extrinsic charging effects.

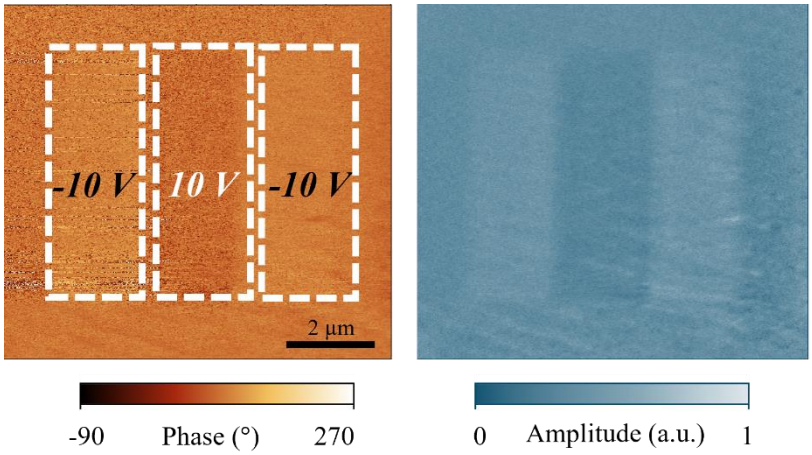


Figure 4.9 *Control experiment on pABA-coated SRO/DSO without a BTO layer. PFM phase (left) and amplitude (right) images after applying ±10 V writing bias to the marked regions. No measurable contrast is observed in either channel, confirming that pABA alone does not generate artificial switching signals.*

4.5 Concluding remarks

In summary, our results demonstrate that polarization stability in ultrathin BTO/SRO/DSO films is critically governed by the balance between depolarizing fields and charge screening. Below the critical thickness, bare films exhibited rapid relaxation of written domains, manifested either as incomplete phase contrast or domain shrinkage. Molecular functionalization with pABA provided efficient, dynamic screening of polarization charges, enabling the retention of stable domains over extended timescales and even under bipolar switching conditions at a lower critical thickness than bare films. These findings highlight the potential of molecular layers as a versatile and effective route to control polarization states in ferroelectric tunnel junctions, which will be discussed in the next Chapter.

References

1 J. Junquera, and P. Ghosez, “Critical thickness for ferroelectricity in perovskite ultrathin films,” Nature 422(6931), 506–509 (2003).

2 P. Zubko, H. Lu, C.-W. Bark, X. Martí, J. Santiso, C.-B. Eom, G. Catalan, and A. Gruverman, “On the persistence of polar domains in ultrathin ferroelectric capacitors,” Journal of Physics: Condensed Matter 29(28), 284001 (2017).

3 G. De Luca, N. Strkalj, S. Manz, C. Bouillet, M. Fiebig, and M. Trassin, “Nanoscale design of polarization in ultrathin ferroelectric heterostructures,” Nat Commun 8(1), 1419 (2017).

4 N. Strkalj, G. De Luca, M. Campanini, S. Pal, J. Schaab, C. Gattinoni, N.A. Spaldin, M.D. Rossell, M. Fiebig, and M. Trassin, “Depolarizing-Field Effects in Epitaxial Capacitor Heterostructures,” Phys Rev Lett 123(14), 147601 (2019).

5 C. Lichtensteiger, S. Fernandez-Pena, C. Weymann, P. Zubko, and J.-M. Triscone, “Tuning of the Depolarization Field and Nanodomain Structure in Ferroelectric Thin Films,” Nano Lett 14(8), 4205–4211 (2014).

6 D.D. Fong, A.M. Kolpak, J.A. Eastman, S.K. Streiffer, P.H. Fuoss, G.B. Stephenson, C. Thompson, D.M. Kim, K.J. Choi, C.B. Eom, I. Grinberg, and A.M. Rappe, “Stabilization of Monodomain Polarization in Ultrathin PbTiO3 Films,” Phys Rev Lett 96(12), 127601 (2006).

7 N. Strkalj, C. Gattinoni, A. Vogel, M. Campanini, R. Haerdi, A. Rossi, M.D. Rossell, N.A. Spaldin, M. Fiebig, and M. Trassin, “In-situ monitoring of interface proximity effects in ultrathin ferroelectrics,” Nat Commun 11(1), 5815 (2020).

8 E. Gradauskaite, Q.N. Meier, N. Gray, M.F. Sarott, T. Scharsach, M. Campanini, T. Moran, A. Vogel, K. Del Cid-Ledezma, B.D. Huey, M.D. Rossell, M. Fiebig, and M. Trassin, “Defeating depolarizing fields with artificial flux closure in ultrathin ferroelectrics,” Nat Mater 22(12), 1492–1498 (2023).

9 H. Lu, A. Lipatov, S. Ryu, D.J. Kim, H. Lee, M.Y. Zhuravlev, C.B. Eom, E.Y. Tsymbal, A. Sinitskii, and A. Gruverman, “Ferroelectric tunnel junctions with graphene electrodes,” Nat Commun 5(1), 5518 (2014).

10 C. Lichtensteiger, “InteractiveXRDfit: A new tool to simulate and fit X-ray diffractograms of oxide thin films and heterostructures,” J Appl Crystallogr 51(6), 1745–1751 (2018).

11 C. Weymann, C. Lichtensteiger, S. Fernandez-Peña, A.B. Naden, L.R. Dedon, L.W. Martin, J. Triscone, and P. Paruch, “Full Control of Polarization in Ferroelectric Thin Films Using Growth Temperature to Modulate Defects,” Adv Electron Mater 6(12), (2020).

12 W. Peng, J. Mun, Q. Xie, J. Chen, L. Wang, M. Kim, and T.W. Noh, “Oxygen vacancy-induced topological nanodomains in ultrathin ferroelectric films,” NPJ Quantum Mater 6(1), 48 (2021).

13 S.K. Streiffer, J.A. Eastman, D.D. Fong, C. Thompson, A. Munkholm, M. V. Ramana Murty, O. Auciello, G.R. Bai, and G.B. Stephenson, “Observation of Nanoscale 180° Stripe Domains in Ferroelectric PbTiO3 Thin Films,” Phys Rev Lett 89(6), 067601 (2002).

14 M. Gharbi, C. Davoisne, F. Le Marrec, L. Dupont, and N. Lemée, “Disentangling elastic relaxation and ferroelectric domain contributions to in plane X-ray scattering profile: A necessity in strained ferroelectric superlattices,” Mater Lett 275, 128138 (2020).

15 G. Catalan, A. Janssens, G. Rispens, S. Csiszar, O. Seeck, G. Rijnders, D.H.A. Blank, and B. Noheda, “Polar Domains in Lead Titanate Films under Tensile Strain,” Phys Rev Lett 96(12), 127602 (2006).

16 S. V. Kalinin, C.Y. Johnson, and D.A. Bonnell, “Domain polarity and temperature induced potential inversion on the BaTiO 3(100) surface,” J Appl Phys 91(6), 3816–3823 (2002).

17 T. Tybell, C.H. Ahn, and J.M. Triscone, “Ferroelectricity in thin perovskite films,” Appl Phys Lett 75(6), 856–858 (1999).

18 F. Peter, K. Szot, R. Waser, B. Reichenberg, S. Tiedke, and J. Szade, “Piezoresponse in the light of surface adsorbates: Relevance of defined surface conditions for perovskite materials,” Appl Phys Lett 85(14), 2896–2898 (2004).

19 C. Gattinoni, N. Strkalj, M. Fiebig, M. Trassin, and N.A. Spaldin, “Interface and surface stabilization of the polarization in ferroelectric thin films,” PNAS 117(46), 28589–28595 (2007).

20 L.P. Hoang, I. Spasojevic, T.-L. Lee, D. Pesquera, K. Rossnagel, J. Zegenhagen, G. Catalan, I.A. Vartanyants, A. Scherz, and G. Mercurio, “Surface polarization profile of ferroelectric thin films probed by X-ray standing waves and photoelectron spectroscopy,” Sci Rep 14(1), 24250 (2024).

21 H. Lee, T.H. Kim, J.J. Patzner, H. Lu, J.W. Lee, H. Zhou, W. Chang, M.K. Mahanthappa, E.Y. Tsymbal, A. Gruverman, and C.B. Eom, “Imprint Control of BaTiO3 Thin Films via Chemically Induced Surface Polarization Pinning,” Nano Lett 16(4), 2400–2406 (2016).

22 J. Shin, V.B. Nascimento, G. Geneste, J. Rundgren, E.W. Plummer, B. Dkhil, S. V. Kalinin, and A.P. Baddorf, “Atomistic screening mechanism of ferroelectric surfaces: An in situ study of the polar phase in ultrathin BaTiO3 films exposed to H 2O,” Nano Lett 9(11), 3720–3725 (2009).

23 N. Balke, P. Maksymovych, S. Jesse, I.I. Kravchenko, Q. Li, and S. V. Kalinin, “Exploring local electrostatic effects with scanning probe microscopy: Implications for piezoresponse force microscopy and triboelectricity,” ACS Nano 8(10), 10229–10236 (2014).

24 I. Spasojevic, J. Santiso, J.M. Caicedo, G. Catalan, and N. Domingo, “Tunable Molecular Electrodes for Bistable Polarization Screening,” Small 19(30), (2023).

25 N. Balke, P. Maksymovych, S. Jesse, A. Herklotz, A. Tselev, C.-B. Eom, I.I. Kravchenko, P. Yu, and S. V. Kalinin, “Differentiating Ferroelectric and Nonferroelectric Electromechanical Effects with Scanning Probe Microscopy,” ACS Nano 9(6), 6484–6492 (2015).

5 Tunneling electroresistance in ultrathin films

Having established that pABA functionalization can stabilize monodomain polarization in ultrathin ferroelectric films, we now investigate a possible application for them: Ferroelectric Tunnel Junctions (FTJ). In FTJs, non-destructive readout is achieved by exploiting quantum tunneling through a nanometer-scale ferroelectric barrier, where the electron transmission probability depends on the polarization orientation. Their correct functioning therefore requires ferroelectric films that are sufficiently thin to enable tunneling yet have switchable and stable polarization (to enable contrast between up-polarized and down-polarized states). These two requisites have been hard to meet simultaneously due to depolarization effects, but the performance of pABA electrodes demonstrated in this thesis suggests that they could offer a way forward. In this Chapter we show that stable polarization switching in ultrathin films (below 4-unit cell) produces two distinct resistive states (ON, Low Resistive State (LRS) and OFF, High Resistive State (HRS)) arising from polarization controlled modulation of the tunneling barrier. We show the Tunneling Electroresistance (TER) effect both through local measurements using Conductive Atomic Force Microscopy (CAFM), and through macroscopic current-voltage measurements.

5.1 Introduction

As outlined in Chapter 1, polarization switching alters the electrostatic potential profile across the barrier in an FTJ, modulating the tunneling transmission probability. Realizing this effect, however, requires maintaining a stable polarization in ferroelectric layers that are thin enough for quantum tunneling to dominate transport. However, as thickness decreases, ferroelectricity is destabilized by depolarizing fields, imperfect screening, and interface-related effects. Below a critical thickness, the spontaneous polarization becomes unstable or unswitchable. As discussed in Chapter 4, polarization gradients and domain fragmentation emerge in this regime, and while an external field may transiently align dipoles, insufficient screening causes rapid relaxation into a state with zero average polarization once the field is removed, hindering stable switching and limiting FTJ functionality.

These intrinsic limitations pose a major challenge, and extensive experimental efforts have focused on identifying interface and strain conditions that can preserve monodomain ferroelectricity at reduced dimensions to produce a sizable TER effect.[1,2] The TER ratio is typically defined as the relative change in resistance (or conductance) between the high- and low-resistance states, expressed as TER = $(R_{OFF} - R_{ON})/R_{ON}$ and serves as a quantitative measure of the polarization-controlled modulation of the tunneling current.

A representative strategy to stabilize ferroelectricity at reduced thicknesses was demonstrated by Garcia et al., who employed $NaGaO_3$ (NGO) substrates to impose strong compressive strain, stabilizing out-of-plane ferroelectricity in BTO layers down to 1 nm.[3] NGO imposes ~3.2% compressive lattice mismatch on BTO—roughly double that of DSO (~1.6%)—and such enhanced compressive strain is known to increase tetragonality and Curie temperature, thereby helping to sustain out-of-plane polarization in the ultrathin limit. This enabled reliable

switching and resistive contrast under tunneling conditions, with TER values of ~2 at 1 nm thickness, which were significantly enhanced to ~750 when the thickness was increased to 3 nm. However, their thinnest films exhibited weak PFM and CAFM domain contrast, suggesting there was only marginal polarization stability at 1 nm. Moreover, there was no verification that the transport remained tunneling-dominated across the full thickness range.

Meanwhile, Gruverman et al. demonstrated switchable tunneling resistance in BTO films as thin as 2.4 nm (6 unit cells) grown on STO (compressive strain of 2.38 %), reporting a TER of ~7, which increased to ~80 for 4.8 nm films, with current densities in order of 10^6 A/cm^2.[4] Since 2.4 nm was their experimental lower bound, it remains open how a further thickness reduction would impact polarization retention. In another study, Guo et al. investigated BTO films grown on Si substrates with an STO buffer layer and found that, although layers down to 1.5 nm could be fabricated, their TER nearly vanished, likely due to the loss or instability of switchable polarization at such low thicknesses. They identified an optimal TER of ~158 for 2 nm films, followed by a decrease at larger thicknesses, which they attributed to the involvement of transport mechanisms other than tunneling.[5] Moreover, Wen et al. studied BTO films on DSO and reported TER values of ~10 at 12-unit cell (approximately 4.9 nm) thickness. However, temperature-dependent measurements revealed that the TER observed at room temperature primarily originated from phonon-assisted indirect tunneling, rather than from a polarization-modulated barrier.[6] These results again highlight that approaching the ultrathin limit often compromises ferroelectric retention and that, above the optimal thickness for FTJ functionality, non-tunneling channels can dominate.

In these latter cases, the electromechanical response of the ferroelectric films was also probed by PFM, confirming stable polarization switching. Several other reports have shown TER

effects in even thinner BTO films, indirectly implying that the films remain switchable; however, direct investigations of domain writing and retention using PFM remain relatively scarce. A case in point is the work of Li et al. [7], who explored FTJs incorporating ultrathin BTO layers and observed distinct resistance states even in a 2-unit cell film (approximately 0.8 nm), with a TER ratio of ~4, but PFM switching at this minimum thickness was not demonstrated, so the retention of the written state under zero bias remains unclear.

Taken together, the state of the art shows that (i) polarization stability at the few-unit cell limit is often marginal or undocumented, (ii) large TER, generally observed at larger thickness (2-10 nm range) can partly stem from non-tunneling channels or indirect processes, and (iii) robust, direct PFM verification of ultrathin retention is rarely paired with transport data. Motivated by these gaps, we examine whether our pABA functionalization strategy can stabilize ferroelectricity in few-unit cell BTO while preserving a tunneling-dominated regime. We explicitly combine PFM (for domain writing/retention) with I–V/CAFM (for transport) to assess TER mechanisms and compare performance against prior BTO-based FTJs. We demonstrate that 2-unit cell BTO films grown on DSO, when integrated with molecular top electrodes, exhibit bi-stable polarization switching as confirmed by PFM, and show clear and reproducible resistive switching with well-separated ON and OFF states both at nanoscopic level confirmed by CAFM and also at device level using top graphite electrodes and tested via macroscopic I-V curves.

5.2 Structural and ferroelectric characterization of 2-unit cell BTO films

BTO films of 2-unit cell thickness, grown under the optimized conditions described in Chapter 2 and with a growth pressure adjusted to 25 mTorr, were selected as the basis for most of

the experiments in this Chapter. Given their extremely small thickness, the BTO film reflection in XRD scans is barely detectable and extremely broad (inset Fig. 5.1a) . Hence, we turn to HR-TEM to examine the thickness and structural quality. The images reveal atomically sharp interfaces and uniform contrast, confirming coherent epitaxial growth even at the ultrathin limit (Fig. 5.1a). To further verify the film composition and thickness, cross-sectional Electron Energy-Loss Spectroscopy (EELS) elemental mapping was performed. Clear contrast in the Sr, Ru, Ti, and Ba maps confirms the presence of precisely 2 BTO unit cells sandwiched between the SRO electrode and the surface (Fig. 5.1a, bottom panels).

The ferroelectric properties were then probed by PFM lithography. On bare 2-unit cell BTO films, written domains showed no phase contrast (Fig. 5.1b, top), consistent with lack of ferroelectricity or poor retention below the critical thickness. By contrast, pABA-functionalized films exhibited stable phase contrast with defined domain boundaries (Fig. 5.1b, bottom). This indicates that the molecular layer provides efficient surface screening and stabilizes polarization switching at the atomic-scale limit. SS-PFM was also performed on both bare and functionalized areas. Although bare BTO did not show any hysteretic behavior upon application of voltage, pABA-functionalized areas, showed a robust hysteresis loop, observed through both phase and amplitude signals (Fig. 5.1c).

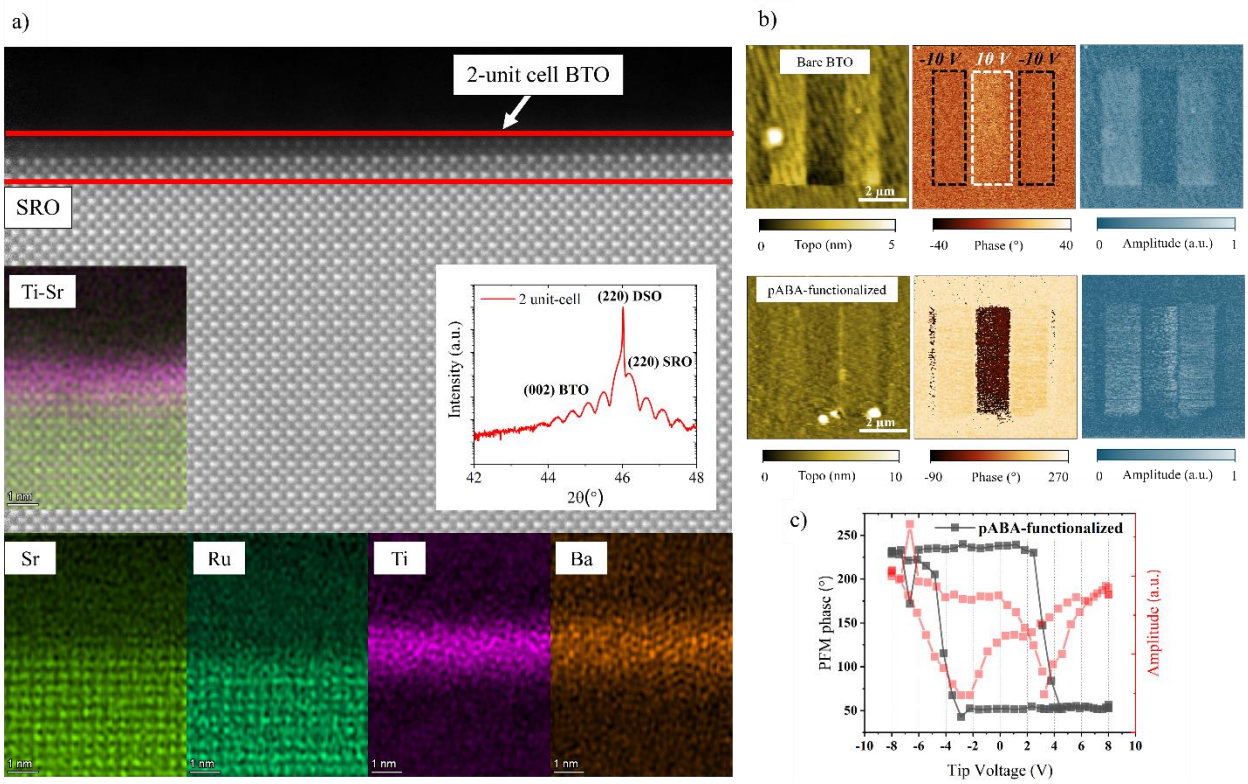


Figure 5.1 *(a) HR-TEM image of a 2-unit cell BTO/SRO/DSO heterostructure with elemental EELS maps confirming the presence of Ba, Ti, Sr, and Ru across the interface (inset: XRD scan showing the weak (002) BTO reflection alongside SRO and DSO peaks). (b) PFM topography, phase and amplitude images (from left to right) comparing bare and pABA-functionalized 2-unit cell BTO films, demonstrating stabilization of polarization switching by molecular functionalization. (c) SS-PFM hysteresis loop of pABA-functionalized area.*

The consistency of the domain lithography results was verified by repeating the measurements at multiple locations across the sample. To further assess the retention of the written domains, consecutive PFM read scans were performed immediately after writing, followed by additional scans after several hours. The written regions consistently exhibited clear phase contrast at the domains and amplitude contrast at the domain boundaries, confirming the robust retention and stability of the polarization state in the pABA-functionalized films (Fig. 5.2) over a time scale of hours. Subsequently, nominally 1- and 4-unit cell BTO films were also prepared by halving and

doubling the growth time of the 2-unit cell reference, respectively. These were included in later experiments to further probe thickness dependence at the atomic limit.

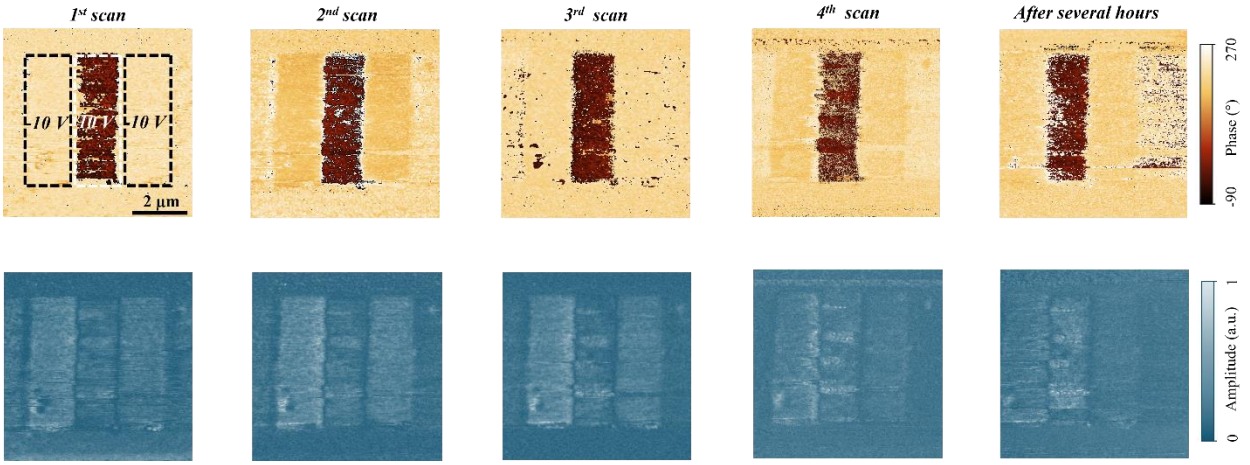


Figure 5.2 *Sequential PFM phase (upper panels) and amplitude (bottom panels) images of pABA-functionalized 2-unit cell BTO film showing the temporal stability of the written domains. The images correspond to the first to fourth consecutive read scans after writing, followed by an additional scan performed several hours later.*

5.3 Polarization-dependent tunneling and TER characterization by CAFM

To study the TER effect, we monitored polarization switching via PFM, and examined its correlation with local conductivity, measured by CAFM. In CAFM, a conductive AFM tip is brought into contact with the sample surface while a voltage bias is applied between the tip and the bottom electrode, allowing to capture the current response of different domain configurations.[3,4,8–11] The tip simultaneously acts as a movable top electrode and a local probe for tunneling or leakage currents. A low-noise current amplifier integrated into the AFM system records the current flowing through the tip–sample junction during either surface scans or stationary point measurements. In mapping mode, the tip scans the surface under a fixed bias, producing spatially resolved current maps that directly correlate local conductivity with

ferroelectric domain patterns. In point-spectroscopy mode, the tip is positioned at a selected site, and the bias is swept to record local I–V characteristics, enabling direct comparison of transport properties for different polarization states. To extend the accessible current range while maintaining sensitivity at low signals, a dual-gain ORCA current-sensing holder (Asylum Research) was used, allowing reliable measurements from the picoampere to microampere scale.

To investigate the polarization-dependent tunneling behavior in the pABA-functionalized 2-unit cell BTO films, ferroelectric domains were first written using the PFM setup by applying local bias voltages through the conductive AFM tip, following the same writing pattern as shown in Fig. 5.2. After domain writing, we moved to the CAFM configuration, where current mapping was performed over the same pre-poled regions of a representative sample to assess the local current response. As shown in Fig. 5.3a the CAFM current maps, recorded with read voltage of 1.5 V applied to the sample, reveal a distinct contrast between polarized areas with +10 V and –10 V, corresponding to downward and upward polarization, respectively. The down-polarized domains exhibit higher currents, in line with the expected decrease in electrostatic average barrier height when polarization points toward the bottom electrode. Within these down-polarized regions, some spatial inhomogeneities in the current distribution are observed and they were consistently present across several repeated measurements and appear to be inevitable. They may arise from limitations such as tip degradation, local surface contamination, or slight variations in tip–sample contact conditions during CAFM mapping.

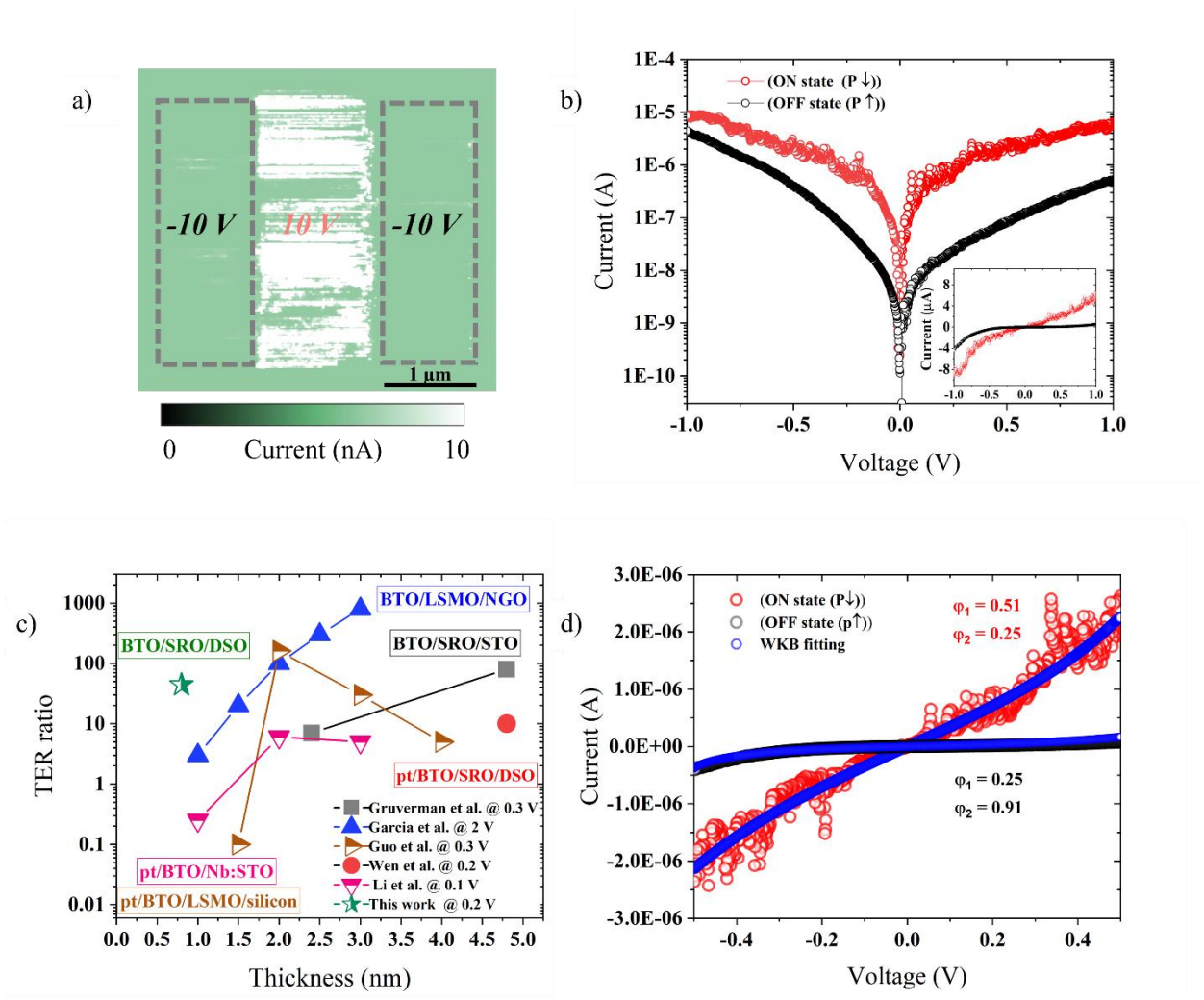


Figure 5.3 *(a) CAFM current map acquired at a read voltage of 1.5 V on a pABA-functionalized 2-unit cell BTO film after writing ferroelectric domains with ±10 V, showing higher current in the down-poled region (P↓) compared to the up-poled regions (P↑). (b) Representative short-range I–V curves acquired on down-poled (red, +10 V written) and up-poled (black) regions of the 2-unit cell pABA-functionalized BTO film, showing the polarization-dependent tunneling contrast used to extract the TER ratio. The insets display the same I–V data in linear scale. (c) Comparison of TER ratios as a function of ferroelectric barrier thickness from literature; the green star highlights the performance of this work (pABA-functionalized BTO/SRO/DSO). (d) WKB fitting of the I–V characteristics shown in (a), restricted to the low-bias range (–0.5 V to +0.5 V) where the WKB approximation is valid. Red open circles correspond to the ON-state current (P↓), black open circles to the OFF-state current (P↑), and the blue curves represent the corresponding WKB fits. The extracted barrier heights (φ_1, φ_2) for each polarization state are indicated in the figure.*

To more directly assess the polarization-dependent tunneling contribution, we performed point I–V measurements on selected down ↓ and up ↑ domains written with, respectively, +10 V and -10 V. The I-V measurements were measured at sub-coercive voltages (±1 V) to prevent switch-back during the measurement. The I-V curves show higher conductance on the down-poled regions (Fig. 5.3b), in agreement with the contrast observed in the CAFM current maps and with the expected polarization-modulated reduction of the average barrier height. We note that the absolute current values obtained in static I–V mode are higher than those extracted from CAFM maps around the same nominal read bias. Although the exact origin of this discrepancy cannot be unambiguously established, such differences are not uncommon in CAFM measurements[12] and may reflect practical factors such as the shorter dwell time per pixel during mapping versus spectroscopy mode. More reliable CAFM detection schemes can be achieved by coupling the AFM setup with an external voltage source–measured unit, as demonstrated in the work of Gruverman et al.[4]

Importantly, however, the qualitative trend—higher current on down-poled regions and lower current on up-poled ones—remains consistent, reinforcing the interpretation that the low-bias contrast arises from polarization-modulated tunneling. Furthermore, assuming a tip–sample contact area of approximately 20 nm in diameter, the corresponding ON-state current density values are estimated to be on the order of 1×10^6 A/cm². This magnitude is consistent with previously reported current densities for ultrathin BTO films measured by CAFM.[4] To place our findings in a broader context, we compiled previously reported TER ratios for various ferroelectric tunnel junctions using BTO films on different substrates and interfaces (Fig. 5.3c). Our data point (green star), is taken from the local contrast extracted from the point I–V measurements performed directly on down and up-poled regions, and it shows that despite the ultrathin 2-unit cell thickness

and the use of only a moderate compressive strain from a DSO substrate, our device exhibits an electroresistance ratio of approximately 45, that surpasses all previous quoted TER values in the sub-nm thickness range.

To further analyze the transport mechanism, the ON and OFF state currents shown in Fig. 5.3b were fitted using a Wentzel–Kramers–Brillouin (WKB) tunneling model, derived by Gruverman et al.,[4] as shown in Fig. 5.3d. This analytical approach has since been widely adopted in subsequent studies of ferroelectric tunnel junctions to extract effective barrier heights and elucidate polarization-dependent transport behavior in ultrathin films.[12–16] The model describes electron tunneling through an asymmetric trapezoidal barrier[17] defined by two interfacial barrier heights, φ_1 and φ_2. The derivation relies on the key assumption that the voltage is not too large:

$$J(V) = C * \frac{exp\left\{\alpha(V)\left[\left(\varphi^2 - \frac{eV}{2}\right)^{\frac{3}{2}} - \left(\varphi^1 + \frac{eV}{2}\right)^{\frac{3}{2}}\right]\right\}}{\left[\alpha(V)^2\left(\left(\varphi^2 - \frac{eV}{2}\right)^{\frac{1}{2}} - \left(\varphi^1 + \frac{eV}{2}\right)^{\frac{1}{2}}\right)^2\right]} \times sinh\left\{\alpha(V)\frac{3}{2}\left[(\varphi_2 - \frac{eV}{2})^{\frac{1}{2}} - (\varphi_1 + \frac{eV}{2})^{\frac{1}{2}}\right](\frac{eV}{2})\right\} \quad (5.1)$$

where C is a prefactor containing physical constants and $\alpha(V)$ is defined as:

$$\alpha(V) = \frac{4\,d\,(2m)^{\frac{1}{2}}}{[\,3\,\hbar\,(\,\varphi_1 + eV - \varphi_2\,)\,]} \quad (5.2)$$

Where m and d are the effective tunneling electron mass and barrier width respectively. We simplified the model by grouping constant terms into two phenomenological parameters C and α_0, while keeping φ_1 and φ_2, as the physically meaningful quantities describing the interfacial barrier heights. This preserves the voltage dependence of the WKB model while enabling stable numerical fitting.

$$\alpha_0 = \frac{4\,d\,(2m)^{\frac{1}{2}}}{3\,\hbar} \tag{5.3}$$

Because the WKB approximation is accurate only in the low-bias regime, the fitting was restricted to –0.5 to +0.5 V. Barrier heights were constrained to values 0–2 eV. Nonlinear Levenberg–Marquardt fitting in Origin yielded stable convergence and high goodness-of-fit ($R^2 \approx$ 0.97–0.98) for the ON-state currents. The extracted barrier heights were φ_1= **0.517 ± 0.076** eV and φ_2= **0.250 ± 0.016** eV. The OFF-state (high-resistance) currents exhibited only moderate agreement with the WKB model ($R^2 \approx 0.90$), and the fits were significantly more sensitive to initial conditions and parameter bounds. Nevertheless, approximate barrier values could be extracted, yielding φ_1= **0.25 ± 0.003** eV and φ_2= **0.91 ± 0.10** eV. To put these values into context, the extracted barrier heights are consistent in magnitude and relative asymmetry with those previously reported by Gruverman et al. for a 4.8 nm BTO tunnel junction, where φ values were reported as **0.48** and **0.96** eV for polarization pointing down (ON state), and **0.24** and **1.52** eV for polarization pointing up (OFF state). The poorer fit quality and the markedly asymmetric barrier profile can be an indication that the OFF-state transport mechanism is not dominated solely by direct tunneling. Such a conclusion would be consistent with prior reports on ferroelectric tunnel junctions, where the high-resistance state often transitions to thermionic (Schottky) emission or a mixed tunneling–thermionic transport regime, rather than pure quantum tunneling.[12]

5.3.1 Thickness dependence of the TER and mechanisms

Expanding the scope of our investigation, we also prepared and analyzed 1- and 4-unit cell BTO samples functionalized with pABA, to evaluate thickness-dependent tunneling phenomena.

For 1-unit cell sample, the phase contrast observed during the first scan immediately after writing showed a 180° difference between the down-poled domain and the surrounding area. However, this contrast was only apparent in the initial scan and tended to diminish in subsequent scans (Fig. 5.4a). The transient nature of the contrast suggests that it may not originate from a stable ferroelectric polarization but could instead result from surface charging effects or localized charge injection induced during the bias application. Furthermore, the amplitude does not display well defined domain walls.[18] Presently, it was not possible to establish whether the lack of contrast was due to lack of true ferroelectricity, fast domain relaxation, or the absolute value of the deformation of a 1- unit cell layer being too small for the PFM to detect it. We also cannot rule out incomplete formation of a homogeneous 1-unit cell BTO layer during the short deposition time of 5 minutes. Further HR-TEM analysis could help clarify this issue. For now, in any case, we regard this 1- unit cell sample as inconclusive.

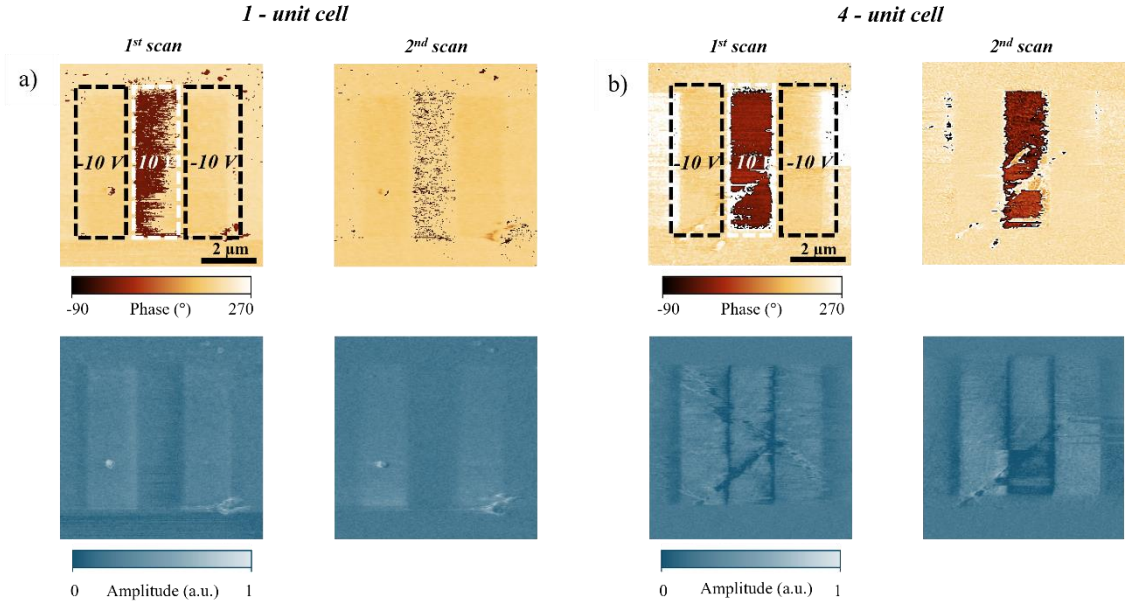


Figure 5.4 *PFM phase (upper panels) and amplitude (bottom panels) images of 1-unit cell (a) and 4-unit cell (b) BTO films after poling the samples with ±10 V, during first and second scan subsequently after writing. The images show a rapid disappearance of the phase contrast and an absence of well-defined*

amplitude signals at the domain boundaries for 1-unit cell sample, indicating an unstable or non-ferroelectric behavior.

For the 4-unit cell sample, clear signatures of stable polarization switching were observed, as evidenced by the persistent phase contrast in subsequent PFM scans (Fig. 5.4b) and the presence of well-defined amplitude signals at the domain walls—behavior consistent with that observed for the 2-unit cell film shown in Fig. 5.2. Moving on to the CAFM measurements, the 4-unit cell sample also exhibited distinct current signals in the down-poled regions (Fig. 5.5a), similar to those observed in the 2-unit cell samples. This behavior confirms that, in our pABA-functionalized BTO heterostructures, switching the polarization with stable screening of the switched domain is enabled by our organic molecules, thus facilitating resistive switching. The currents in the 4-unit cell film are notably lower than those of the 2-unit cell sample at the same read voltage (1.5 V, see scale bars in Fig. 5.3). This reduction is consistent with an expected decrease in total current density as the tunneling barrier thickness increases.[4,13,19]

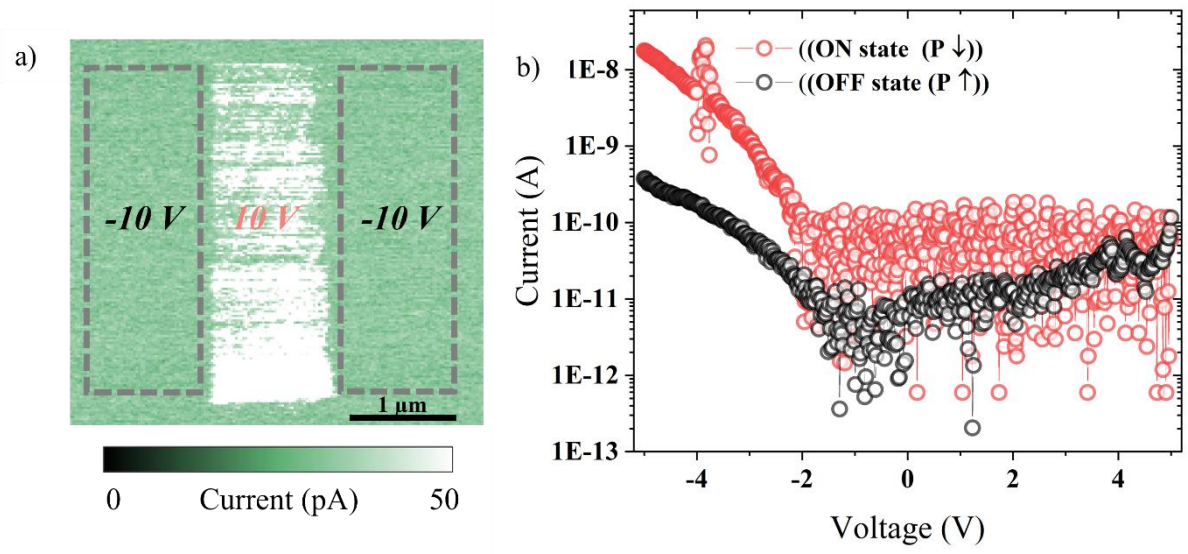


Figure 5.5 *CAFM current map acquired at a read voltage of 1.5 V on a pABA-functionalized 4-unit cell BTO film after writing domains with ±10 V, showing higher current in the down-poled region (P↓) compared*

to the up-poled regions (P↑). (b) shows the local I–V spectroscopy recorded directly on the written domain area, exhibiting suppressed low-bias current and asymmetric behavior at higher voltages.

Additionally, local I–V spectroscopy performed directly on the written domains (Fig. 5.5b) captures the transport characteristics of both the ON state (down-polarized, +10 V written) and the OFF state (up-polarized, −10 V written). In both polarization configurations, the current remains largely suppressed at low bias and increases more strongly beyond approximately −2 V, accompanied by a pronounced asymmetry between the positive and negative bias branches. Such rectifying-like behavior may indicate that transport in this thickness is increasingly influenced by thermionic injection processes, rather than pure tunneling conduction. These results suggest a gradual transition in the dominant transport mechanism as the barrier thickness increases[13,20], with the influence of thermally activated carrier injection becoming more pronounced in the 4-unit cell regime.

Based on the results obtained in the previous sections, particularly the CAFM current mappings and the direct short-range I–V measurements performed on pre-poled regions, the 2-unit-cell pABA-functionalized BTO film provides the most reliable and well-defined polarization-dependent tunneling response. This optimal thickness therefore serves as the basis for the next part of the study, where large-area top electrodes are added to enable macroscopic electrical characterization in a device-like structure.

5.4 Adding large-area top electrode for macroscopic measurements

5.4.1 Graphite flakes as soft top contact

In the present section, we employed graphite flakes as soft top electrodes, transferred via a stamping method designed to minimize surface damage and ensure preservation of the molecular interface in our pABA-functionalized 2-unit cell BTO films. Specifically, flakes were exfoliated from Highly Oriented Pyrolytic Graphite (HOPG) using a PDMS stamp and gently transferred onto the BTO surface at a mild temperature of ~60 °C to facilitate adhesion. The AFM topography and optical image of the flake is shown in Fig. 5.6a (approximate dimensions of 50 μm × 50 μm). Macroscopic I–V characterization was performed using a Radiant ferroelectric tester. In this setup, a triangular or pulsed voltage waveform is applied across the graphite/pABA/BTO/SRO heterostructure, while the resulting current is measured by a high-sensitivity charge integration circuit. This configuration allows the tester to accurately capture current–voltage response, providing complementary information to the local CAFM-based measurements.

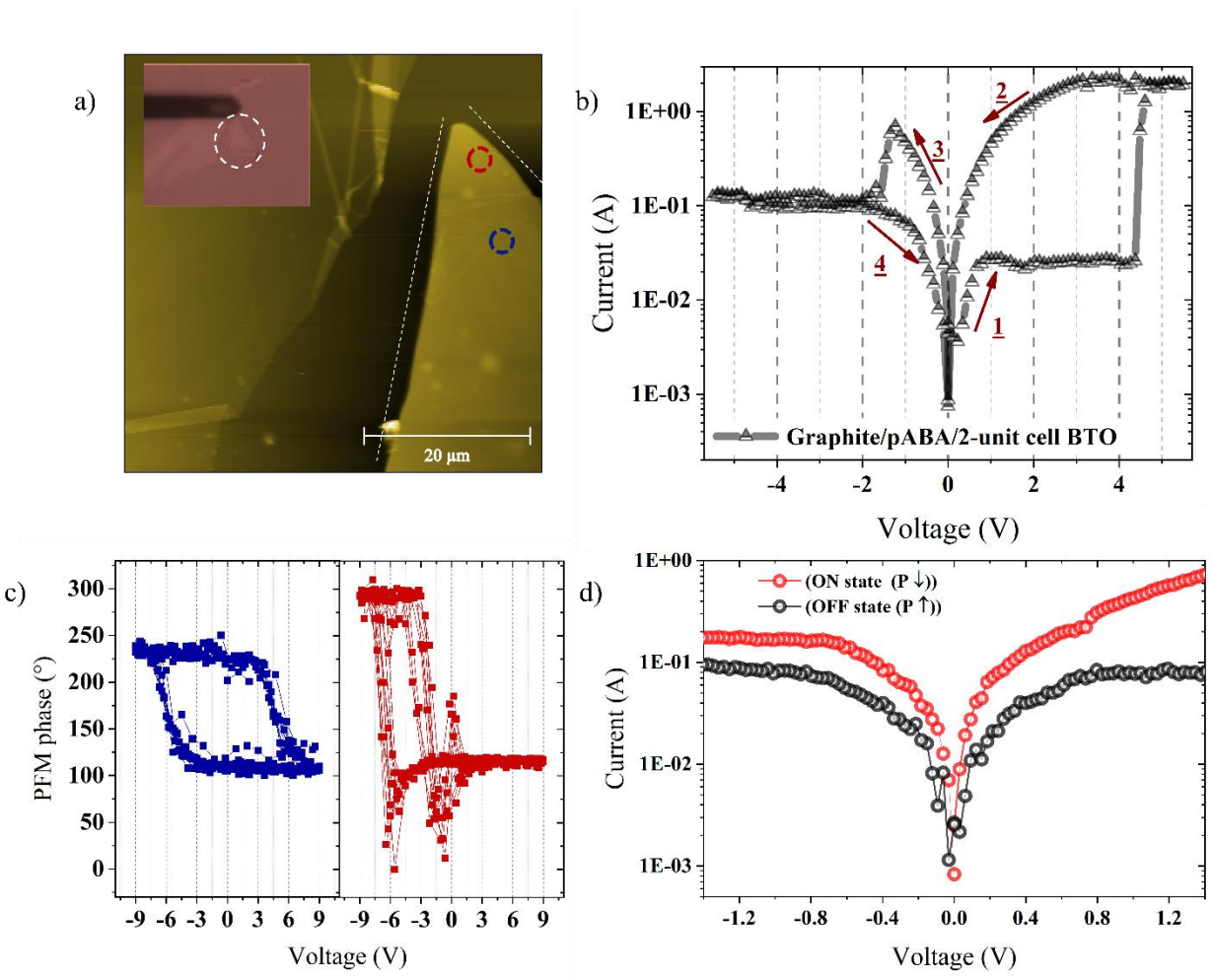


Figure 5.6 *Electrical characterization of graphite flakes used as soft top contacts on 2-unit cell BTO films. (a) AFM topography of the transferred graphite flake (inset shows optical image). (b) Representative long-range I–V sweep measured using a PDMS-transferred graphite flake. (c) PFM phase loops recorded on the graphite, showing location-dependent polarization switching behaviors. (d) Low-bias I–V measurements after presetting with +10 V (P↓) (red points) and –10 V (P↑) (black points), showing higher current in the down-polarized state.*

As shown in Fig. 5.6b, long-range voltage sweeps were performed on the graphite flake, and a representative I–V curve is shown. The I–V curve displays a current spike near 4 V, which is comparable to the coercive voltages previously obtained from SS-PFM measurements (Fig. 5.1c), suggesting that the observed current enhancement is linked to polarization switching. A clear

asymmetry in the I–V curve is evident between positive and negative voltage sweeps. For example, there is a noticeable drop in current around –2 V but increasing the negative voltage beyond this point does not fully restore the initial low-current state expected for OFF state configuration. The observed asymmetry could be related to imperfect integration of the graphite flake with the underlying pABA layer in our device structure. Any local detachment, contamination, or incomplete contact between the graphite and the organic interface could interfere with the effective screening or switching dynamics, thus preventing full reversal of polarization during the negative sweep. Further supporting this interpretation, PFM hysteresis loops acquired by contacting different parts of the graphite flake with the AFM tip (Fig. 5.6c) reveal two distinct switching behaviors. In some areas, loops resemble those obtained on pABA-functionalized BTO without graphite, albeit with a reduced phase shift of ~150°, likely suggesting partial switching or restricted forward domain growth. In other regions, a full 180° phase shift is observed, but the loops are shifted toward negative voltages, indicating a built-in electric field that favors down-polarized domains—potentially stabilized by the overlying graphite layer. In the future, optimized electrode preparation, e.g. following the approach outlined in Ref.[21] with graphene or graphite patches, together with the pABA molecular layer, may help in obtaining a more homogeneous electrical contact.

To directly assess the effect of polarization orientation on the tunneling current, we performed low-bias I–V measurements after presetting the sample with +10 V (to induce downward polarization) and –10 V (to induce upward polarization), as shown in Fig. 5.6d. The resulting curves display a higher current in the down-polarized state, consistent with polarization-modulated average barrier height, giving rise to tunneling electroresistance effect. Considering the approximate size of the graphite flake used as the top electrode, the estimated current density

values are almost on the order of 1×10^5 A/cm^{-2}, which is about one order of magnitude lower than those obtained from the local short range I–V measurements presented in Fig. 5.3.

5.5 Concluding remarks

In summary, we have demonstrated that stable polarization switching can be achieved in BTO films as thin as 2-unit cells when functionalized with a pABA molecular layer, a prerequisite for realizing ferroelectric tunnel junctions. Using conductive AFM, we investigated the tunneling response of these ultrathin films and explored the transport mechanisms underlying the resistive switching behavior. While our work establishes a consistent framework for analyzing resistive switching in molecularly functionalized ultrathin FTJs, there remain several directions for improvement.

In particular, electrodes other than the tip of an AFM are needed for real devices, and the attempt with graphite transfer has yielded mixed results: there is TER, but with a lower value than in AFM-based measurements, and switching spectroscopy suggests inhomogeneous interfacial quality. Better integration of graphene/graphite electrodes with the pABA molecular layer could help ensure a clean and reliable contact between the electrode, the organic layer, and the BTO surface, thereby enhancing the TER. The use of lithographically defined electrode areas would also allow better control over junction size and reproducibility. Finally, temperature dependance measurements would further confirm the tunneling characteristics of the transport mechanism. Together, these refinements could enhance device performance and further clarify the conduction mechanisms at play in ultrathin ferroelectric tunnel junctions.

References

1 H. Kohlstedt, N.A. Pertsev, J. Rodríguez Contreras, and R. Waser, “Theoretical current-voltage characteristics of ferroelectric tunnel junctions,” Phys. Rev. B 72(12), 125341 (2005).

2 M.Ye. Zhuravlev, R.F. Sabirianov, S.S. Jaswal, and E.Y. Tsymbal, “Giant Electroresistance in Ferroelectric Tunnel Junctions,” Phys. Rev. Lett. 94(24), 246802 (2005).

3 V. Garcia, S. Fusil, K. Bouzehouane, S. Enouz-Vedrenne, N.D. Mathur, A. Barthélémy, and M. Bibes, “Giant tunnel electroresistance for non-destructive readout of ferroelectric states,” Nature 460(7251), 81–84 (2009).

4 A. Gruverman, D. Wu, H. Lu, Y. Wang, H.W. Jang, C.M. Folkman, M.Y. Zhuravlev, D. Felker, M. Rzchowski, C.B. Eom, and E.Y. Tsymbal, “Tunneling electroresistance effect in ferroelectric tunnel junctions at the nanoscale,” Nano Lett. 9(10), 3539–3543 (2009).

5 R. Guo, Z. Wang, S. Zeng, K. Han, L. Huang, D.G. Schlom, T. Venkatesan, Ariando, and J. Chen, “Functional ferroelectric tunnel junctions on silicon,” Sci. Rep. 5(1), 12576 (2015).

6 Z. Wen, L. You, J. Wang, A. Li, and D. Wu, “Temperature-dependent tunneling electroresistance in Pt/BaTiO3/SrRuO3 ferroelectric tunnel junctions,” Appl. Phys. Lett. 103(13), (2013).

7 C. Li, L. Huang, T. Li, W. Lü, X. Qiu, Z. Huang, Z. Liu, S. Zeng, R. Guo, Y. Zhao, K. Zeng, M. Coey, J. Chen, Ariando, and T. Venkatesan, “Ultrathin BaTiO3-Based Ferroelectric Tunnel Junctions through Interface Engineering,” Nano Lett. 15(4), 2568–2573 (2015).

8 M. Lv, J. Wang, M. Tian, N. Wan, W. Tong, C. Duan, and J. Xue, “Multiresistance states in ferro- and antiferroelectric trilayer boron nitride,” Nat. Commun. 15(1), 295 (2024).

9 R. Soni, A. Petraru, P. Meuffels, O. Vavra, M. Ziegler, S.K. Kim, D.S. Jeong, N.A. Pertsev, and H. Kohlstedt, “Giant electrode effect on tunnelling electroresistance in ferroelectric tunnel junctions,” Nat. Commun. 5(1), 5414 (2014).

10 P. Maksymovych, S. Jesse, P. Yu, R. Ramesh, A.P. Baddorf, and S. V. Kalininl, “Polarization control of electron tunneling into ferroelectric surfaces,” Science (1979). 324(5933), 1421–1425 (2009).

11 M. Lanza, U. Celano, and F. Miao, “Nanoscale characterization of resistive switching using advanced conductive atomic force microscopy based setups,” J. Electroceram. 39(1–4), 94–108 (2017).

12 W. Jin Hu, Z. Wang, W. Yu, and T. Wu, “Optically controlled electroresistance and electrically controlled photovoltage in ferroelectric tunnel junctions,” Nat. Commun. 7(1), 10808 (2016).

13 D. Pantel, and M. Alexe, “Electroresistance effects in ferroelectric tunnel barriers,” Phys. Rev. B 82(13), 134105 (2010).

14 L. Wang, M.R. Cho, Y.J. Shin, J.R. Kim, S. Das, J.-G. Yoon, J.-S. Chung, and T.W. Noh, “Overcoming the Fundamental Barrier Thickness Limits of Ferroelectric Tunnel Junctions through BaTiO3 /SrTiO3 Composite Barriers,” Nano Lett. 16(6), 3911–3918 (2016).

15 Z. Xi, J. Ruan, C. Li, C. Zheng, Z. Wen, J. Dai, A. Li, and D. Wu, “Giant tunnelling electroresistance in metal/ferroelectric/semiconductor tunnel junctions by engineering the Schottky barrier,” Nat. Commun. 8, (2017).

16 L.-P. Tan, X.-F. Hu, A.-L. Li, W.-W. Qing, M. Zhou, D.-B. Yu, G.-P. Zhang, Q.-Q. Mu, Z.-L. Wang, X.-L. Wang, Y.-L. Bi, and W. Zhang, “Observation of out-of-plane ferroelectricity in ∼5 nm ultrathin SrBi2Ta2O9 films for memristors and synapses application,” Chemical Engineering Journal 528, 171951 (2026).

17 W.F. Brinkman, R.C. Dynes, and J.M. Rowell, “Tunneling Conductance of Asymmetrical Barriers,” J. Appl. Phys. 41(5), 1915–1921 (1970).

18 C. Lichtensteiger, S. Fernandez-Pena, C. Weymann, P. Zubko, and J.M. Triscone, “Tuning of the depolarization field and nanodomain structure in ferroelectric thin films,” Nano Lett. 14(8), 4205–4211 (2014).

19 V. Garcia, and M. Bibes, “Ferroelectric tunnel junctions for information storage and processing,” Nat. Commun. 5(1), 4289 (2014).

20 R. Duan, J. Yan, D. Meng, Y. Wang, D. Xu, M. Zhang, D. Yu, K. Tang, J. Dong, D. Han, and X. Zhang, “A van der Waals ferroelectric switchable diode with ultra-high nonlinearity factor,” Appl. Surf. Sci. 693, 162792 (2025).

21 H. Lu, A. Lipatov, S. Ryu, D.J. Kim, H. Lee, M.Y. Zhuravlev, C.B. Eom, E.Y. Tsymbal, A. Sinitskii, and A. Gruverman, “Ferroelectric tunnel junctions with graphene electrodes,” Nat. Commun. 5(1), 5518 (2014).

6 Summary and outlook

6.1 Summary

In this thesis, my primary goal was to address some of the key challenges associated with ferroelectric thin films and to highlight the crucial role played by depolarizing fields in determining their performance. The strategy was to explore alternatives to conventional screening mechanisms by employing **molecular electrodes**, referring specifically to organic molecules with resonance structures. Accordingly, the central focus of this work has been the study of the ferroelectric functionalities of BTO thin films functionalized with pABA. I began by optimizing the growth of high-quality BTO/SRO structures on DSO substrates using RF-sputtering, as this formed the basis for all subsequent functionality studies.

Chapter 2: Through growth optimization, I demonstrated how the dynamic interplay between growth parameters can induce transitions between different growth modes. In particular, I showed that increasing the sputtering power, which enhances the flux of energetic ions and the surface diffusivity of adatoms, results in a transition from island-like growth mode with trenches to a more desirable two-dimensional, layer-by-layer morphology.

Chapter 3: I investigated switching dynamics in the BTO thin films through a series of writing-speed experiments and demonstrated that, in bare BTO, screening by atmospheric adsorbates fails to maintain homogeneous domain formation beyond a critical writing speed, due to the slow reorientation of adsorbates required to screen the switched polarization. By contrast, incorporation of pABA molecules significantly mitigated this constraint, enabling stable domain writing up to speeds of ~1 mm/s—an improvement by at least a factor of 22 relative to bare BTO surfaces. The thickness of the pABA-functionalized domains also showed a much lower dependence on writing speed than their bare-BTO counterparts.

Chapter 4: I also looked at the long-term stability of written domains as a function of thickness. Reducing the thickness of bare BTO below ~10 nm thickness, results in domain back-switching and loss of macroscopic polarization on a time scale of minutes. Further thinning leads to rapid back-switching and a marked suppression of the measurable polarization magnitude. In contrast, incorporating pABA molecules substantially reinforces polarization stability across all thicknesses examined: regardless of the initial domain configuration, both polarization directions could be uniformly and stably written down to a thickness of 2-unit cells.

Chapter 5: Through nanoscale current-transport measurements, I showed that, in the ultrathin regime where polarization is stabilized via the pABA molecular layer, the average barrier height for electron tunneling is modulated by the polarization direction, resulting in higher tunneling currents when the polarization points downward, toward the bottom electrode (Low Resistance State(LRS)) and lower currents when it points upward (High Resistance State(HRS)). For the 2-unit cell sample, the corresponding TER ratio reached values of approximately 45, which is at least one order of magnitude higher than those typically reported for BTO films of comparable thickness. Large-area graphite electrodes placed on pABA-functionalized-2-unit-cell BTO/SRO/DSO structures, reproduce the same polarity-dependent current contrast: downward polarization consistently yields higher current compared to the upward orientation. These results point to pABA as a promising pathway for improving ferroelectric tunnel junctions.

6.2 Future works

Beyond the scope of the discussions presented in this thesis, the work carried out here opens several promising directions for future research.

- Other ferroelectrics. A natural extension would be to explore pABA functionalization on a broader range of ferroelectric materials. It would be valuable to examine whether the strong surface bonding observed between pABA and BTO—and more generally, the interaction of conjugated organic molecules capable of delocalized electronic resonance—can be replicated on other ferroelectric surfaces. Such studies may reveal whether similar enhancements in switching dynamics and stability can be achieved in ultrathin ferroelectrics. In addition, applying these concepts to antiferroelectric systems that undergo ferroelectric transitions below a critical thickness could offer an efficient route toward stabilizing ferroelectricity in otherwise unstable regimes.

- Photovoltaics. Beyond the role of pABA molecules for screening depolarizing fields agents to improve switching dynamics and stabilize polarization in ultrathin ferroelectric films, as demonstrated in this thesis, I believe there are further interesting opportunities for future works, in which pABA molecules can be utilized. pABA molecules are already used in organic–inorganic hybrid Perovskite Solar Cells (PSCs), where adding the molecular layer enhances power conversion efficiency and open circuit voltage by minimizing charge recombination.[1] Also, adsorption studies of pABA on TiO_2 surfaces has showed that incorporation of the molecular layer enables sub-bandgap absorption, resulting in reduction in optical bandgap observed in UV-visible spectrum.[2] These observations suggest that exploring such interfacial engineering strategies in ferroelectric materials may provide pathways to enhance photocurrent generation or broaden absorption spectra in ferroelectric devices.

- Coupled functionalities. A final intriguing avenue involves coupling ferroelectric tunnel junctions with photovoltaic effects. There are works that have previously investigated coupling, however, the report was mostly focused on engineering resistive states of the ferroelectric tunnel

junction, by photovoltaic effect in a Nb-doped STO substrate.[3] In this medium, the ferroelectric layer itself is not considered as the light sensing medium: the doped substrate absorbs the light and generates the electron-hole pairs, and the ferroelectric layer separates them. If pABA functionalization can indeed reduce the optical bandgap of ferroelectrics such as BTO, as suggested by related studies, the ferroelectric material itself can absorb more light and, promote charge separation/reduce charge recombination when polarization-controlled depletion widths become comparable to the film thickness.[4] Under such conditions, both tunneling currents and photovoltaic contributions could traverse the same medium being the ferroelectric layer, potentially leading to increased current densities and/or novel device functionalities.

References

1 Y. Zou, Y. Liang, C. Mu, and J.P. Zhang, “Enhancement of Open-Circuit Voltage of Perovskite Solar Cells by Interfacial Modification with p-Aminobenzoic Acid,” Adv Mater Interfaces 7(1), (2020).

2 A.G. Thomas, M.J. Jackman, M. Wagstaffe, H. Radtke, K. Syres, J. Adell, A. Lévy, and N. Martsinovich, “Adsorption Studies of p-Aminobenzoic Acid on the Anatase TiO2(101) Surface,” Langmuir 30(41), 12306–12314 (2014).

3 W. Jin Hu, Z. Wang, W. Yu, and T. Wu, “Optically controlled electroresistance and electrically controlled photovoltage in ferroelectric tunnel junctions,” Nat Commun 7(1), 10808 (2016).

4 Z. Tan, L. Hong, Z. Fan, J. Tian, L. Zhang, Y. Jiang, Z. Hou, D. Chen, M. Qin, M. Zeng, J. Gao, X. Lu, G. Zhou, X. Gao, and J.-M. Liu, “Thinning ferroelectric films for high-efficiency photovoltaics based on the Schottky barrier effect,” NPG Asia Mater 11(1), 20 (2019).

7 Appendix

Appendix A: Fundamentals of piezoresponse force microscopy

Local poling of ferroelectrics by AFM was first demonstrated by Güthner and Dransfeld (1992)[1], who polarized nanometer-sized regions in a poly(vinylidene fluoride–trifluoroethylene) film by applying a DC bias between a conductive tip and the bottom electrode. The resulting piezoelectric vibration was detected through the cantilever deflection under an applied AC signal, marking the first realization of nanoscale polarization control and detection. The subsequent development of PFM transformed this concept into a versatile tool for probing ferroelectric behavior at the nanoscale. PFM is a contact AFM-based technique in which a conductive AFM tip acts simultaneously as a local top electrode and as a mechanical deflection sensor while scanning the sample surface. The principle of the method relies on the inverse piezoelectric effect, where a piezoelectric material undergoes mechanical deformation in response to an applied electric field. By applying a small AC modulation voltage through the conductive tip in contact with the surface, the resulting electromechanical vibration of the sample is transmitted to the cantilever. The oscillation amplitude reflects the magnitude of the local piezoelectric response, while the phase shift relative to the driving voltage reveals the orientation of the polarization (upward or downward). In addition to vertical PFM, where out-of-plane sample deformation is detected as cantilever deflection, PFM can also be performed in lateral mode, in which in-plane piezoresponse is measured through cantilever torsion.

Beyond imaging domain structures, PFM provides direct access to the functional electromechanical properties of ferroelectrics, such as local hysteresis behavior and coercive voltage, through SS-PFM, under operating conditions. During lithography and SS-PFM, the application of a DC bias larger than the coercive voltage to the AFM tip—either in static contact or during scanning—enables local modification of polarization through the process of polarization

switching. This combination of AC excitation and DC bias control allows both the imaging and manipulation of ferroelectric domains, making PFM a powerful tool for investigating switching dynamics and domain evolution at the nanoscale.[2]

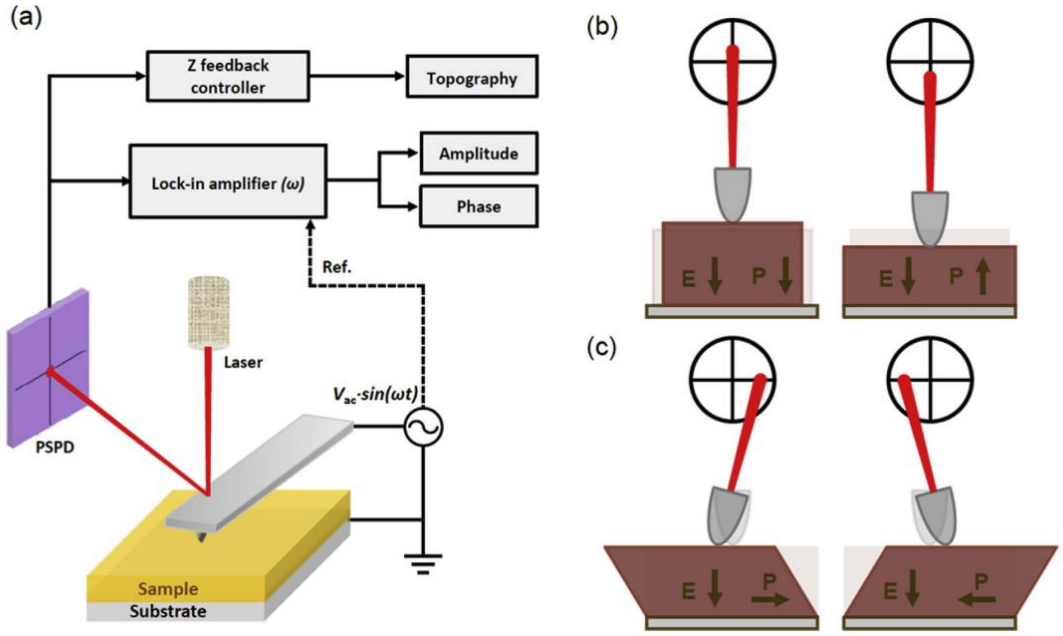


Figure A.1 *(a) Schematic PFM setup, and the principle of (b) vertical and (c) lateral PFMs, adapted from Ref [3].*

In PFM, the measured piezoresponse amplitude, A, consists of three major contributions: the true electromechanical response of the material (A_{piezo}), electrostatic interactions between the tip and sample (A_{el}), and non-local contributions arising from long-range capacitive interactions between the cantilever body and the surface (A_{nl}).[3,4] For reliable quantitative imaging, it is crucial to maximize A_{piezo}, thereby ensuring that the observed contrast predominantly reflects electromechanical effects. Depending on the tip–sample interaction regime, the nature of the signal varies. In the strong indentation regime, the contact is sufficient to directly extract piezoelectric coefficients, offering quantitative insight into the material's ferroelectric response. In contrast, the

weak indentation regime still allows for indirect extraction of ferroelectric behavior, though the measurements are more sensitive to the local surface conditions. In the purely electrostatic regime, however, long-range interactions dominate, and the piezoelectric properties become inaccessible.

References

1 P. Güthner, and K. Dransfeld, “Local poling of ferroelectric polymers by scanning force microscopy,” Appl Phys Lett 61(9), 1137–1139 (1992).

2 I. Spasojević (Author), N. Domingo Marimon (Director), and G. Catalán Bernabé (Director), Interplay Between Ferroelectricity and Surface Chemistry in BaTiO3, 2022.

3 D. Seol, B. Kim, and Y. Kim, “Non-piezoelectric effects in piezoresponse force microscopy,” Current Applied Physics 17(5), 661–674 (2017).

4 S. V. Kalinin, and D.A. Bonnell, “Contrast Mechanism Maps for Piezoresponse Force Microscopy,” J Mater Res 17(5), 936–939 (2002).

Appendix B: Strain analysis of BTO/SRO films on different substrates

This appendix summarizes complementary investigations performed to understand how substrate-induced strain influences the structural and functional behavior of BTO/SRO heterostructures. These studies provided the initial framework for substrate selection and strain control, in the work discussed in the main chapters.

B.1 Introduction

The choice and preparation of the substrate is substantially critical in functionalities of ferroelectric thin films. The substrate lattice constant dictates the strain imposed on the overlaying film: lattice-matched substrates enable growth close to the film's natural state, while lattice-mismatched substrates can impose compressive or tensile strain that substantially modifies functional properties.[1,2] Coherently strained BTO, for example, shows transition temperatures hundreds of degrees higher and markedly larger remanent polarization than bulk, underscoring the leverage of substrate-imposed strain.[3] Importantly, strain has also been shown to strongly influence coercive fields: both experiments and phase-field simulations demonstrate that modest changes in epitaxial strain can lead to large variations in switching fields, linked to changes in domain wall mobility, polarization variants, and phase coexistence.[4,5] Equally important is how strain evolves with thickness. As films thicken, relaxation occurs and—crucially—often does so inhomogeneously, producing strain gradients rather than a single uniform strain value; these gradients couple to polarization via the flexoelectric effect and can smear dielectric anomalies and depress permittivity.[6] In $Ba_{0.5}Sr_{0.5}TiO_3$, such thickness-dependent relaxation shifts the apparent Curie temperature and lowers the dielectric constant at high compressive strain, directly linking

strain state to dielectric response.[7] Moreover, theory shows that flexoelectric coupling can raise the critical thickness for switchable ferroelectricity because strain gradients are unidirectional rather than bipolar.[8]

Based on what we have discussed, strain states strongly influence the quality and functional performance of ferroelectric thin films. The following section details the PLD–based strain analysis performed on BTO/SRO heterostructures grown on substrates with different lattice mismatches. These investigations encompass a systematic study of strain accommodation across several strain series, including the effects of film and electrode thickness on relaxation behavior. In addition, complementary X-ray Photoelectron Spectroscopy (XPS) analyses were carried out to evaluate near-surface cation stoichiometry and its correlation with the degree of relaxation. Together, these results define the optimal lattice-mismatch window for coherent growth and reveal how structural and compositional factors evolve as strain relaxes. Furthermore, preliminary ferroelectric benchmarking was performed by SS-PFM to assess the switching behavior of the optimized heterostructures. The insights obtained from these PLD experiments established the substrate selection criteria and provided the fundamental guidelines for the growth-mode optimization studies presented in the main text.

B.2 Pulsed laser deposition: strain analysis

In PLD, an intense laser pulse is focused onto the target surface, where its electromagnetic energy is first converted into electronic excitations which subsequently relax into thermal, chemical, and mechanical energy within the lattice. These processes result in material removal through evaporation and ablation, producing a plasma plume containing a mixture of energetic species—atoms, ions, electrons, clusters, and even micron-sized particulates. The plume has a highly directed, dense shape that rapidly expands in the vacuum chamber to create a jet of material directed normal to the target surface.[9,10] This plasma plume is directed towards a heated single crystal placed opposite the target; upon touching the surface of the crystal, the species in the plume condense and crystallize, slowly forming a thin film.

B.2.1 Growth of BTO/SRO heterostructures under substrate-induced strain

BTO/SRO bilayers were deposited on (001)-oriented STO, (110)-oriented $GdScO_3$ (GSO) and $SmScO_3$ (SSO), and (110)-oriented $NdScO_3$ (NSO) substrates using a PLD system with a KrF excimer laser (λ = 248 nm). These substrates impose different strain state on the BTO and SRO layers. The corresponding lattice misfits between the substrates and the BTO/SRO layers are summarized in Table B.1. The deposition temperatures were 635 °C for SRO and 700 °C for BTO, with both layers grown in an oxygen atmosphere at a partial pressure of 100 mTorr. The laser spot size on the target during growth was kept constant at 0.02 cm^2. In all cases, the SRO layer was deposited with a fixed laser energy of 110 mJ (unless otherwise stated), while the thickness was adjusted by varying the number of laser pulses. For BTO, however, the laser energies varied across

different strain-series experiments. In the 1st strain series, both SRO and BTO were grown at 110 mJ, resulting in an SRO thickness of ~13 nm and a BTO thickness in the range of 22–26 nm.

Table B.1 *Lattice mismatch values between different substrates and SRO (3.930 Å) and BTO (4.000 Å).*

Substrate	Pseudo cubic a (Å)	Misfit vs SRO %	Misfit vs BTO %
STO	3.905	-0.64 %	-2.38 %
GSO	3.968	+0.97 %	-0.80 %
SSO	3.986	+1.43 %	-0.35 %
NSO	4.011	+2.06 %	+0.28 %

To investigate the strain state of epitaxial SRO/BTO bilayers, we have recorded RSM around substrate Bragg reflection. In RSM, the diffracted intensity is mapped as a function of the in-plane (Qx) and out-of-plane (Qz) components of the scattering vector. This allows the simultaneous determination of the in-plane and out-of-plane lattice parameters, thereby providing direct insight into whether the film is coherently strained to the substrate or has undergone partial relaxation. RSM results on our 1st strain series (Fig. B.1) revealed that BTO and SRO films grown on SSO and GSO remain coherently strained to the substrates. In contrast, for NSO, the relatively large lattice misfit drives relaxation: even though the SRO layer is only ~13 nm thick, it is partially relaxed, and the overlying BTO follows the same trend. However, for films grown on STO, while SRO remains mostly strained to the substrate—although a subtle shoulder on the right-hand side of the SRO peak indicates incipient relaxation—the BTO layer exhibits pronounced relaxation despite being below the critical thickness reported for BTO/STO heterostructures.[11] Although it is

possible that this slight relaxation of SRO influences the relaxation of BTO, these results were particularly surprising given that our own later experiments with thicker BTO films (grown on correspondingly thicker SRO layers, discussed in the 3rd strain series) showed that BTO can remain coherently strained on STO.

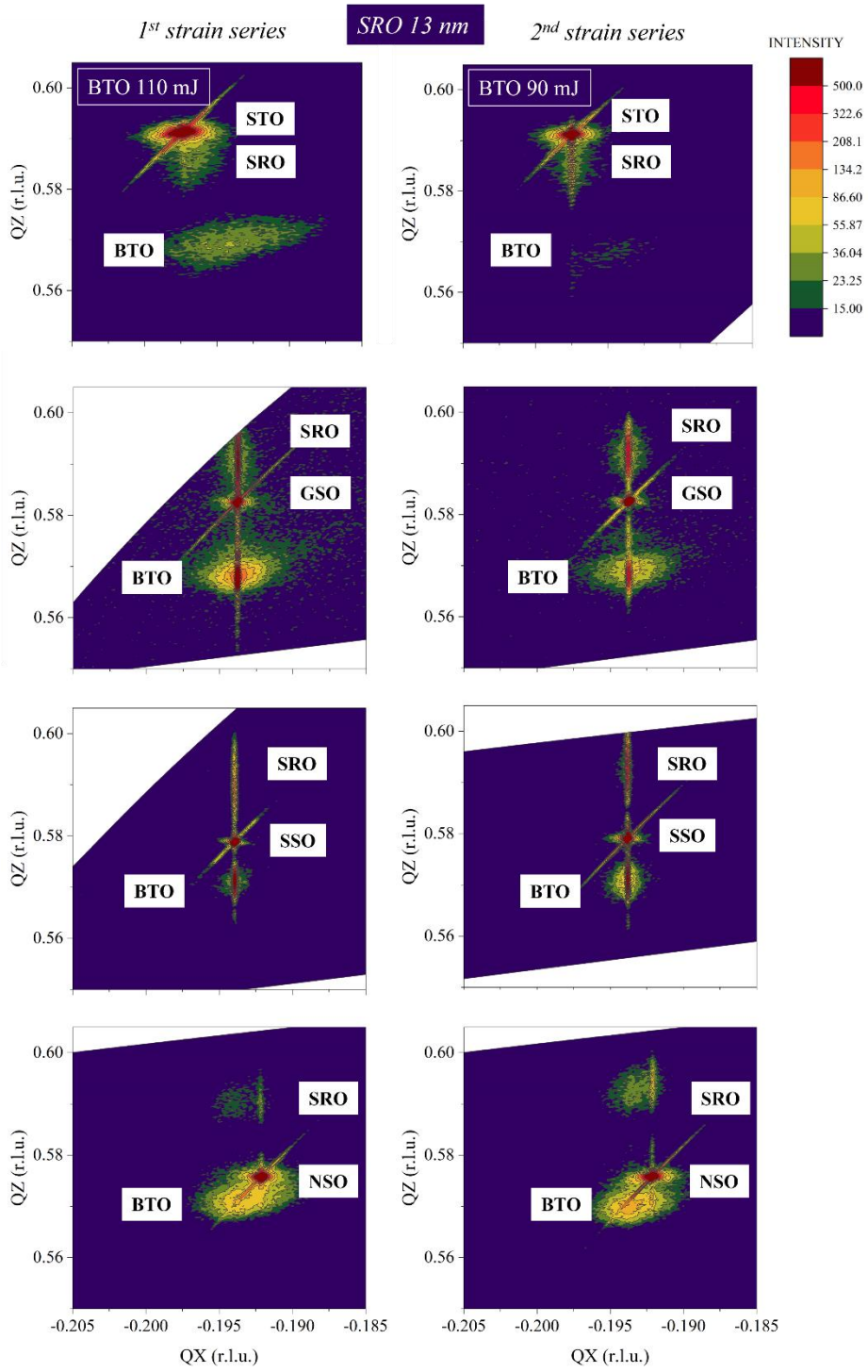


Figure B.1 *RSMs of the 1st and 2nd strain-series BTO/SRO bilayers, collected around the (–103) reflection for STO and the (33-2) reflections for GSO, SSO, and NSO. In both series, SRO was grown at 110 mJ to a thickness of ≈13 nm, while the BTO laser energy was 110 mJ (1st series) and 90 mJ (2nd series). Coherent*

strain is observed for GSO and SSO, partial relaxation of both SRO and BTO was observed for NSO substrates, and notable relaxation of BTO on STO.

To verify this anomalous relaxation behavior, a 2nd strain series was grown under identical conditions for SRO but modified conditions for BTO: the deposition energy was reduced to 90 mJ, yielding thinner BTO layers. Again, BTO on STO exhibited partial relaxation, consistent with the earlier results; however, in this case, the right-hand shoulder of the SRO peak was no longer observed. These findings suggest that the strain states of both layers are strongly interdependent, with relaxation arising from their mutual structural interaction rather than from the isolated thickness effect of either layer.

In 3rd strain series (Fig. B.2), the NSO substrate was omitted, since even a 13 nm SRO bottom layer was already partially relaxed on NSO, making it unsuitable for further study. In this series, SRO was grown with an increased number of laser pulses, yielding a thickness of ~40 nm, while the BTO fluence and thickness were kept identical to strain series 1. Interestingly, on STO, both SRO and the overlying BTO now appeared much less relaxed, confirming that the improved strain coherence is related to the increased SRO thickness rather than an isolated BTO effect. The exact mechanism behind this dependence remains unclear, but the increased SRO thickness likely allows partial accommodation of the lattice mismatch due to the metallic and somewhat ductile nature of SRO, which can locally expand near the interface and thus relieve part of the stress transmitted to BTO. Conversely, on SSO, increasing the SRO thickness led to its relaxation, with the BTO layer grown on top following the same trend. From these results, we infer that the critical thickness for maintaining fully strained SRO is below 13 nm on NSO and between 13 nm and 40 nm on SSO. Based on these observations—and considering the need for a sufficiently thick and

conductive SRO bottom electrode for the electrical measurements carried out in this thesis—we conclude that, for our purposes, the most suitable substrates for growing BTO/SRO bilayers are those with lattice mismatches in the range of approximately –0.6% to +0.97%, corresponding to STO and GSO, respectively.

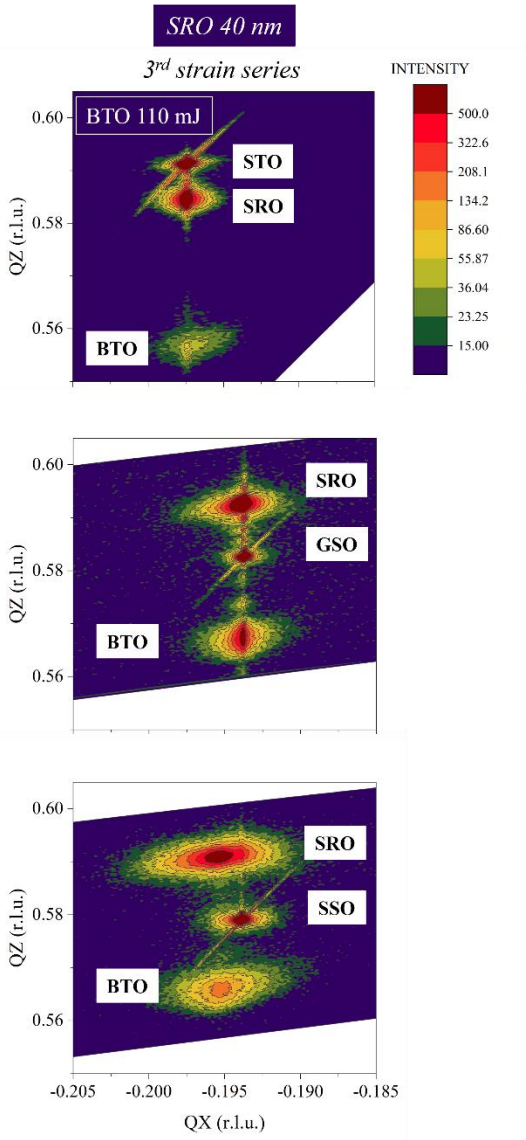


Figure B.2 *RSMs of the 3rd strain series for BTO/SRO bilayers grown on (001) STO, (110) GSO, and (110) SSO substrates. In this series, the SRO bottom layer was deposited with a laser energy of 110 mJ and increased thickness of ~40 nm (controlled by number of pulses), while BTO was grown with laser energy of 110 mJ at ~22–26 nm thickness. For STO, both SRO and BTO remain coherently strained to the substrate,*

in contrast to the first strain series where partial relaxation of BTO was observed. On GSO, both layers are strained, while on SSO, the SRO layer shows partial relaxation, which propagates to the BTO film grown on top.

B.2.2 Effect of epitaxial strain and relaxation on surface stoichiometry

In the previous section, we investigated the strain states of our BTO/SRO bilayers grown on different substrates and identified a lattice-mismatch window between approximately –0.6 % and +0.97 % (corresponding to STO and GSO) as optimal for our purposes, ensuring coherent epitaxial growth. Building on those findings, we next aimed to explore whether epitaxial strain could also influence the chemical composition of our films. Maintaining a balanced cation stoichiometry in BTO is critical for achieving stable ferroelectric properties and reproducible lattice parameters, since deviations such as Ba excess or Ti deficiency can lead to lattice expansion, defect formation, and altered polarization behavior. Therefore, after completing the strain-dependence studies, we performed a detailed stoichiometric analysis of our films using XPS. XPS is a surface-sensitive technique that provides quantitative information on the elemental composition and chemical states of materials. It is based on the detection of photoelectrons emitted from core levels upon irradiation with monochromatic X-rays. The measured binding energies allow identification of the present elements, while chemical shifts in the core-level peaks provide insight into oxidation states, bonding environments, and possible defects. Because its probing depth is limited to a few nanometers, XPS is particularly valuable for thin-film systems where surface composition and interface quality strongly affect functional properties.

We first examined the stoichiometry of films from the 3rd strain series, where XPS revealed that both STO and GSO samples (nearly fully strained) were Ba-rich (Ba ≈ 61–62 %), whereas the relaxed SSO film was closer to stoichiometric (Ba ≈ 57 %, Ti ≈ 43 %). This observation suggested

that off stoichiometry may correlate with the degree of epitaxial strain rather than with the substrate itself. Motivated by this trend, we designed a follow-up study—the 4th strain series—to investigate more systematically whether stoichiometric deviations scale with strain relaxation.

For this purpose, a new set of BTO/SRO bilayers—referred to as the 4th strain series—was grown on STO substrates under compressive strain. In this series, the number of laser pulses used for BTO deposition was increased compared to the 3rd strain series, resulting in overall thicker films. However, within the 4th series, while the pulse number was kept constant for all samples, the laser energy was varied (70, 90, and 110 mJ). This combination produced films with different thicknesses and, consequently, different degrees of relaxation. The resulting BTO top layers had thicknesses of approximately 32 nm, 39 nm, and 46 nm, respectively. The SRO bottom electrode was deposited under identical conditions to the 3rd strain series. Along with reciprocal space mappings (Fig. B.3), XPS was again employed to assess the near-surface cation stoichiometry, focusing on the Ba/Ti ratio in relation to the degree of relaxation. The structural parameters, deposition conditions, and corresponding near-surface Ba/Ti atomic concentrations for the samples from both the 3rd and 4th strain series are summarized in Table B.2.

Table B.2 *Summary of growth parameters and near-surface Ba/Ti cation ratios for BTO/SRO bilayers in the 3rd and 4th strain series. The results indicate that stoichiometric deviations are closely associated with the degree of strain relaxation.*

3rd strain series (same energy, different substrates)	**Substrate**	**BTO energy (mJ)**	**Thickness/ pulse numbers**	Ba **%At Conc.**	**Ti %At Conc.**
	STO	110	26/331	61.3	38.7
	GSO	110	26/331	62	38
	SSO	110	23/331	57	43
4th strain series (same substrate, different energies)	**Substrate**	**BTO energy (mJ)**	**Thickness/ pulse numbers**	**Ba %At Conc.**	**Ti %At Conc.**
	STO	110	46/1000	51.77	48.23
	STO	90	39/1000	56.8	43.2
	STO	70	32/1000	59.3	40.6

As expected, partial relaxation was most pronounced in the thickest BTO film, a natural consequence of its higher thickness resulting from the increased pulse count relative to the 3rd strain series. Within the 4th strain series on STO (70/90/110 mJ), the thickest and most relaxed film (110 mJ) was the most stoichiometric (Ba ≈ 51.8 %, Ti ≈ 48.2 %), while thinner and more strained films (90 mJ and 70 mJ) were progressively Ba-rich. These observations demonstrate a clear correlation between strain relaxation and near-surface stoichiometry: as epitaxial constraint decreases, the films tend to recover closer to the ideal Ba/Ti ratio.

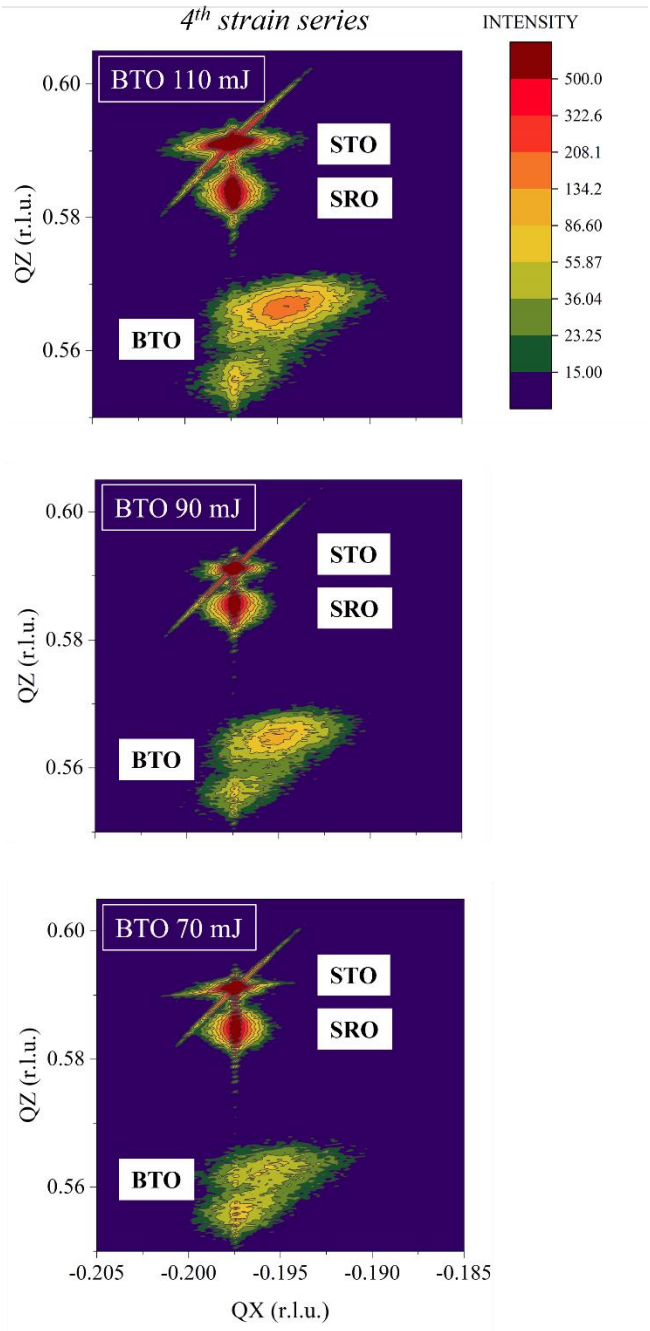


Figure B.3 *RSMs around the (–103) reflection of STO for the 4th strain series. All films consist of ~40 nm SRO bottom electrodes grown at 110 mJ, with BTO layers deposited at different laser energies (110, 90, and 70 mJ from left to right). The maps reveal the effect of laser energy on BTO lattice strain and relaxation behavior.*

Taken together, these comparisons indicate a consistent trend: stoichiometric deviations correlate primarily with the degree of epitaxial constraint, with larger deviations observed in fully strained films. This suggests that nonstoichiometry may act as an additional strain-accommodation mechanism, rather than being dictated by fluence or substrate identity.[12–14] Notably, previous work has shown that cation nonstoichiometry can significantly reduce the critical thickness for strain relaxation, and with optimized growth conditions, fully strained BTO films up to 200 nm have been demonstrated on GSO.[15] This behavior is often attributed to Ti deficiencies, which expand the out-of-plane lattice constant and promote premature relaxation as thickness increases.[16] Our results therefore imply that chemical nonstoichiometry and elastic relaxation are interconnected phenomena, with local compositional deviations contributing to strain relief in ultrathin BTO films. While literature also shows that oxygen pressure and laser fluence can be tuned to achieve nearly stoichiometric values even in fully strained films[15–17], such optimization was not pursued here; however, studies suggest that a more moderate oxygen pressure than the 100 mTorr used in this study could be beneficial. Finally, we emphasize that XPS is a surface-sensitive probe (≈ top few nanometers), and thus bulk stoichiometry throughout the film thickness would need to be assessed by Rutherford Backscattering Spectrometry (RBS) or other depth-averaging techniques to rule out possible gradients.

For the flow of this thesis, our goal in the PLD section was strain control. Having found that STO and GSO yield similarly off-stoichiometric fully strained films at the surface (where XPS probes), while SSO relaxes too readily, we turned to a preliminary SS-PFM hysteresis comparison between the fully strained STO- and GSO-based stacks. That quick screen (next section) helped us judge which lattice-parameter window was more promising for robust ferroelectric switching under our constraints.

B.2.3 Ferroelectric benchmarking on fully strained BTO/SRO bilayers analyzed by SS-PFM

To benchmark the ferroelectric response, SS-PFM measurements were performed on strained BTO/SRO bilayers grown on STO and GSO substrates with comparable thicknesses. Representative Phase–voltage loops are presented in Fig. B.4a. For films grown on STO, the loops are relatively narrow and exhibit low average coercive voltages. In contrast, those grown on GSO display broader loops with higher coercive voltages. This contrast can arise from the different epitaxial constraints imposed by the substrates. Theoretically and experimentally, both coercive fields and remnant polarizations are expected to decrease as compressive strain decreases, since weaker substrate clamping enhances domain wall mobility.[4,5] However, the relationship is not always straightforward. In particular, for example it has been reported that BTO films grown on GSO (lower compressive strain) exhibit larger coercive voltages but reduced remanent polarization compared to those on DSO (higher compressive strain) (Fig. B.4b).[3] In our case, BTO grown on STO likely develops a larger remnant spontaneous polarization (not directly visible in SS-PFM loops). However, the stronger compressive strain enhances depolarizing fields, which can result in back-switching and narrowing the loops. By contrast, BTO on GSO, with a smaller compressive misfit, experiences a reduced depolarizing burden, making the switched state more stable and producing wider loops. An additional factor may be the SRO bottom electrode: compressive on STO but tensile on GSO, which could influence interfacial electrostatics and domain-wall pinning.

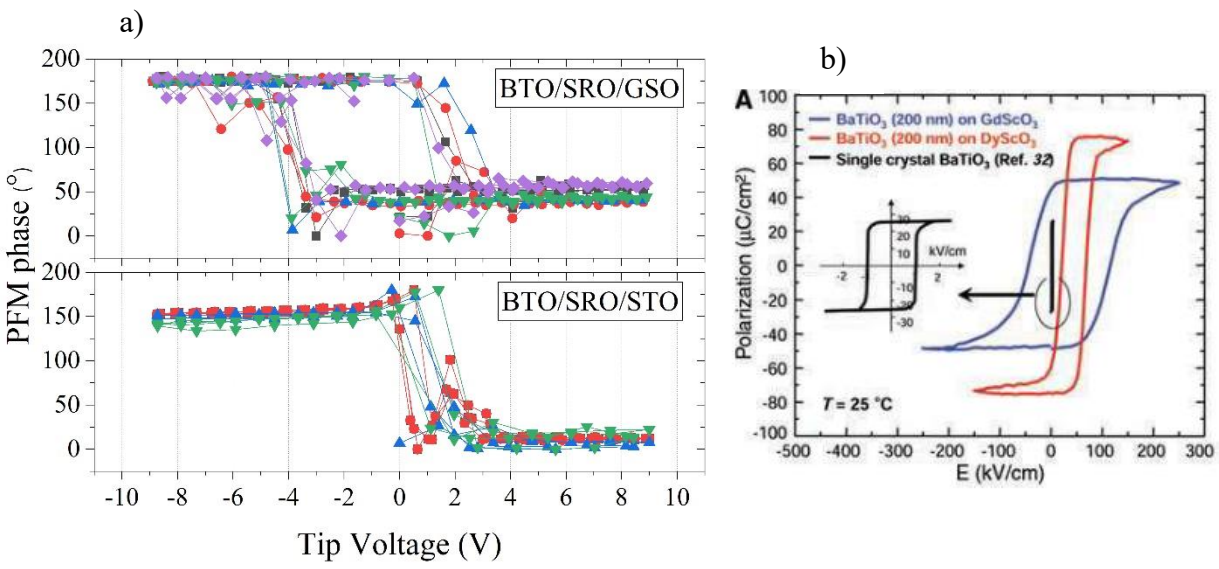


Figure B.4 *a) SS-PFM phase loops for fully strained BTO/SRO on GSO (top) and STO (bottom); each curve corresponds to a different probing location. b) P-E loop taken from the work of Choi. et al.*[3]

Although the loops observed on STO closely resemble those previously reported by our group for as-grown films of the same structure[11], it is important to note that coercive voltages are highly sensitive to the defect landscape of the films, and thus to the specific growth method and parameters employed. For the initial aim of this thesis—probing polarization-switching kinetics in relatively thick (~18 nm) BTO films (Chapter 3)—substrates with in-plane lattice parameters closer to GSO were identified as most suitable. At this thickness range, the reduced remnant polarization expected on GSO does not hinder ferroelectric performance, while the wider loops provide a more favorable window for kinetic studies. Because GSO availability was limited at the time of our growths, we proceeded with DSO as a practical proxy (pseudo-cubic lattice ≈3.94 Å) which sits between STO (3.905 Å) and GSO (3.968 Å).

B.3 Concluding remarks

To conclude this section on PLD growth and strain analysis, the key findings can be summarized as follows:

1. We studied epitaxial strain in BTO/SRO bilayers across different substrates to define the optimal lattice mismatch window for coherent growth.
2. The influence of SRO and BTO thickness on strain relaxation and its correlation with near-surface cation stoichiometry was systematically investigated.
3. Under our growth conditions, the strain state was found to govern stoichiometric deviations: fully strained films showed the largest Ba/Ti imbalance, while partially relaxed films were closest to stoichiometric.
4. Preliminary PFM hysteresis measurements provided a first indication of increased coercive voltages on substrates with lower compressive strain, supporting their suitability for further optimization and electrical studies.

References

1 R. Uecker, D. Klimm, R. Bertram, M. Bernhagen, I. Schulze-Jonack, M. Brützam, A. Kwasniewski, T.M. Gesing, and D.G. Schlom, "Growth and investigation of Nd1-xSmxScO3 and Sm1-xGdxScO3 solid-solution single crystals," Acta Phys Pol A 124(2), 295–300 (2013).

2 A. Biswas, C.H. Yang, R. Ramesh, and Y.H. Jeong, "Atomically flat single terminated oxide substrate surfaces," Prog Surf Sci 92(2), 117–141 (2017).

3 K.J. Choi, M. Biegalski, Y.L. Li, A. Sharan, J. Schubert, R. Uecker, P. Reiche, Y.B. Chen, X.Q. Pan, V. Gopalan, L.-Q. Chen, D.G. Schlom, and C.B. Eom, "Enhancement of Ferroelectricity in Strained BaTiO3 Thin Films," Science (1979) 306(5698), 1005–1009 (2004).

4 E.J. Guo, R. Roth, S. Das, and K. Dörr, "Strain induced low mechanical switching force in ultrathin PbZr0.2Ti0.8O3 films," Appl Phys Lett 105(1), (2014).

5 S. Choudhury, Y.L. Li, L.Q. Chen, and Q.X. Jia, "Strain effect on coercive field of epitaxial barium titanate thin films," Appl Phys Lett 92(14), (2008).

6 G. Catalan, B. Noheda, J. McAneney, L.J. Sinnamon, and J.M. Gregg, "Strain gradients in epitaxial ferroelectrics," Phys Rev B 72(2), 020102 (2005).

7 B. Xiao, V. Avrutin, H. Liu, E. Rowe, J. Leach, X. Gu, Ü. Özgür, H. Morkoç, W. Chang, L.M.B. Alldredge, S.W. Kirchoefer, and J.M. Pond, "Effect of large strain on dielectric and ferroelectric properties of Ba0.5Sr0.5TiO3 thin films," Appl Phys Lett 95(1), (2009).

8 H. Zhou, J. Hong, Y. Zhang, F. Li, Y. Pei, and D. Fang, "Flexoelectricity induced increase of critical thickness in epitaxial ferroelectric thin films," Physica B Condens Matter 407(17), 3377–3381 (2012).

9 L.W. Martin, Y.H. Chu, and R. Ramesh, "Advances in the growth and characterization of magnetic, ferroelectric, and multiferroic oxide thin films," Materials Science and Engineering R: Reports 68(4–6), 89–133 (2010).

10 P.R. Willmott, and J.R. Huber, "Pulsed laser vaporization and deposition," Rev Mod Phys 72(1), 315–328 (2000).

11 I. Spasojevic, G. Sauthier, J.M. Caicedo, A. Verdaguer, and N. Domingo, "Oxidation processes at the surface of BaTiO3 thin films under environmental conditions," Appl Surf Sci 565, 150288 (2021).

12 J.Q. He, E. Vasco, R. Dittmann, and R.H. Wang, "Growth dynamics and strain relaxation mechanisms in BaTiO3 pulsed laser deposited on SrRuO3 SrTiO3," Phys Rev B Condens Matter Mater Phys 73(12), (2006).

13 E. Vasco, R. Dittmann, S. Karthäuser, and R. Waser, “Fabrication of stress-induced SrRuO3 nanostructures by pulsed laser deposition,” in *Appl Phys A Mater Sci Process*, (Springer Verlag, 2004), pp. 1461–1464.

14 D.A. Muller, N. Nakagawa, A. Ohtomo, J.L. Grazul, and H.Y. Hwang, “Atomic-scale imaging of nanoengineered oxygen vacancy profiles in SrTiO3,” Nature 430(7000), 657–661 (2004).

15 D. Kan, and Y. Shimakawa, “Controlled cation stoichiometry in pulsed laser deposition-grown BaTiO3 epitaxial thin films with laser fluence,” Appl Phys Lett 99(8), 081907 (2011).

16 A.P. Chen, F. Khatkhatay, W. Zhang, C. Jacob, L. Jiao, and H. Wang, “Strong oxygen pressure dependence of ferroelectricity in BaTiO3/SrRuO3/SrTiO3 epitaxial heterostructures,” J Appl Phys 114(12), (2013).

17 A. Dasgupta, S. Saremi, X. Ruijuan, L.R. Dedon, S. Pandya, A.R. Damodaran, and L.W. Martin, “Nonstoichiometry, structure, and properties of Ba1−xTiOy thin films,” J Mater Chem C Mater 6(40), 10751–10759 (2018).